

Ph.D Thesis

Department of Materials Science and Engineering

Carnegie Mellon University

**Effect of the Surface and Interface Electric  
Potential on the Photochemical Reactivity of  
Transition Metal Oxides**

Yisi Zhu

Professor Gregory S. Rohrer  
Professor Paul A. Salvador  
Professor P. Chris Pistorius  
Professor Yoosuf N. Picard  
Professor John Kitchin

*(Advisor, Materials Science and Engineering)*  
*(Advisor, Materials Science and Engineering)*  
*(Materials Science and Engineering)*  
*(Materials Science and Engineering)*  
*(Chemical Engineering)*

## ACKNOWLEDGEMENTS

I would like first to thank my advisors, Dr. Gregory Rohrer and Dr. Paul Salvador, for their guidance and encouragement in my PhD study and research, and for being extremely patient in editing my documents. They set a good example how to be a good scientist and professor. It has been my honor to be advised by them. I also owe my sincere thankfulness to Dr. Chris Pistorius, Dr. Yoosuf Picard, and Dr. John Kitchin for being on my committee. My appreciations will have to go to the staff in the MSE department as well, especially to Jason Wolf, Adam Wise, and Tom Nuhfer, for their continuous assistance. The financial support of the NSF (DMR 1206656) is acknowledged.

I want to express my gratefulness to my friends and colleagues for their help. I would specially like to thank Dr. Li Li, Dr. Andrew Schultz and Dr. Yiling Zhang for teaching me using all experiment instruments at the beginning stage of my graduate study. Also Dr. Ratiporn Munprom, Dr. James Glickstein, Julia Wittkamper, Dr. Miaolei Yan and Siyuan Liu shared their thoughts and helped with my experiments over these years. And I also want to thanks Suzanne Smith, Jeanna Pekarcik, Marygrace Anthowski for their administrative assistance and other MSE staff.

Finally, I want to give the biggest thanks to my parents, who have always been there for me whole-heartedly. And also my husband, who quit his own study in China and come here to accompany me over these years.

## ABSTRACT

Polycrystalline hematite, SrTiO<sub>3</sub> (111), and SrTiO<sub>3</sub> (110) single crystal surfaces exhibit spatial variations in the electric potential due to surface chemisorption, reconstruction, orientation, and bulk polar termination. Such potential variation can bias the motion of photogenerated carriers, and can therefore impact photochemical surface reactions. In this document, it is first demonstrated that surface potential variations on a single surface can be measured by Kelvin Probe Microscopy (KPM). Moreover, the KPM contrast is correlated with the photocathodic and photoanodic reactivity of a terrace or surface orientation. Second, to investigate if charge at a buried interface could control the reactivity of supported films, thin (001) oriented anatase TiO<sub>2</sub> films (< 16 nm) were deposited on SrTiO<sub>3</sub> (111). The films exhibit the same photochemical reactivity as the substrate. This observation suggests that electrons photogenerated in the substrate migrate, under the influence of the buried surface charge induced electric field, to the film surface, where they participate in the photo-reduction reaction.

To optimize the overall photochemical reaction efficiency, one needs to balance the surface area ratio of photocathodic and photoanodic surfaces so that the consumption rate of electrons and holes during the reaction can be equalized. As a strong correlation between surface potential and photo-reactivity exist, one can achieve this goal by controlling the potential variation of photocatalyst's surface. Here, it is demonstrated for both SrTiO<sub>3</sub> (111) and (110) single crystals, that it is possible to tune the surface continuously from being terminated by predominantly high surface potential terraces to predominantly low

surface potential terraces, simply by varying the annealing conditions. As for hematite, it is demonstrated the surface potential is orientation dependent. Therefore, hematite particles with larger surface areas of high surface potential facets should be more efficient for the photo-reduction reaction.

# TABLE OF CONTENTS

<b>CHAPTER 1 Introduction .....</b>	<b>1</b>
<b>1.1 Motivation .....</b>	<b>1</b>
<b>1.2 Objectives .....</b>	<b>3</b>
<b>1.3 Approach .....</b>	<b>5</b>
<b>1.4 Organization.....</b>	<b>6</b>
<b>CHAPTER 2 Background.....</b>	<b>10</b>
<b>2.1 Photochemistry on Semiconductor surfaces .....</b>	<b>10</b>
<b>2.2 Internal Fields in Photocatalyst.....</b>	<b>13</b>
<b>2.3 Charged Surfaces.....</b>	<b>16</b>
<b>2.4 Surface Potential on Oxide .....</b>	<b>18</b>
<b>2.5 Material's Structure and Anisotropy.....</b>	<b>21</b>
<b>2.5.1 Hematite.....</b>	<b>21</b>
<b>2.5.2 Strontium Titanate.....</b>	<b>25</b>
<b>2.6 Photocatalysis with TiO<sub>2</sub>/SrTiO<sub>3</sub> heterostructure .....</b>	<b>28</b>
<b>2.6.1 Energy level diagrams of TiO<sub>2</sub> and SrTiO<sub>3</sub> .....</b>	<b>29</b>
<b>2.6.2 Energy diagrams of thin film TiO<sub>2</sub>/SrTiO<sub>3</sub>.....</b>	<b>30</b>
<b>CHAPTER 3 Experimental.....</b>	<b>38</b>
<b>3.1 Sample Preparation .....</b>	<b>38</b>
<b>3.1.1 Solid-state reaction &amp; Sample annealing .....</b>	<b>38</b>
<b>3.1.2 Pulsed Laser Deposition (PLD).....</b>	<b>40</b>
<b>3.2 Characterization Techniques.....</b>	<b>42</b>

3.2.1	Marker Reaction .....	42
3.2.2	Characterization of surfaces after marker reaction .....	44
3.2.3	Kelvin Probe Microscopy: Surface Potential Measurement .....	48
3.2.4	Electron Backscatter Diffraction .....	50
3.2.5	X-ray Diffraction and Reflectometry .....	52
<b>CHAPTER 4 The Orientation Dependence of the Photochemical Activity of <math>\alpha</math>-Fe<sub>2</sub>O<sub>3</sub></b>		
.....		57
4.1	Introduction.....	58
4.2	Experimental Procedure .....	61
4.3	Results.....	62
4.4	Discussion .....	72
4.5	Conclusions.....	76
<b>CHAPTER 5 Controlling the Relative Areas of Photocathodic and Photoanodic Terraces on the SrTiO<sub>3</sub> (111) Surface</b>		
.....		80
5.1	Introduction.....	81
5.2	Experimental Procedure .....	84
5.3	Results.....	86
5.4	Discussion .....	98
5.5	Conclusions.....	102
<b>CHAPTER 6 Controlling the Termination and Photochemical Reactivity of the SrTiO<sub>3</sub> (110) Surface</b>		
.....		107
6.1	Introduction.....	108
6.2	Experimental Procedure .....	111

6.3	Results.....	112
6.4	Discussion .....	127
6.5	Conclusions.....	131
<b>CHAPTER 7 Buried Charge at the TiO<sub>2</sub>/SrTiO<sub>3</sub> (111) Interface and its Effect on</b>		
<b>Photochemical Reactivity .....</b>		<b>135</b>
7.1	Introduction.....	136
7.2	Experimental Procedure .....	138
7.3	Results.....	139
7.4	Discussion .....	146
7.5	Conclusion .....	151
<b>CHAPTER 8 Conclusions .....</b>		
<b>8.1 Photochemical activity and surface potential correlation.....</b>		<b>156</b>
<b>8.2 Control surface termination of SrTiO<sub>3</sub>.....</b>		<b>158</b>
<b>8.3 Photochemical activity of TiO<sub>2</sub>/SrTiO<sub>3</sub> heterostructure .....</b>		<b>160</b>

## LIST OF FIGURES

<b>Figure 2.1.</b> Schematic of illustration the basic theory of photolysis and the band position of $\text{Fe}_2\text{O}_3$ , $\text{SrTiO}_3$ and $\text{TiO}_2$ .....	12
<b>Figure 2.2.</b> The internal field enhanced photogenerated charge carrier separation: (a) ferroelectric polarization; (b) p-n junctions; (c) polar interfaces; and (d) polymorph junctions.....	15
<b>Figure 2.3.</b> Schematic electronic energy level diagrams of a sample (left side) and a conductive AFM tip (right side) .....	19
<b>Figure 2.4.</b> (a) Corundum structure of hematite and the trigonal distortion in two face sharing octahedral. (b) $\text{H}_2\text{O}$ chemisorption species on hematite surfaces .....	22
<b>Figure 2.5.</b> Schematics of hematite viewed along (a) $[2110]$ and (b) $[1101]$ . The dashed black lines indicate (a) $(0001)$ and (b) $(1102)$ surfaces .....	23
<b>Figure 2.6.</b> Schematic of $\text{SrTiO}_3$ viewed along $[001]$ direction.....	26
<b>Figure 2.7.</b> The energy level diagram of $\text{SrTiO}_3$ on the left and the band structure of anatase $\text{TiO}_2$ on the right. ....	30
<b>Figure 2.8.</b> The energy level diagram of $\text{TiO}_2/\text{SrTiO}_3$ in contact with solution.....	31
<b>Figure 2.9.</b> The energy level diagrams of a $\text{SrTiO}_3$ $(111)$ substrate and a anatase $\text{TiO}_2$ film in contact with solution in the case of (a) negatively charged and (b) positively charged termination .....	32
<b>Figure 3.1.</b> Schematic of the pulsed laser deposition vacuum chamber used in this work, showing the location of the substrate, target and incident laser beam.....	42

<b>Figure 3.2.</b> Schematic of photochemical marker reaction .....	43
<b>Figure 3.3.</b> (a) AFM topography image, (b) dark field optical microscopy image and (c) processed dark field optical microscopy image of the same area of the surface of an annealed hematite polycrystal after a silver marker reaction.....	46
<b>Figure 3.4.</b> Schematic illustration of KFM working theory.....	49
<b>Figure 3.5.</b> Examples of EBSD orientation mapping of an Fe <sub>2</sub> O <sub>3</sub> polycrystal .....	51
<b>Figure 3.6.</b> Illustration of the principle of X-ray reflectivity .....	54
<b>Figure 4.1.</b> Schematic electronic energy level diagrams of hematite sample (left side) and a conductive AFM tip (right side).....	60
<b>Figure 4.2.</b> (a) and (b) are both representative AFM images of $\alpha$ -Fe <sub>2</sub> O <sub>3</sub> surfaces after silver reduction. ....	62
<b>Figure 4.3.</b> Inverse pole figure (orientation) maps of the $\alpha$ -Fe <sub>2</sub> O <sub>3</sub> surface.....	64
<b>Figure 4.4.</b> Orientation dependent activity (as determined from AFM measurements) of 89 grains plotted on the standard stereographic triangle for hexagonal crystals. ....	65
<b>Figure 4.5.</b> Dark field optical microscopy images of the $\alpha$ -Fe <sub>2</sub> O <sub>3</sub> surface after the photochemical reduction of Ag.....	66
<b>Figure 4.6.</b> Orientation dependent activity (as determined from optical microscopy measurements) of 547 grains plotted on the standard stereographic triangle for a hexagonal crystal.....	67
<b>Figure 4.7.</b> A representative KFM image (a) and the associated AFM topography image (b), as well as the DF-OM image after reaction (c) .....	68

**Figure 4.8.** (a) The average relative potential value measured by KFM plotted versus orientation on a stereographic projection. (b) A similar plot of the average activity measured from DF-OM images ..... 70

**Figure 4.9.** A calculated electronic band structure for hematite, with the bands rigidly shifted to reflect the experimentally observed band gap ..... 73

**Figure 5.1.** (a) The unit cell of perovskite SrTiO<sub>3</sub>. (b) Schematic of SrTiO<sub>3</sub> (111) planes viewed along [110]..... 82

**Figure 5.2.** (a) Surface topography AFM image and (b) surface potential image recorded of the same area. In (c), height cross-section and the potential profile are extracted from the same location..... 87

**Figure 5.3.** Topographic AFM images (a) after silver photoreduction and (b) lead photooxidation. In (c), the fractional surface coverage of Ag and Pb-containing particles are plotted..... 88

**Figure 5.4.** Topographic AFM images of samples annealed without (a) and with (b-d) different TiO<sub>2</sub>/SrTiO<sub>3</sub> powder mixtures after the photochemical reduction of silver ..... 90

**Figure 5.5.** AFM topography images of the surface before any reactions (a) Sample annealed in air. (b)-(d) Samples were annealed with a powder reservoir..... 92

**Figure 5.6.** (a) High precision topographic AFM image recorded on the clean surface of a sample annealed with TiO<sub>2</sub> powder. (b) Image of the same area after the photoreduction of silver. (c) The surface potential image of the same area (d) The height (solid line) and surface potential (dashed line) profiles extracted from the same location..... 93

**Figure 5.7.** Surface potential images of the same location of the sample annealed with 31.4 wt% Ti powder mixtures. (a) The clean surface after thermal annealing. (b) The

hydrated surface after soaking the sample in water for 20 h. (c) The surface after it was used to reduce silver and the silver was removed. All images are  $15\ \mu\text{m} \times 15\ \mu\text{m}$ . The black lines mark identical locations in the images..... 95

**Figure 5.8.** Ti 2p and Sr 3d core level XPS spectra from SrTiO<sub>3</sub> (111) surfaces with (a) 55 % photocathodic terraces and (b) 86 % photoanodic terraces ..... 97

**Figure 5.9.** Oxygen 1s XPS spectra from SrTiO<sub>3</sub> (111) surfaces with (a) 55 % photocathodic terraces and (b) 86 % photoanodic terraces ..... 98

**Figure 6.1.** Schematic of SrTiO<sub>3</sub> (110) plane viewed along [001] direction ..... 110

**Figure 6.2.** (a) Topographic AFM image (b) surface potential image (c) topographic image after lead photooxidation (d) topographic image after silver photoreduction. In (e), height cross-section and surface potential profile are extracted from the same location ..... 114

**Figure 6.3.** Surface topography AFM image of samples annealed at 1200 °C for (a) 24 hours (b) 12 hours (c) 3 hours and (d) 0 hour after the photooxidation of lead..... 117

**Figure 6.4.** Surface topography AFM image of samples annealed at 1200 °C for (a) 24 hours (b) 12 hours (c) 3 hours and (d) 0 hour after the photochemical reduction of silver. .... 117

**Figure 6.5.** Surface topography AFM image scanned on clean surface of samples annealed at 1200 °C for (a) 24 hours (b) 12 hours (c) 3 hours and (d) 0 hour..... 117

**Figure 6.6.** Topographic AFM images after lead photooxidation for samples annealed at 1100 °C for (a) 6 h (b) 0 h and samples annealed at 1000 °C for (c) 6 h (d) 0 h..... 118

**Figure 6.7.** Surface topography AFM image after silver photoreduction for samples annealed at 1100 °C for (a) 6 hours (b) 0 hours and samples annealed at 1000 °C for (c) 6 hours (d) 0 hours ..... 120

**Figure 6.8.** Surface topography AFM image scanned on clean surface of samples annealed at 1100 °C for (a) 6 hours (b) 0 hours and samples annealed at 1000 °C for (c) 6 hours (d) 0 hours..... 120

**Figure 6.9.** (a) Topographic AFM image after lead photooxidation, (b) topographic image after silver photoreduction recorded, (c) topographic image of the clean surface, and (d) surface potential image for sample annealed with 2 g TiO<sub>2</sub> powder at 1000 °C for 6 h. .... 122

**Figure 6.10.** (a) Topographic AFM image after lead photooxidation, (b) topographic image after silver photoreduction recorded, (c) topographic image of the clean surface, and (d) surface potential image of the same area of the sample annealed at 1100 °C for 6 h with 0.02 g Sr<sub>3</sub>Ti<sub>2</sub>O<sub>7</sub>..... 124

**Figure. 11.** Topographic AFM image of samples annealed with 2 g TiO<sub>2</sub> powder (a) after lead photooxidation and (b) after silver photoreduction. Topographic AFM image of samples annealed with 0.12 g Sr<sub>3</sub>Ti<sub>2</sub>O<sub>7</sub> powder (c) after lead photooxidation and (d) after silver photoreduction. Both samples were annealed at 1100 °C for 6 h..... 125

**Fig. 6.12.** The fractional coverage of photoanodic and photocathodic terraces versus the annealing time for samples shown in Figs. 2 through 11 ..... 126

**Figure 7.1.** (a) Topographic AFM image of the clean SrTiO<sub>3</sub> (111) surface. (b) Surface potential image of the same area. (c) Topographic image of the same area after it was used to photochemically reduce Ag<sup>+</sup> ..... 140

**Figure 7.2.** Topographic AFM images (semi-contact mode) of (a) the bare SrTiO<sub>3</sub> (111) surface after annealing and (b) the same area after depositing a 2.2 nm thick TiO<sub>2</sub> film. .... 141

**Figure 7.3.** (a) XRD patterns of the bare SrTiO<sub>3</sub> (111) substrate and the TiO<sub>2</sub>/SrTiO<sub>3</sub> heterostructure. (b) Example of an X-ray reflectivity curve measured on a TiO<sub>2</sub> film/SrTiO<sub>3</sub> (111) single crystal heterostructure. (c) Electron backscatter diffraction pattern from TiO<sub>2</sub>/SrTiO<sub>3</sub> heterostructure..... 142

**Figure 7.4.** (a) and (d): AFM topographic images of bare SrTiO<sub>3</sub> (111) substrates after silver-reduction reactions. (b) and (e): Surface potential images measured in the same areas as (a) and (d), respectively, after deposition of a 0.9 (b) and 2.2 (e) nm titania film. (c) and (f): AFM topographic images of the two heterostructures from (b) and (e), respectively, after the silver-reduction reaction ..... 144

**Figure 7.5.** Topographic AFM images of the same areas of the substrate ((a) & (c)) and film surfaces ((b) & (d)), after the photoreduction of silver, for two different film thicknesses ..... 146

**Figure 7.6.** Schematic energy level diagrams of SrTiO<sub>3</sub> (111) and SrTiO<sub>3</sub> (111)/TiO<sub>2</sub> heterostructures and a conductive AFM tip ..... 149



# Chapter 1 Introduction

## 1.1 Motivation

Photocatalysis is a promising method to produce hydrogen, a high energy density clean energy source, on large scale by directly splitting water using solar energy.<sup>1</sup> During the reaction, electrons and holes photogenerated in the volume of a photocatalyst migrate to the catalyst surface where they can respectively reduce and oxidize water and produce hydrogen and oxygen gases. However, photocatalysis is not yet a commercial technology because of its low efficiency under visible light irradiation. Currently, research has focused on two routes for splitting water. The first route uses photoelectrochemical cells (PECs) with separated reaction locations and the second uses powdered catalysts distributed throughout water.

For PEC systems, photogenerated carriers are separated on the macroscale to different electrodes; hydrogen evolves at the cathode and oxygen evolves at the physically separated anode. The configuration of PECs make naturally separates electron-hole pairs and, therefore, decreases recombination of photogenerated carriers and back reactions of chemical intermediates.<sup>2,3</sup> Unfortunately, the cost of constructing long lived and efficient PECs hinders its commercial application. Also, the overall efficiency is limited by the rate of charge carrier or ion transfer between the reactive electrodes.<sup>2</sup>

Powder photocatalysts have the potential to be fabricated at much lower costs than PECs, but their efficiencies are much lower. Their low efficiency is frequently attributed to two primary causes: photogenerated carrier recombination and chemical intermediate /

product back reactions.<sup>4, 5</sup> Powder photocatalysts can be considered as a short-circuited version of a PEC, where different regions of the powder surface perform the photocathodic and photoanodic functions. Because a uniform photocatalyst contains no effective charge separation mechanism, carriers remain in close proximity, as do the cathodic and anodic surface sites. The traditional approach to addressing this has been to decorate the surface with a co-catalyst, leading to reaction separation and some driving force for charge separation. This has not, unfortunately, lead to the creation of useful photocatalysts.

More recent work has focused on natural inhomogeneities in some photocatalysts to separate the carriers and reaction sites. For example, some photocatalysts have natural internal electric fields, such as ferroelectrics<sup>6, 7</sup>, which drive photogenerated carriers to different surface regions, resulting in the reduction and oxidation products being spatially separated.<sup>8</sup> Some photocatalysts have naturally occurring anisotropic photocatalytic surface reactivity, such as  $\text{TiO}_2$ ,<sup>9</sup>  $\text{BiVO}_4$ ,<sup>10</sup>  $\text{SrTiO}_3$ <sup>11</sup> and  $\text{Fe}_2\text{O}_3$ <sup>12</sup>. For these materials, some orientations are significantly more reactive in the photocatalytic reduction or oxidation process than other orientations, while some orientations are inert for photochemical reactions. Therefore, a catalyst should be mainly constructed by those photochemically reactive facets to increase the efficient surface area for the reaction.<sup>13</sup> As the overall reaction rate is determined by the slowest step, to split water, one needs to balance the surface area ratio of photoreduction and photooxidation facets, so that the consumption rate of electrons and holes during reaction can be equalized, and the overall efficiency can be maximized. However, more work is needed to realize precisely how to achieve this.

## 1.2 Objectives

The research described in this document has two goals. The first goal is to investigate how photochemical reactions are related to surface potential. Building off of this, the second goal is to develop an ability to tune the overall photochemical activity of a catalyst by controlling relative surface coverage of photoreduction (photocathodic) and photooxidation (photoanodic) reactive areas.

The local surface potential of an oxide surface is determined by the work function and local surface charges (and charge distribution in the near surface region of the catalyst). Surface charge can originate from natural polar terminations, from bound charge associated with internal polarizations (in ferroelectrics, piezoelectrics, or flexoelectrics), and from adsorbed surface species. Differences in local surface potential can induce electric fields within the photocatalyst. If the potential gradient is sufficiently large (and the electrical conductivity is sufficiently low), the motion of charge carriers will be affected. Generally speaking, electrons will be directed to the high surface potential regions, as bands are bent more downward at surface; while holes will be directed to the low surface potential regions, as there is more upward band bending. The projects described here are motivated by the idea that a facet or atomically flat terrace with more positive or less positive surface potential will promote either reduction or oxidation processes, respectively, and that this will lead to a spatial separation of H<sub>2</sub> and O<sub>2</sub> generation sites. In this work, I am interested in how local surface charge affects orientation-dependent reactivity in polycrystalline Fe<sub>2</sub>O<sub>3</sub> and terrace reactivity in single crystalline SrTiO<sub>3</sub>.

Potential differences and internal fields also exist at buried interfaces in heterostructured photocatalysts, and these can play a role on the photochemical activity of

heterostructures. Previous observations on TiO<sub>2</sub>/ferroelectric heterostructures<sup>14, 15</sup> showed that the internal field originating from the spontaneous polarization in the buried ferroelectric influenced the photochemical activity of the TiO<sub>2</sub> overlayer. Motivated by this, I am interested in whether buried surface charge on non-ferroelectric SrTiO<sub>3</sub> single crystals can be captured and if it influences the reactivity of TiO<sub>2</sub> overlayers. I will investigate the hypothesis that internal fields at the buried substrate surface control the reactivity of its overlayers (films).

My investigations of tuning the photochemical activity through controlling surface area ratio of high or low surface potential terraces are motivated by the concept that a catalyst surface that attracts photogenerated electrons or holes will exhibit higher efficiencies in photoreduction or photooxidation reactions, respectively. It is hypothesized that a semiconductor surface that is mainly constructed by relatively high or low potential terraces will participate preferentially in redox reactions. To test the feasibility of these ideas, experiments were performed to answer the following questions:

1. Do measured surface potential correlate with the spatial location of photochemical half reactions on the surfaces of Fe<sub>2</sub>O<sub>3</sub> and SrTiO<sub>3</sub> catalysts?
2. Can the SrTiO<sub>3</sub> catalyst's overall photochemical reactivity be tuned by modifications of the area percentage of high or low potential surfaces (terminations)?
3. Do potential differences at buried interfaces in TiO<sub>2</sub>/SrTiO<sub>3</sub> heterostructures affect the photochemical activity of the film surface?

### 1.3 Approach

The approach taken in this research relies on two main experimental methods: photochemical marker reaction to investigate the spatial variation in reactivity and Kelvin Force Microscopy (KFM) to measure the spatial variation in surface potentials. Marker reactions leave insoluble reaction products on the photocatalyst surface, thus marking the reduction or oxidation sites. The products can be located on the surface using atomic force microscopy (or other microscopy methods). Subsequently, the location of specific reaction sites, and their relative reactivity, can be correlated with the local surface potential measured at the reaction sites.

To address the first question posed above, I studied the correlation between the reactivity and surface potential of all orientations of polycrystalline hematite  $\text{Fe}_2\text{O}_3$ , and (111) and (110) surfaces of single crystal perovskite  $\text{SrTiO}_3$ . Hematite was chosen because it is reported to exhibit various surface reconstructions<sup>14-16</sup> and to accommodate differently charged adsorbates,<sup>17-19</sup> both of which are orientation dependent. As such, we expect the local surface potential also to depend strongly on orientation, as should (therefore) reactivity. Randomly oriented polycrystalline hematite ceramics were used to observe the spatial dependence of reactivity and surface potential over the range of all possible crystallographic orientations. For  $\text{SrTiO}_3$ , the ideal bulk terminations of (111) and (110) surfaces are polar. These ideal surfaces can either be terminated by positively charged or a negatively charged layers. In reality, the surface rearranges in some fashion, which is likely termination dependent, and may yet yield two distinct surfaces with different potentials (this will be demonstrated). Given two oppositely charged surfaces on a single crystal, one

can investigate the correlation between local surface potential and reactivity in a uniform bulk.

To address the second question, the relative areas of the two different chemical termination on either SrTiO<sub>3</sub> (111) and (110) single crystal surfaces was controlled using thermal anneals in different atmospheres. Appropriate anneals were developed by measuring (with KFM) the area percentage of high and low potential surfaces. The photochemical activities were then observed using marker reactions on predominantly high or low potential surfaces. The overall photochemical activity is quantified as the relative amount of products after reaction, using the area percentage of surfaces that covered with products to represent the photochemical activity.

To address the last question, TiO<sub>2</sub>/SrTiO<sub>3</sub> (111) heterostructures were fabricated. The potential distribution and spatial reactivity of the SrTiO<sub>3</sub> (111) substrate were addressed above, and the spatial reactivity at the TiO<sub>2</sub> film surface can be correlated and compare to that. Because the impact of the buried layer is expected to diminish with increasing TiO<sub>2</sub> thickness, investigations are carried out at different thicknesses. The hypothesis is that the spatial reactivity of thin TiO<sub>2</sub> layers will be correlated with that of the underlying SrTiO<sub>3</sub> substrate surfaces.

## **1.4 Organization**

This document contains eight chapters. It starts with this introductory chapter, and the remaining chapters are:

- Chapter 2 contains background information on photocatalytic water splitting,

internal electric fields in photocatalysts, KFM measured surface potentials, and relevant properties of  $\text{Fe}_2\text{O}_3$ ,  $\text{SrTiO}_3$  and  $\text{TiO}_2/\text{SrTiO}_3$  heterostructure, such as structure, possible reconstructions, adsorption species and energy band diagrams.

- Chapter 3 introduces the details of the experimental techniques used for fabricating, characterizing, and testing the photocatalysts.
- Chapter 4 focuses on the orientation dependence of the visible-light photochemical reactivity on polycrystalline  $\text{Fe}_2\text{O}_3$  (hematite) and its correlation with the orientation dependent surface potential (addressing question 1).
- Chapter 5 focuses on making the same correlation between surface potential and photochemical reactivity on annealed single crystal  $\text{SrTiO}_3$  (111) surfaces. Through thermal annealing methods described therein, the fractional surface coverage of high or low surface potential terraces are tuned, and the photochemical reactivity changes are modified accordingly (addressing questions 1 & 2).
- Chapter 6 focuses on making nearly identical correlations to those in Chapter 5, except for using annealed single crystal  $\text{SrTiO}_3$  (110) surfaces. Moreover, a more extensive demonstration of surface control through annealing is demonstrated (addressing questions 1 & 2).
- Chapter 7 addresses the effects potential differences at the buried interface have on the photochemical reactivity of overlayers in  $\text{TiO}_2/\text{SrTiO}_3$  (111) heterostructures (addressing question 3).
- Chapter 8 summarizes the results and findings of this thesis.



## Reference

1. Z. Zou, J. Ye, K. Sayama, and H. Arakawa, "Direct splitting of water under visible light irradiation with an oxide semiconductor photocatalyst," *Nature*, 414[6864] 625-27 (2001).
2. M. Grätzel, "Photoelectrochemical cells," *Nature*, 414[6861] 338-44 (2001).
3. T. Bak, J. Nowotny, M. Rekas, and C. Sorrell, "Photoelectrochemical hydrogen generation from water using solar energy. Materials-related aspects," *International journal of hydrogen energy*, 27[10] 991-1022 (2002).
4. M. A. Fox and M. T. Dulay, "Heterogeneous photocatalysis," *Chemical reviews*, 93[1] 341-57 (1993).
5. M. R. Hoffmann, S. T. Martin, W. Choi, and D. W. Bahnemann, "Environmental applications of semiconductor photocatalysis," *Chemical reviews*, 95[1] 69-96 (1995).
6. J. L. Giocondi and G. S. Rohrer, "Spatial separation of photochemical oxidation and reduction reactions on the surface of ferroelectric BaTiO<sub>3</sub>," *The Journal of Physical Chemistry B*, 105[35] 8275-77 (2001).
7. A. Schultz, Y. Zhang, P. Salvador, and G. Rohrer, "Effect of Crystal and Domain Orientation on the Visible-Light Photochemical Reduction of Ag on BiFeO<sub>3</sub>," *Acs Applied Materials & Interfaces*, 3[5] 1562-67 (2011).
8. M. Anpo, "Surface photochemistry." Wiley, (1996).
9. J. Lowekamp, G. Rohrer, P. Morris Hotsenpiller, J. Bolt, and W. Farneth, "Anisotropic photochemical reactivity of bulk TiO<sub>2</sub> crystals," *The Journal of Physical Chemistry B*, 102[38] 7323-27 (1998).
10. R. Li, F. Zhang, D. Wang, J. Yang, M. Li, J. Zhu, X. Zhou, H. Han, and C. Li, "Spatial separation of photogenerated electrons and holes among {010} and {110} crystal facets of BiVO<sub>4</sub>," *Nature communications*, 4 1432 (2013).
11. J. L. Giocondi, P. A. Salvador, and G. S. Rohrer, "The origin of photochemical anisotropy in SrTiO<sub>3</sub>," *Topics in Catalysis*, 44[4] 529-33 (2007).
12. Y. Zhu and A. M. R. Schultz, Gregory S. Salvador, Paul A., "The Orientation Dependence of the Photochemical Activity of  $\alpha$ -Fe<sub>2</sub>O<sub>3</sub>," *Journal of the American Ceramic Society* (2016).
13. Z. Zheng, B. Huang, X. Qin, X. Zhang, Y. Dai, M. Jiang, P. Wang, and M. H. Whangbo, "Highly efficient photocatalyst: TiO<sub>2</sub> microspheres produced from TiO<sub>2</sub> nanosheets with a high percentage of reactive {001} facets," *Chemistry–A European Journal*, 15[46] 12576-79 (2009).
14. Y. Zhang, A. M. Schultz, P. A. Salvador, and G. S. Rohrer, "Spatially selective visible light photocatalytic activity of TiO<sub>2</sub>/BiFeO<sub>3</sub> heterostructures," *Journal of Materials Chemistry*, 21[12] 4168-74 (2011).
15. N. V. Burbure, P. A. Salvador, and G. S. Rohrer, "Photochemical Reactivity of Titania Films on BaTiO<sub>3</sub> Substrates: Influence of Titania Phase and Orientation," *Chemistry of Materials*, 22[21] 5831-37 (2010).

## Chapter 2 Background

*This chapter will introduce the relevant background for the research projects introduced in Chapter 1 and described in detail later in this document. The chapter is broken down into subsections devoted to: photochemistry at semiconductor surfaces, internal electric fields in photocatalysts, charged surfaces, surface potentials, the structure and anisotropy of  $Fe_2O_3$  and  $SrTiO_3$ , and heterostructured  $TiO_2/SrTiO_3$  photocatalysts .*

### 2.1 Photochemistry on Semiconductor surfaces

In a typical particulate semiconductor photocatalyst, an electron in the valence band is excited to the conduction band when a photon with an energy greater than the band gap ( $h\nu > E_g$ ) is absorbed, leaving a hole in the valence band. This process is indicated in Fig. 2.1 by the orange arrow, on the left hand side. After such a photoexcitation, some of the electrons and holes migrate to the surface of the photocatalyst prior to recombination (if they are not at the band edge, they can also move in energy space towards the band edges). If these electrons/holes have an appropriate energy relative to specific ions in solution, they can reduce/oxidize these ions. Several relevant redox levels (water reduction, or the hydrogen level, water oxidation, or the oxygen level,  $Ag^+$  reduction, and  $Pb^{2+}$  oxidation)

are given in Fig. 2.1 as horizontal lines, their position being relative to the normal hydrogen electrode (NHE) scale (shown on each side of the figure). For example, in a photocatalytic water splitting process, the photocatalyst's conduction band edge needs to lie above the hydrogen level (0 V/NHE) and valence band edge needs to lie below the oxygen level (1.23 V/NHE).<sup>1</sup> If so, electrons in the conduction band and holes in the valence band can act as reducing and oxidizing agents, respectively, to produce H<sub>2</sub> and O<sub>2</sub>.

In this project, I aim to study the correlation between surface potential and reactivity. One needs to, therefore, spatially determine preferred reaction sites. In the water photolysis process, the evolution of gaseous hydrogen and oxygen cannot be easily tracked; therefore it is impossible to locate the reaction site and compare the relative spatial reactivity. However, using the marker reactions, surface locations covered with more products are considered to be more reactive than other locations.<sup>2, 3, 4, 5</sup> As such, silver and lead marker reactions were used as indicators of reduction and oxidation reactions, respectively. Electrons in the conduction band need to be above the Ag<sup>+</sup> reduction level of 0.8 V/NHE,<sup>2, 3</sup> and holes in the valence band need to be below the Pb<sup>2+</sup> oxidation level of 1.69 V/NHE.<sup>4, 5</sup> The insoluble Ag<sup>0</sup> or PbO<sub>2</sub> solids can be detected by optical microscopy or AFM. The relative position of the redox levels for Ag<sup>+</sup> and Pb<sup>2+</sup> are shown in Fig. 2.1.

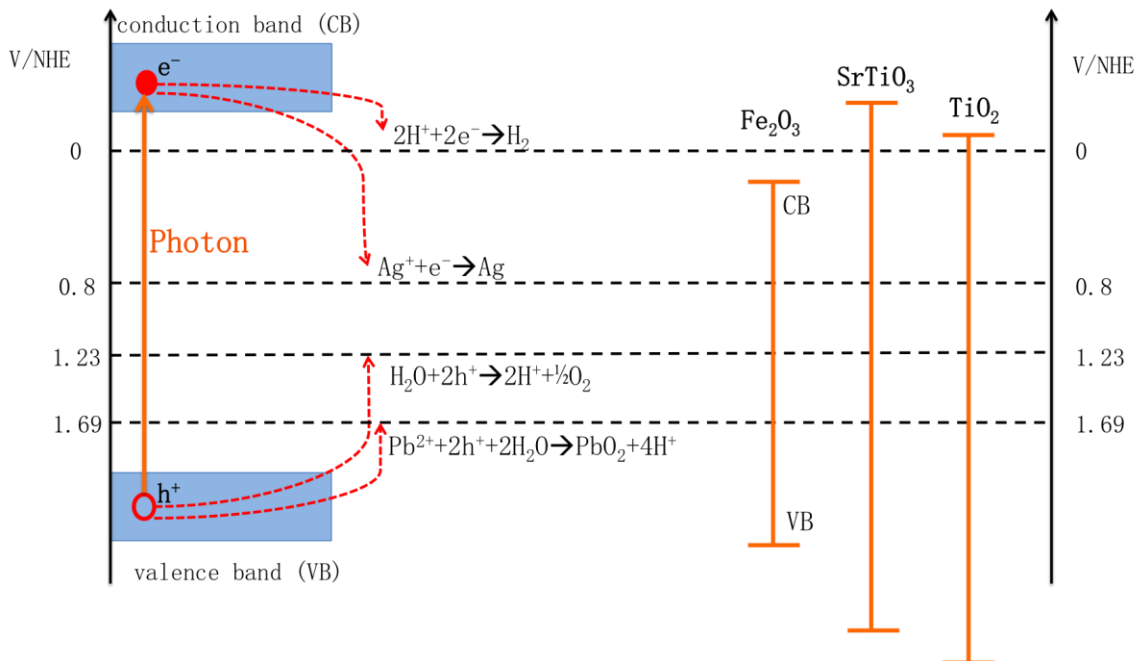


**Figure 2.1.** Schematic of illustration the basic theory of photolysis and the band position of materials relevant to the following research, including  $\text{Fe}_2\text{O}_3$ ,  $\text{SrTiO}_3$  and  $\text{TiO}_2$

The (flat) band positions of all materials studied in this document—  $\text{Fe}_2\text{O}_3$ ,  $\text{SrTiO}_3$ , and  $\text{TiO}_2$ — are shown on the right hand side of Fig. 2.1, indicating they should all be active for the marker reactions chosen. Hematite has a narrow band gap of  $1.9 \text{ eV} \sim 2.3 \text{ eV}$ ,<sup>6</sup> which renders it a good absorber of visible light. Because its conduction band lies  $0.21 \text{ eV}$ <sup>7</sup> below the hydrogen scale, it cannot be used to produce hydrogen. However, we can still study its reactivity for reduction using a marker reaction, and correlate it to the surface potential, because the  $\text{Ag}^+/\text{Ag}^0$  redox level is still well below its conduction band level.  $\text{SrTiO}_3$  and  $\text{TiO}_2$  are wide band gap materials.  $\text{SrTiO}_3$  has a band gap of  $3.2 \sim 3.4 \text{ eV}$ <sup>7</sup> and  $\text{TiO}_2$  has a band gap of  $3.0 \text{ eV}$  for rutile phase<sup>8</sup> and  $3.2 \text{ eV}$  for anatase phase.<sup>9, 10</sup> Due to their relatively large band gaps, both phases only absorb UV light to generate electrons and holes. For both materials, the conduction bands lies slightly above the redox level of  $\text{H}^+/\text{H}^2$  and their valence bands lies well below the redox level of  $\text{Pb}^{2+}/\text{Pb}^{4+}$  (as does that of

hematite). Therefore, all materials are capable of photochemically catalyzing the relevant reactions.

## 2.2 Internal Fields in Photocatalyst

The efficiency of powdered photocatalysts is inhibited by carrier recombination and product back reactions.<sup>1</sup> Recombination means photoelectrons and holes recombine before participating in surface reactions. When the evolution sites of hydrogen and oxygen are nearby one another, back reactions can occur between reactive intermediate species or products. Internal electric fields drive electrons and holes in different directions, reducing recombination and, if surfaces have spatially varying internal fields driving reactants to different surface locations, the photoreduction and oxidation processes occur at different sites, reducing back reactions.<sup>11</sup> By this means the overall photocatalytic efficiency can be increased.

Four possible sources of electric fields within photocatalyst are shown in Fig. 2.2. In the cases of ferroelectric materials (Fig. 2.2(a)) and polar interfaces (Fig. 2.2(b)), the internal fields are generated from physical charges associated with the photocatalyst's crystal structure. A ferroelectric material has a spontaneous polarization<sup>12, 13, 14</sup>, which means it exhibits a non-zero electric polarization in the absence of external fields. Ferroelectrics are non-centrosymmetric and the internal polarization occurs because the positive and negative charges have different centers in the unit cell.<sup>15</sup> Classic examples of ferroelectric materials are  $\text{BaTiO}_3$  and  $\text{Pb}(\text{Zr}_x\text{Ti}_{1-x})\text{O}_3$  (PZT), which have distorted perovskite structures ( $\text{SrTiO}_3$  adopts the undistorted parent perovskite structure, described

later). The internal dipolar field within a ferroelectric causes photogenerated carriers to move in opposite directions, which separates electrons and holes and cause oxidation and reduction products to be generated at different locations. Inoue et al.<sup>16</sup> demonstrated that a positively poled ferroelectric PZT produced 10-40 times more hydrogen during photolysis than negatively poled PZT. Most ferroelectrics, however, are not uniformly poled: they contain domains in which the polarization varies, which lowers the overall electrostatic energy. As such, the surfaces of ferroelectrics are expected to (and do) exhibit spatially non-uniform reactivity associated with the domain orientations.

Polar surface terminations can be created when an ionic crystal is cleaved along a direction parallel to the normal of internal planes that have non-zero formal charges (see Fig. 2.2(c)); the two new surfaces are thus oppositely charged.<sup>17</sup> Examples abound in ionic crystals, and two of interest here are the (111) and (110) surfaces of SrTiO<sub>3</sub> and the (0001) and (1 $\bar{2}$ 10) surfaces of hematite.<sup>18, 19</sup> These surfaces are all constructed from planes that alternate between positive and negative charges in the bulk structure. A variety of mechanisms can act to minimize or offset the charge imbalance at a polar surface<sup>17</sup> (as is the case for ferroelectric surfaces), one of which is the creation of an internal field to screen the surface charge. This internal field can then act to separate carriers and spatial reactions.<sup>12</sup> Because charged surfaces are the focus of this work, the effect of charged surfaces on photochemistry are described in the next section (§ 2.3). Most surfaces contain a mix of these polar surface terminations (i.e., are not singly terminated by one type of charged plane), and may exhibit spatial selectivity to reactivity that follows termination type similar to domain specific reactivity on ferroelectrics: this is a focus of my work.

The mechanisms of charge separation in p-n junctions (Fig. 2.2(b)) and polymorph junctions (Fig. 2.2(d)) are similar. When two phases are joined, including different composite materials or materials with different doping levels, the electrons come into equilibrium (by transferring between phases) and the Fermi levels align. An internal field associated with the transferred charges (Fermi level shifts to equilibrate) develops and acts to separate photogenerated charge carriers. Electrons are driven “downhill” to lower energy states and holes are driven “uphill” to higher electron energy states. Descriptions of photocatalysts that take advantage of the internal fields in p-n or polymorph junctions are described elsewhere.<sup>20, 21</sup>

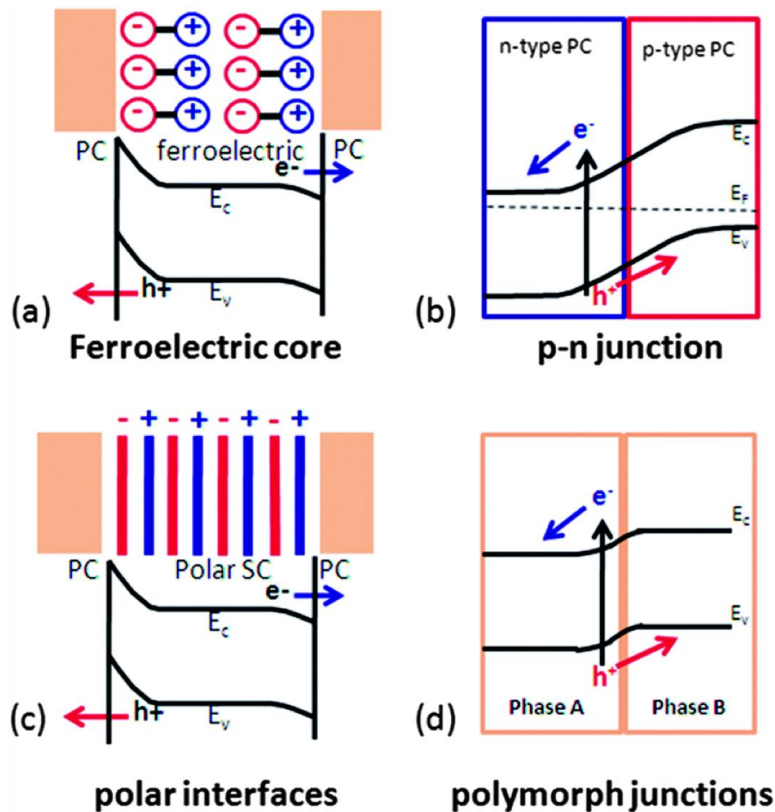


**Figure 2.2.** The internal field enhanced photogenerated charge carrier separation: (a) ferroelectric polarization; (b) p-n junctions; (c) polar interfaces; and (d) polymorph junctions. (PC: photo catalytic active materials; SC: semiconductor). (This figure is reproduced from Li et al.’s publication<sup>11</sup>)

Though this research is mainly focused on the internal field induced by polar surfaces (case (c) in Fig. 2.2), I also include research on junctions that have surface charges at the interphase junctions (interfaces), such as heterostructured coated photocatalysts, which combines the effects of polar surfaces and junctions. When necessary, we will discuss the combination of such effects later in the document.

### 2.3 Charged Surfaces

As discussed above, surface charges cause band bending, which can separate electron-hole pairs near the surface.<sup>22</sup> As shown in Fig 2.3(c), if the surface is positively charged, the bands bend downward, because the electron feels an attractive force toward the surface (and its energy is lowered at surface). Similarly, when the surface is negatively charged, the bands bend upwards, because the electron feels a repulsive force and its energy increases at surface.<sup>23</sup> Therefore, downward band bending will benefit the reduction half reactions because its electric field drives electrons to the surface. Upward band bending will benefit oxidation half reactions, because holes are driven to the surface.

Direct evidence that positively charged surfaces promote reduction reactions and negatively charged surfaces promote oxidation reactions have been shown on PZT and BaTiO<sub>3</sub> ferroelectric surfaces.<sup>24, 25</sup> For these ferroelectric surfaces, a positive (negative) domain refers to a uniform region where positive (negative) charges terminate the surface, as shown in the right (left) side of Fig. 2.2(a). Using a PZT thin film, surface charges (domains) were "written" using a conductive AFM probe; application of a negative (positive) 10 V was used to write positive (negative) domains.<sup>24</sup> For the BaTiO<sub>3</sub> sample,

positive and negative domains were written directly using electron beams.<sup>25</sup> Photocatalysis experiments carried out on these samples found that  $\text{Ag}^+$  was only photoreduced on the positive domains and  $\text{Pb}^{2+}$  was only photooxidized on the negative domains.<sup>26</sup> These observations agree with the expected band bending from the screening the ferroelectric surface charges.

A semiconductor surface can be charged from the polar bulk surface termination (described above) or from the chemisorbed species on the surface. A classic example of a polar surface terminated material is zinc oxide (ZnO). ZnO has a hexagonal wurzite structure, which is polar along the c-axis. The (0001) plane of ZnO can be terminated by a positively charged  $\text{Zn}^{2+}$  layer or negatively charged  $\text{O}^{2-}$  layer. Therefore, a perfectly flat bulk-truncated ZnO (0001) surface would either be positively or negatively charged, depending on which of these two layers terminate the surface. As for the chemisorption induced charging layer, the most common chemisorption would be oxygen and hydroxyls as the samples used in this document are exposed to air and solutions. The chemisorption can introduce charges to the original surface and thus affect the surface's charge state. For example, oxygen chemisorption on ZnO surface will change the charges of  $\text{Zn}^{2+}$  ion by the following reaction<sup>27</sup>:



$\text{H}_2\text{O}$  will also be chemisorbed on the just mentioned ZnO (0001) polar surface through Zn-O-H bonding.<sup>28</sup> The interaction between -OH and Zn site is much stronger than the O site, thus the Zn terminated (0001) has higher density of chemisorption than O terminated (0001) surface. Overall, most surfaces studied in reaction conditions are very different from the ideal surfaces or those found in vacuum. Even for surfaces of exactly the

same orientation, charges associated with chemisorption differ according to the local surface structure and bonding. To provide a better understanding of the anisotropic surface state of materials studied in this document, their structure and surface adsorption species will be elaborated in §2.5.

## 2.4 Surface Potential on Oxide

Photochemical reaction sites are thought to be correlated directly to the local surface potential of a photocatalyst surface, as described above. One method to investigate surface potential is using Kelvin probe force microscopy (KFM). The potential measured using KFM is actually the contact potential difference ( $E_{CPD}$ ) between the photocatalyst surface and the conductive KFM probe. Fig. 2.3 shows a schematic of the relevant energy diagram between tip and sample. For illustration, the local work function at the sample surface ( $\phi_S$ ) is assumed to be less than the work function of the tip ( $\phi_T$ ) (both are defined as positive definite numbers). The schematics are drawn with the Fermi levels aligned (sample surface and tip in equilibrium) and the contact potential difference ( $E_{CPD}$ ) represented by the discontinuity in the vacuum level ( $V_{vac}$ ).

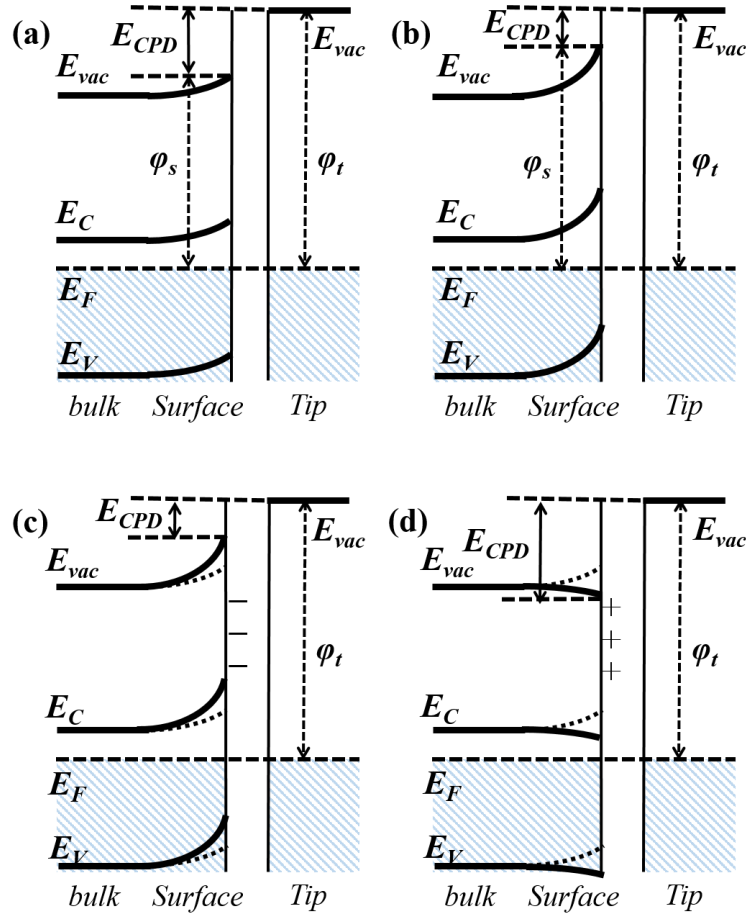


**Figure 2.3.** Schematic electronic energy level diagrams of a sample (left side) and a conductive AFM tip (right side). In (a) and (b), the sample surface is charge neutral and  $E_{CPD} = \phi_s - \phi_t$ . The sample surface work function in (b) is larger than (a). In (c) and (d) the sample surfaces are charged negatively and positively, respectively. The band bending before charging is drawn in dashed line. Compared to that, the surface charges modified  $E_{CPD}$ . In (c) the magnitude of  $E_{CPD}$  is decreased, while in (d) it is increased.

Fig. 2.3 (a) and (b) depict the case for two facets of the same piece of oxide, assuming both do not have bound surface charges. As many oxides are n-type material due to oxygen vacancies, bands are slightly bent upward. However, facets can have different work functions, as work function differs for each orientation and is also sensitive to preparation parameters. The surface termination itself can be electronically different, and may have surface states that attract more or less electrons (these states are not depicted in

the figure). The Figure supposes the facet in (b) has a larger work function than (a), which means the surface in (b) has more electrons than that in (a). Because the bulk below each surface is identical, the Fermi levels are aligned within the material in equilibrium; thus the surface in (b) has more upward band bending than in (a). The contact potential difference is usually defined as :  $E_{CPD} = \phi_S - \phi_T$ . The KFM measured surface potential is opposite in sign, but proportional to the magnitude of  $E_{CPD}$ ,<sup>29</sup> which can be expressed as:

$$\phi_{KFM} = -a (E_{CPD}) = a (\phi_T - \phi_S) \quad (\text{Eq. 2.1}),$$

where  $a$  is a constant ( $0 < a < 1$ ) that relates to the machine settings. Thus, as the work function of a surface is increased, the  $E_{CPD}$  should become less negative (more positive) and the measured surface potential is less positive (more negative). As depicted in Fig. 2.3, the facet shown in (b) would have a lower KFM surface potential than (a).

Fig. 2.3(c) (Fig. 2.3(d)) depicts the changes in Fig. 2.3(a) if that surface was charged negatively (positively) with bound surface charges. A space charge develops in the semiconductor and the bands bend more upward (downward) at the surface. As the magnitude of band bending changed, the contact potential difference changed accordingly. Therefore, negative surface charges decreased the magnitude of  $E_{CPD}$ , resulting in a lower surface potential (Fig. 2.3 (c)), while the positive surface charges give a higher surface potential value (Fig. 2.3 (d)). The differences between Fig. 2.3(a) and Figs. 2.3(b) / (c) are similar because both arise from a negative charge density at the surface, an electronic one in (b) and a chemisorption one in (c).

In general, for surface potentials measured on the same piece of oxide, a higher potential value corresponds to more downward (less upward) band bending at surface, while a lower potential value corresponds to more upward (less downward) band bending.

This near surface band bending will also modify the field experienced by photogenerated carriers, and therefore we hypothesized the photochemical reactivity should correlate with the surface potential. As downward (upward) band bending will attract more electrons (holes) to the surface, the high (low) surface potential facets or terraces are expected to be more reactive in photoreduction (oxidation).

## **2.5 Material's Structure and Anisotropy**

### **2.5.1 HEMATITE**

Hematite adopts the corundum structure, as shown in Fig. 2.4(a); the unit cell is hexagonal with  $a=0.5034$  nm and  $c=1.374$  nm.<sup>30</sup> In this structure, close packed planes of  $O^{2-}$  are stacked along the  $[0001]$  direction in hexagonal<sup>31</sup> close packing (hcp) and  $Fe^{3+}$  fills two thirds of the octahedral sites in planes parallel to  $(0001)$ . The  $FeO_6$  octahedra have a slight trigonal distortion resulting from edge sharing between three neighboring octahedra in the  $(0001)$  plane and face sharing with one octahedron in the  $[0001]$  direction (two face sharing octahedral are highlighted in Fig. 2.4(a)).<sup>32</sup> Because the corundum structure has low symmetry, orientations have low multiplicities. Several factors that will influence the surface charges of different orientation are discussed here.

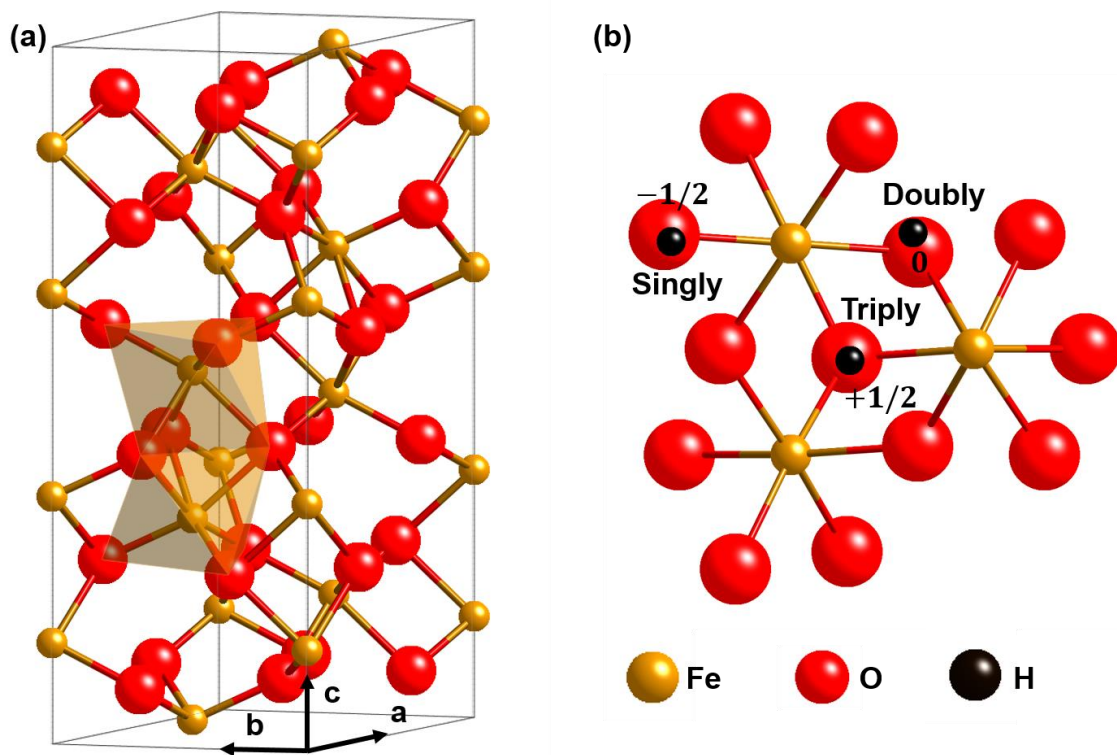


**Figure 2.4.** (a) Corundum structure of hematite and the trigonal distortion in two face sharing octahedral. (b) H<sub>2</sub>O chemisorption species on hematite surfaces. Singly coordinated, doubly coordinated, triply coordinated hydroxyl groups will introduce different amount of charges.

**Surface termination:** The prismatic  $(0\bar{1}10)$  and  $(1\bar{1}00)$  planes are non-polar, while the prismatic  $(1\bar{2}10)$  and the basal  $(0001)$  surfaces are both polar. The bulk-truncated  $(0001)$  is shown (viewed from the side) in Fig. 2.5(a), with a negatively charged oxygen (positively charged iron) plane shown as the upper (lower) surface. The bulk-truncated rhombohedral  $(1\bar{1}02)$  plane can also be either Fe or O terminated (see Fig. 2.5(b)), which indicates it could be polar. However, the iron layers are almost on the same plane as one of the adjacent oxygen layers ( $0.35 \text{ \AA}$  difference), which renders this plane essentially non-polar. In Fig. 2.5(b), the same  $(1\bar{1}02)$  oxygen plane is shown with the upper (lower) surface representing

the polar (nearly non-polar) version. As described in the main chapter of hematite project (§4), the real surfaces of hematite differ considerably from these ideal versions, but their terminations still vary with orientation and they can be charged. Note that all of the above facets are stable, on the Wulff shape of hematite. Among them the  $(1\bar{1}02)$  plane has the lowest surface energy.<sup>33</sup>

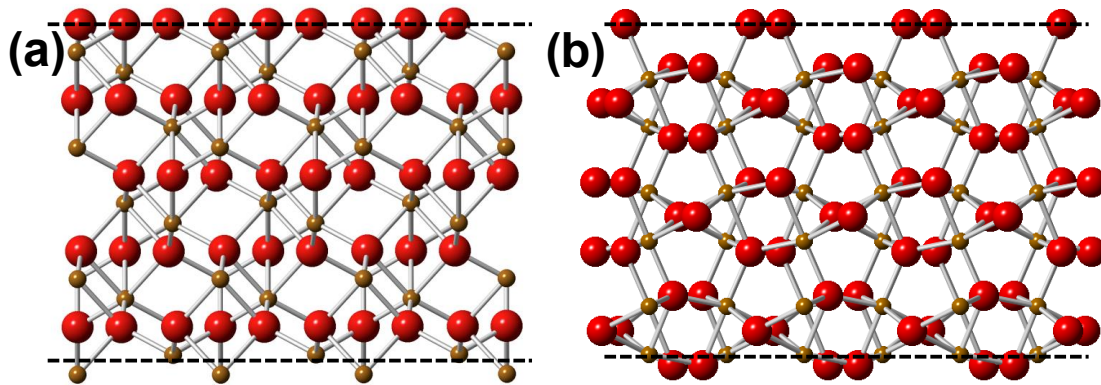


**Figure 2.5.** Schematics of hematite viewed along (a)  $[2\bar{1}\bar{1}0]$  and (b)  $[1\bar{1}0\bar{1}]$ . The dashed black lines indicate (a)  $(0001)$  and (b)  $(1\bar{1}02)$  surfaces. Oxygen terminated planes are depicted on the upper surfaces. The lower surfaces have (a) pure iron termination and (b) mixed termination. The larger red (smaller brown) spheres represent oxygen (iron) and grey lines represent bonds between them.

**Surface chemisorption:** Hematite exposed to air exhibits chemisorption of  $O_2$  and  $H_2O$ .

Chemisorption of  $O_2$  occurs in one second when the pressure is higher than  $10^{-2}$  Torr.<sup>34</sup>

The chemisorption of  $O_2$  will not only introduce charges to the original surface, but also affect the electronic structure. For example, the work function of the  $(0001)$  surface with  $O_2$  chemisorption is 0.8 eV larger than others without chemisorption (measured by UPS spectrum),<sup>34</sup> and the value of measured surface potential by Kelvin force microscopy (KFM) is expected to change accordingly. The anisotropic chemisorption of  $H_2O$  on hematite was studied by various groups. The pressure threshold for  $H_2O$  chemisorption is  $10^{-4}$  Torr<sup>35</sup> and the partial pressure of  $H_2O$  in air varies from  $10^{-1}$ -33 Torr. Researchers

found that the anisotropic chemisorption of H<sub>2</sub>O can greatly affect the charge density of each orientation. Generally, there are three types of adsorbed hydroxyls: single-, double- and triple-coordinated hydroxyls, with  $-\frac{1}{2}$ , 0,  $+\frac{1}{2}$ , charge states respectively, as shown in Fig. 2.4(b). The (0001) surface is terminated predominantly by double-coordinated hydroxyls. Other orientations that bear different amounts of single- and triple-coordinated hydroxyls are more reactive in protonation or de-protonation reactions that affect charge accumulation.<sup>36</sup> Because chemisorption depends on orientation, and also induces different charge accumulations, the surface potential differs for each orientation.

**Surface reconstructions:** For hematite, different preparation processes will result in different types of surface reconstructions for each orientation. For example, reports show that the (0001) face of hematite has several types of reconstructions as a function of annealing temperature (from 800 °C to 1000 °C) and oxygen partial pressure during the anneal. At lower temperatures, an Fe<sub>3</sub>O<sub>4</sub> (111)-type layer appears on the surface; and at higher temperatures, an Fe<sub>1-x</sub>O(111)/ $\alpha$ -Fe<sub>2</sub>O<sub>3</sub>(0001) interface occurs for high vacuum annealing.<sup>37</sup> Similarly, for hematite ( $1\bar{1}02$ ), the surface could be (with respect to the bulk termination) deficient of iron, stoichiometric, or stoichiometric and hydroxylated, depending on how the surface was polished and annealed.<sup>38, 39</sup> Of course different reconstructions result in different surface charge densities and different work functions.

Currently there are limited numbers of non-UHV studies correlating specific surface terminations and surface charge densities with surface preparation methods. Moreover, nearly all prior work has focused on specific low-index planes, such as (0001), ( $1\bar{1}02$ ), ( $1\bar{1}00$ ). A comprehensive surface structure study of all possible orientations of hematite is very challenging as so many factors influence the outcomes. In this study, I am

interested in how the surface potential influences local reactivity, and the surface potential is also a function of these many factors. Herein, I measure the surface potential by KFM and aim to determine whether a general relation between the surface potential and orientation of  $\text{Fe}_2\text{O}_3$  exists, whether it is stable in reaction conditions, and whether it influences local reactivity.

### 2.5.2 STRONTIUM TITANATE

$\text{SrTiO}_3$  crystallizes in the  $ABO_3$  cubic perovskite structure (space group  $\text{Pm}\bar{3}\text{m}$ ) with a lattice parameter of  $a = 0.3905$  nm and a density of  $\rho = 5.12$  g/cm<sup>3</sup>.<sup>31</sup> The  $\text{Ti}^{4+}$  ions are octahedrally (sixfold) coordinated by  $\text{O}^{2-}$  ions, where each of the  $\text{Sr}^{2+}$  ions is surrounded by eight  $\text{TiO}_6$  octahedra.  $\text{SrTiO}_3$  has mixed ionic-covalent bonding properties. Within the  $\text{TiO}_6$  octahedra, hybridization of the O-2p states with the Ti-3d states leads to a pronounced covalent bonding, while the interaction between  $\text{Sr}^{2+}$  and  $\text{O}^{2-}$  ions exhibit ionic bonding character. The following paragraphs are focused on the two low-index polar planes of  $\text{SrTiO}_3$ : (111) and (110) (the (100) is non-polar). Experiments carried out using single crystal  $\text{SrTiO}_3$  (111) and (110) surfaces are described in Chapters 5, 6, and 7 of this document.

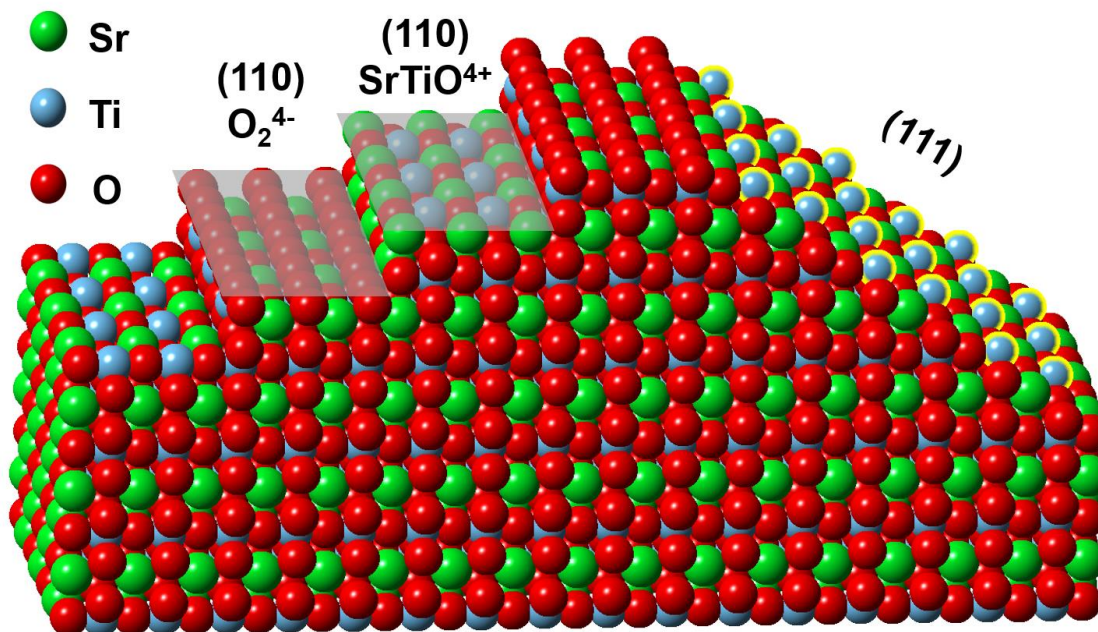


**Figure 2.6.** Schematic of SrTiO<sub>3</sub> viewed along [001] direction. The (110) planes is highlighted by the transparent gray planes. In the picture, along the [110] direction the step height between SrTiO<sup>4+</sup> and O<sub>2</sub><sup>4-</sup> atomic layers are  $3N_{(110)}$  ( $N_{(110)} = 0.138$  nm). The (111) plane is shown in the right. The Ti atoms highlighted by yellow outlines are one atomic layer above the SrO<sub>3</sub><sup>4-</sup> layer, the spacing between these two layers are  $N_{(111)} = 0.112$  nm.

**Surface terminations:** The polar terminations of (111) and (110) SrTiO<sub>3</sub> surfaces are depicted in Fig. 2.6. The (111) surface is terminated by either a Ti<sup>4+</sup> layer or a SrO<sub>3</sub><sup>4-</sup> layer.

The spacing between different layers is  $\frac{1}{2} d_{111} = \frac{\sqrt{3}}{6} a = 0.112$  nm. The (110) group of surfaces can have either a SrTiO<sup>4+</sup> termination or an O<sub>2</sub><sup>4-</sup> termination. Spacing between these two layers is  $\frac{1}{2} d_{110} = \frac{\sqrt{2}}{4} a = 0.138$  nm.

**Surface chemisorption:** Ferrer et al. studied the chemisorption of H<sub>2</sub>, H<sub>2</sub>O and O<sub>2</sub> on SrTiO<sub>3</sub> (111) surface<sup>40</sup>. They found that H<sub>2</sub>, H<sub>2</sub>O and O<sub>2</sub> chemisorbs on a reduced SrTiO<sub>3</sub> (111) plane that has Ti<sup>3+</sup> species stacking over one monolayer at the surface. When the sample was irradiated with band gap light, the oxygen was photodesorbed from the surface.

However, UPS data showed that the hydroxyl concentration increased when the surface was irradiated. On a stoichiometric SrTiO<sub>3</sub> (111) crystal that had no Ti<sup>3+</sup> present, the surfaces were chemically inert. This result is closely related to our experiments as, when we do marker reactions, the SrTiO<sub>3</sub> (111) surface is immersed in an aqueous solution and exposed to UV irradiation (photons exceeding the band gap energy). Therefore, the theoretically Ti<sup>4+</sup> terminated SrTiO<sub>3</sub> (111) surfaces are very likely to bear hydroxyls during photochemical reactions. Considering this, the actual surface charges that influence the band bending during the reaction could be very different from the bulk terminations.

There are two studies focused on water adsorption on (1 × n) reconstructed SrTiO<sub>3</sub> (110) surfaces.<sup>41, 42</sup> Generally, for a surface with highly oxidized Ti sites, most commonly TiO<sub>4</sub> units, the surface was relatively stable and the adsorption of water molecules was weak. However, when there were Ti<sup>3+</sup> sites at the surface, such as for sputtered (1 × 10) surfaces, water was first dissociated at oxygen vacancies, and then water molecules or OH groups were strongly absorbed to the surface.

**Surface reconstructions:** For SrTiO<sub>3</sub> (111) surfaces, a series of (n × n) reconstructions occur after thermal annealing. Experiments found that annealing in atmospheric air produced a highly oxygen enriched (9/5 × 9/5) reconstruction, and annealing in high temperature vacuum environment formed a very reduced TiO (111)-(2 × 2) nanophase on the surface. Annealing in lower O<sub>2</sub> pressures and higher temperatures all contributed to greater oxygen depletion of the (111) surface; the more oxygen depleted the surface was, the higher the concentration of Ti that was found at the surface.<sup>43</sup> There is also a conflicting observation that annealing in oxygen gas produced a trenched and Ti rich surface, while annealing in argon gas produced a Sr rich surface. Compositions were determined by

coaxial impact collision ion scattering spectroscopy (CAICISS).<sup>36,44</sup> This is not surprising because the topography images of SrTiO<sub>3</sub> (111) samples from these two works look quite different, although both samples were annealed in oxygen atmosphere. Differences in experimental details, e.g. samples cleaned by Ar<sup>+</sup> bombardment or ultrasonic cleaning, could determine the final surface structure. Overall, (111) surfaces form a large variety of different stable terminations. Less work has been carried out on the SrTiO<sub>3</sub> (110) surface, but similar observations have been made. When annealed in a UHV environment, the surface adopted (1 × n) and (n × 1) reconstructions. When the (110) surface was annealed in air or oxygen atmospheres between 900 and 1100 °C, (1 × 2), (2 × 5), (3 × 4), and (4 × 4) reconstructions were observed, depending on specifics of the process.<sup>45,46,47</sup>

## 2.6 Photocatalysis with TiO<sub>2</sub>/SrTiO<sub>3</sub> heterostructure

In Chapter 5 and 6, I will show that the surface potential and reactivity of SrTiO<sub>3</sub> (111) and (110) crystals can be controlled through thermal anneals. In Chapter 7, I investigate whether the reactivity of such a SrTiO<sub>3</sub> (111) surface influences the reactivity of a thin TiO<sub>2</sub> overlayer, similar to that reported previously for coated ferroelectrics<sup>48</sup>. Therefore, a detailed description of the energy level diagrams for such a heterostructure is described in this section.

### 2.6.1 ENERGY LEVEL DIAGRAMS OF TiO<sub>2</sub> AND SrTiO<sub>3</sub>

SrTiO<sub>3</sub> is reported to be a n-type semiconductor, likely owing to the oxygen vacancies.<sup>49</sup> Data for its energy levels are taken from Robertson et al.'s reports.<sup>7, 49</sup> Its electron affinity, or the distance from the vacuum level  $E_{\text{vac}}$  to the conduction band edge  $E_c$ , is estimated to be 3.9 eV. The band gap is  $\approx 3.3$  eV, which is an average from all of the reported values. Its Fermi level (called the charge neutral level in some reports) is estimated to be  $\sim 2.6$  eV above the top of its valence band  $E_v$  (or 0.7 eV below the bottom of the conduction band).

TiO<sub>2</sub> is typically an n-type semiconductor, again with oxygen vacancies as the major defect type.<sup>8, 50</sup> For rutile, the band gap is 3.0 eV and its Fermi level is located around 0.2 eV below the bottom of its conduction band  $E_c$ <sup>8</sup>. The rutile's reported work function, or the distance from the vacuum level  $E_{\text{vac}}$  to the Fermi level  $E_F$ , is 4.2 eV.<sup>51</sup> For the anatase phase, the band gap is 3.2 eV<sup>9, 52</sup> and the Fermi level is only  $4.2 \times 10^{-3}$  eV below the conduction band<sup>50</sup>. The reported electron affinity is  $\sim 4.4$  eV.<sup>53</sup> In the experiments described in Chapter 7, heterostructures of (mostly anatase) TiO<sub>2</sub> /SrTiO<sub>3</sub> were fabricated and characterized, and schematics of their respective energy level diagrams, before they are in contact, are depicted in Fig. 2.7

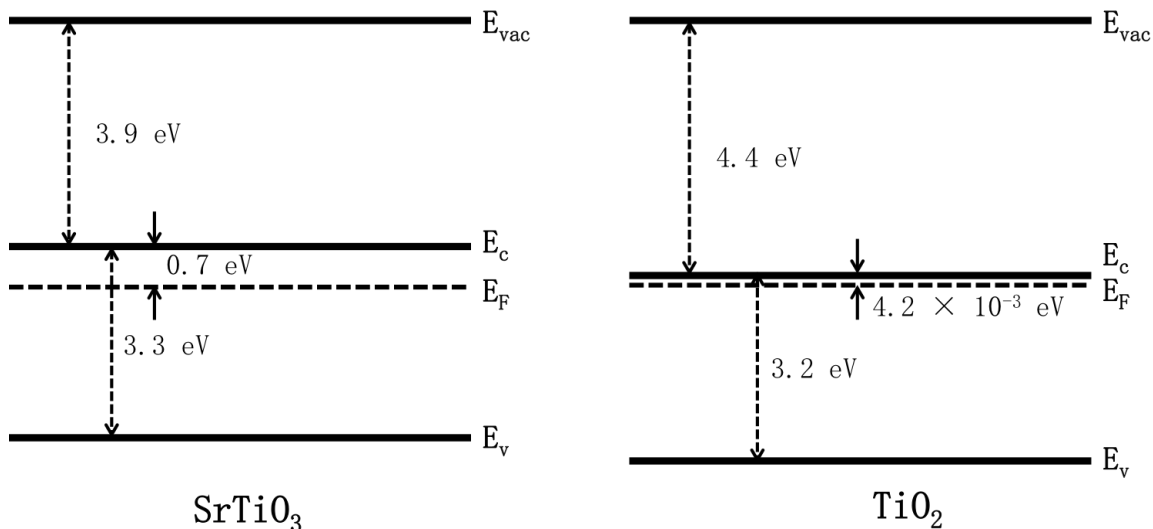


**Figure 2.7.** The energy level diagram of SrTiO<sub>3</sub> on the left and the band structure of anatase TiO<sub>2</sub> on the right. From top down, E<sub>vac</sub> is the vacuum level; E<sub>c</sub> is the conduction band; E<sub>F</sub> is the Fermi level; E<sub>v</sub> is the valence band, for both semiconductors.

### 2.6.2 ENERGY DIAGRAMS OF THIN FILM TiO<sub>2</sub>/SrTiO<sub>3</sub>

When the TiO<sub>2</sub> and SrTiO<sub>3</sub> come into contact, a transfer of charge carriers across the interface takes place until the Fermi levels are aligned. Because the work function of SrTiO<sub>3</sub> (work function  $\phi=4.6$  eV) is slightly larger than anatase ( $\phi=4.4$  eV), electrons flow from TiO<sub>2</sub> to SrTiO<sub>3</sub> to establish equilibrium. This results in SrTiO<sub>3</sub> having downward band bending at the interface and TiO<sub>2</sub> having upward band bending. In the experiment, since the TiO<sub>2</sub> film is in contact with a AgNO<sub>3</sub> solution during the photochemical marker reaction process, the surface condition of the TiO<sub>2</sub> has to be considered. Generally, TiO<sub>2</sub> has upward band bending at surface,<sup>21</sup> creating an energy barrier for electrons getting to the TiO<sub>2</sub>/water interface. The complete energy diagram including TiO<sub>2</sub>/SrTiO<sub>3</sub> and TiO<sub>2</sub>/solution interfaces is drawn in Fig. 2.8, for relatively thick TiO<sub>2</sub> (meaning the two interfaces relax fully into the bulk TiO<sub>2</sub>). The redox level of Ag<sup>+</sup>/Ag is also depicted in the

diagram; it lies within the band gap of  $\text{TiO}_2$ . Therefore, the  $\text{TiO}_2$  is capable for photoreducing  $\text{Ag}^+$  from solution.

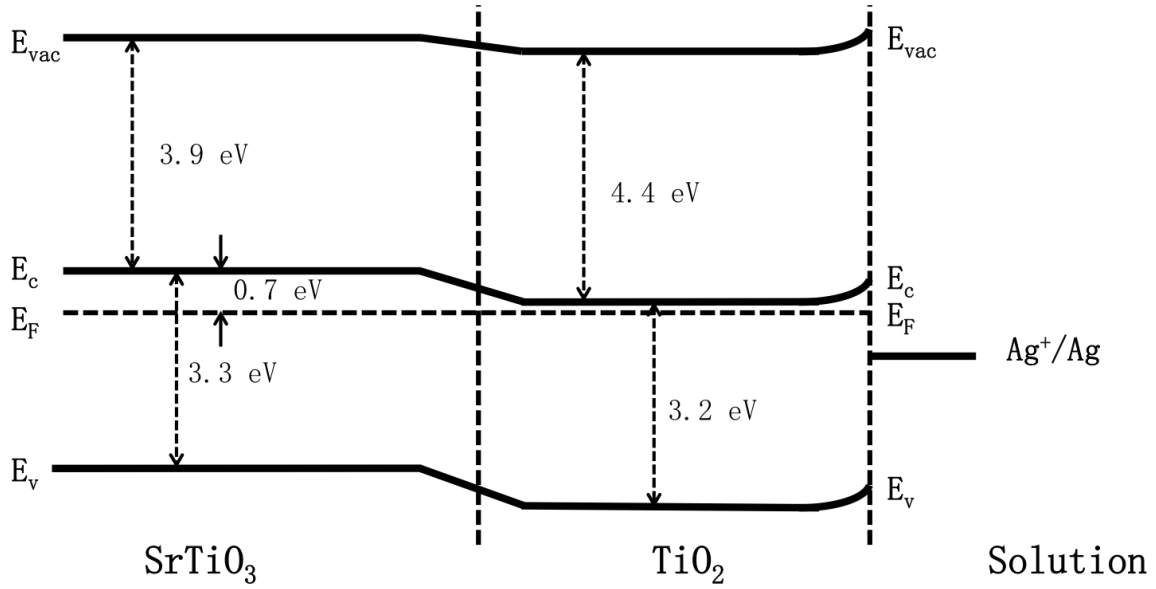


**Figure 2.8.** The energy level diagram of  $\text{TiO}_2/\text{SrTiO}_3$  in contact with solution. At the surface of  $\text{TiO}_2$  film, the band bend upward. The redox level of  $\text{Ag}^+/\text{Ag}$  0.9 eV below conduction band of  $\text{TiO}_2$  (0.8 eV/NHE).

Note that, in general, the thickness of the depletion layers are on the order of 100 nm<sup>21, 54</sup> and the dimension of  $\text{TiO}_2$  drawn in Fig. 2.8 is large enough to accommodate full relaxation of the band bending. However, the heterostructures used in my experiments have only a very thin  $\text{TiO}_2$  film (between 1 and 16nm thick), thinner than the space charge region of  $\text{TiO}_2$ . Because the  $\text{TiO}_2$  film are deposited on  $\text{SrTiO}_3$  substrate, which is supposed to have polar terminations, surface charges at  $\text{TiO}_2/\text{SrTiO}_3$  interfaces should also be considered in depicting the band diagram. Fig. 2.9 shows potential energy level diagrams for  $\text{TiO}_2/\text{SrTiO}_3$  heterostructures, with ultra thin  $\text{TiO}_2$  on two different  $\text{SrTiO}_3$  (111) polar terminations.

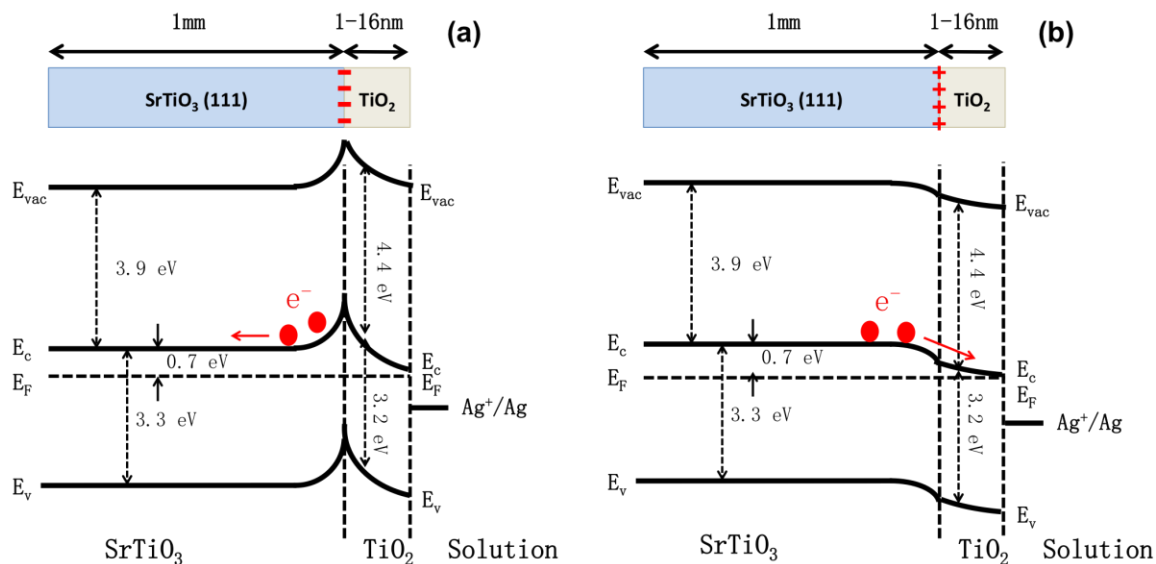


**Figure 2.9.** The energy level diagrams of a SrTiO<sub>3</sub> (111) substrate and a anatase TiO<sub>2</sub> film in contact with solution in the case of (a) negatively charged and (b) positively charged termination. The bands at the TiO<sub>2</sub>/SrTiO<sub>3</sub> interface bend upward in (a) and downward in (b) corresponding to the sign of surface charges. Band bending cause electrons in case (a) is repelled from the interface and electrons in case (b) is driven to the interface then diffuse to the TiO<sub>2</sub>/solution interface where photochemical reactions happened.

As noted before, the ideal unreconstructed SrTiO<sub>3</sub> (111) surfaces are terminated by either Ti<sup>4+</sup> layer or SrO<sub>3</sub><sup>4-</sup> layer. At the surfaces of negatively charged terminations as shown in Fig. 2.9(a), SrTiO<sub>3</sub>'s electron energy levels will bend upward at TiO<sub>2</sub>/SrTiO<sub>3</sub> interface, creating a potential barrier to prevent electrons in the conduction band from migrating to the TiO<sub>2</sub> film. Therefore, when the sample was illuminated by band gap irradiation, photoelectrons created in the SrTiO<sub>3</sub> are repelled from the interface into the interior of the SrTiO<sub>3</sub> and probably recombine with a hole. The opposite occurs at the positively charged interface (Fig. 2.9(b)). In this situation, the conduction band edge bends downward, facilitating the migration of electrons to the TiO<sub>2</sub> film. The excited electrons are driven to the TiO<sub>2</sub> film by the potential gradient at TiO<sub>2</sub>/SrTiO<sub>3</sub> interface, then through the TiO<sub>2</sub> film to reach the surface where they can participate in photochemical reactions. I

will test whether photochemical reactions support the existence of such band bending in  
Chapter 7.

## Reference

1. D. I. Kondarides, V. M. Daskalaki, A. Patsoura, and X. E. Verykios, "Hydrogen production by photoinduced reforming of biomass components and derivatives at ambient conditions," *Catalysis Letters*, 122[1-2] 26-32 (2008).
2. W. Clark and A. Vondjidis, "An infrared study of the photocatalytic reaction between titanium dioxide and silver nitrate," *Journal of Catalysis*, 4[6] 691-96 (1965).
3. J.-M. Herrmann, J. Disdier, and P. Pichat, "Photocatalytic deposition of silver on powder titania: consequences for the recovery of silver," *Journal of Catalysis*, 113[1] 72-81 (1988).
4. K. Tanaka, K. Harada, and S. Murata, "Photocatalytic deposition of metal ions onto TiO<sub>2</sub> powder," *Solar Energy*, 36[2] 159-61 (1986).
5. J. Torres and S. Cervera-March, "Kinetics of the photoassisted catalytic oxidation of Pb (II) in TiO<sub>2</sub> suspensions," *Chemical engineering science*, 47[15] 3857-62 (1992).
6. C. Gleitzer, J. Nowotny, and M. Rekas, "Surface and bulk electrical properties of the hematite phase Fe<sub>2</sub>O<sub>3</sub>," *Applied Physics A*, 53[4] 310-16 (1991).
7. J. Robertson, "Electronic structure and band offsets of high-dielectric-constant gate oxides," *Mrs Bulletin*, 27[03] 217-21 (2002).
8. R. G. Breckenridge and W. R. Hosler, "Electrical properties of titanium dioxide semiconductors," *Physical Review*, 91[4] 793 (1953).
9. H. Tang, H. Berger, P. Schmid, and F. Levy, "Optical properties of anatase (TiO<sub>2</sub>)," *Solid State Communications*, 92[3] 267-71 (1994).
10. S. Pati, L. H. Prentice, G. Tranell, and K. S. Brinkman, "Ferroelectric-Enhanced Photocatalysis with TiO<sub>2</sub>/BiFeO<sub>3</sub>," *Energy Technology 2014: Carbon Dioxide Management and Other Technologies* 15 (2013).
11. L. Li, P. A. Salvador, and G. S. Rohrer, "Photocatalysts with internal electric fields," *Nanoscale*, 6[1] 24-42 (2014).
12. D. Tiwari and S. Dunn, "Photochemistry on a polarisable semi-conductor: what do we understand today?," *Journal of materials science*, 44[19] 5063-79 (2009).
13. J. L. Giocondi and G. S. Rohrer, "The influence of the dipolar field effect on the photochemical reactivity of Sr<sub>2</sub>Nb<sub>2</sub>O<sub>7</sub> and BaTiO<sub>3</sub> microcrystals," *Topics in catalysis*, 49[1-2] 18-23 (2008).
14. A. M. Schultz, Y. Zhang, P. A. Salvador, and G. S. Rohrer, "Effect of Crystal and Domain Orientation on the Visible-Light Photochemical Reduction of Ag on BiFeO<sub>3</sub>," *ACS applied materials & interfaces*, 3[5] 1562-67 (2011).
15. B. Jaffe, "Piezoelectric ceramics," Vol. 3. Elsevier, (2012).
16. Y. Inoue, K. Sato, K. Sato, and H. Miyama, "Photoassisted water decomposition by ferroelectric lead zirconate titanate ceramics with anomalous photovoltaic effects," *The Journal of Physical Chemistry*, 90[13] 2809-10 (1986).
17. A. Wander, F. Schedin, P. Steadman, A. Norris, R. McGrath, T. Turner, G. Thornton, and N. Harrison, "Stability of polar oxide surfaces," *Physical review letters*, 86[17] 3811 (2001).
18. A. Rohrbach, J. Hafner, and G. Kresse, "Ab initio study of the (0001) surfaces of hematite and chromia: Influence of strong electronic correlations," *Physical Review B*, 70[12] 125426 (2004).

19. E. Heifets, W. Goddard III, E. Kotomin, R. Eglitis, and G. Borstel, "Ab initio calculations of the SrTiO<sub>3</sub> (110) polar surface," *Physical Review B*, 69[3] 035408 (2004).
20. J. S. Lee, "Photocatalytic water splitting under visible light with particulate semiconductor catalysts," *Catalysis surveys from Asia*, 9[4] 217-27 (2005).
21. A. L. Linsebigler, G. Lu, and J. T. Yates Jr, "Photocatalysis on TiO<sub>2</sub> surfaces: principles, mechanisms, and selected results," *Chemical reviews*, 95[3] 735-58 (1995).
22. J. L. Giocondi and G. S. Rohrer, "Structure Sensitivity of Photochemical Oxidation and Reduction Reactions on SrTiO<sub>3</sub> Surfaces," *Journal of the American Ceramic Society*, 86[7] 1182-89 (2003).
23. W. Mönch, "Semiconductor surfaces and interfaces," Vol. 26. Springer Science & Business Media, (2013).
24. S. V. Kalinin, D. A. Bonnell, T. Alvarez, X. Lei, Z. Hu, R. Shao, and J. H. Ferris, "Ferroelectric lithography of multicomponent nanostructures," *Advanced Materials*, 16[9 - 10] 795-99 (2004).
25. S. V. Kalinin, D. A. Bonnell, T. Alvarez, X. Lei, Z. Hu, J. Ferris, Q. Zhang, and S. Dunn, "Atomic polarization and local reactivity on ferroelectric surfaces: a new route toward complex nanostructures," *Nano Letters*, 2[6] 589-93 (2002).
26. A. Bhardwaj, N. V. Burbure, A. Gamalski, and G. S. Rohrer, "Composition Dependence of the Photochemical reduction of Ag by Ba<sub>1-x</sub>Sr<sub>x</sub>TiO<sub>3</sub>," *Chemistry of Materials*, 22[11] 3527-34 (2010).
27. R. Glemza and R. Kokes, "Chemisorption of oxygen on zinc oxide," *The Journal of Physical Chemistry*, 69[10] 3254-62 (1965).
28. G. Zwicker, K. Jacobil, and J. Cunningham, "Temperature programmed desorption of polar adsorbates from (1010),(0001) and (0001) ZnO surfaces," *International Journal of Mass Spectrometry and Ion Processes*, 60[1] 213-23 (1984).
29. W. Melitz, J. Shen, A. C. Kummel, and S. Lee, "Kelvin probe force microscopy and its application," *Surface Science Reports*, 66[1] 1-27 (2011).
30. L. Pauling and S. B. Hendricks, "The crystal structures of hematite and corundum," *Journal of the American Chemical Society*, 47[3] 781-90 (1925).
31. T. Bak, J. Nowotny, M. Rekas, and C. Sorrell, "Photoelectrochemical hydrogen generation from water using solar energy. Materials-related aspects," *International journal of hydrogen energy*, 27[10] 991-1022 (2002).
32. R. M. Cornell and U. Schwertmann, "The iron oxides: structure, properties, reactions, occurrences and uses." John Wiley & Sons, (2003).
33. H. Guo and A. S. Barnard, "Thermodynamic modelling of nanomorphologies of hematite and goethite," *Journal of Materials Chemistry*, 21[31] 11566-77 (2011).
34. R. L. Kurtz and V. E. Henrich, "Surface electronic structure and chemisorption on corundum transition-metal oxides:  $\alpha$ -Fe<sub>2</sub>O<sub>3</sub>," *Physical Review B*, 36[6] 3413 (1987).
35. P. Liu, T. Kendelewicz, G. E. Brown, E. J. Nelson, and S. A. Chambers, "Reaction of water vapor with  $\alpha$ -Al<sub>2</sub>O<sub>3</sub> (0001) and  $\alpha$ -Fe<sub>2</sub>O<sub>3</sub> (0001) surfaces: Synchrotron X-ray photoemission studies and thermodynamic calculations," *Surface Science*,

- 417[1] 53-65 (1998).
36. V. Barrón and J. Torrent, "Surface hydroxyl configuration of various crystal faces of hematite and goethite," *Journal of Colloid and Interface Science*, 177[2] 407-10 (1996).
  37. P. Cox, "The surface science of metal oxides." Cambridge university press, (1996).
  38. M. A. Henderson, S. A. Joyce, and J. R. Rustad, "Interaction of water with the (1 × 1) and (2 × 1) surfaces of  $\alpha$ -Fe<sub>2</sub>O<sub>3</sub> (012)," *Surface Science*, 417[1] 66-81 (1998).
  39. K. S. Tanwar, J. G. Catalano, S. C. Petitto, S. K. Ghose, P. J. Eng, and T. P. Trainor, "Hydrated  $\alpha$ -Fe<sub>2</sub>O<sub>3</sub> surface structure: Role of surface preparation," *Surface science*, 601[12] L59-L64 (2007).
  40. S. Ferrer and G. Somorjai, "UPS and XPS studies of the chemisorption of O<sub>2</sub>, H<sub>2</sub> and H<sub>2</sub>O on reduced and stoichiometric SrTiO<sub>3</sub> (111) surfaces; The effects of illumination," *Surface Science*, 94[1] 41-56 (1980).
  41. W. Li, S. Liu, S. Wang, Q. Guo, and J. Guo, "The Roles of Reduced Ti Cations and Oxygen Vacancies in Water Adsorption and Dissociation on SrTiO<sub>3</sub> (110)," *The Journal of Physical Chemistry C*, 118[5] 2469-74 (2014).
  42. Z. Wang, X. Hao, S. Gerhold, Z. Novotny, C. Franchini, E. McDermott, K. Schulte, M. Schmid, and U. Diebold, "Water Adsorption at the Tetrahedral Titania Surface Layer of SrTiO<sub>3</sub> (110)-(4 × 1)," *The Journal of Physical Chemistry C*, 117[49] 26060-69 (2013).
  43. B. C. Russell and M. R. Castell, "Surface of sputtered and annealed polar SrTiO<sub>3</sub>(111): TiO<sub>x</sub>-rich (n × n) reconstructions," *Journal of Physical Chemistry C*, 112[16] 6538-45 (2008).
  44. S. Sekiguchi, M. Fujimoto, M.-G. Kang, S. Koizumi, S.-B. Cho, and J. Tanaka, "Structure analysis of SrTiO<sub>3</sub> (111) polar surfaces," *Japanese journal of applied physics*, 37[7R] 4140 (1998).
  45. J. Brunen and J. Zegenhagen, "Investigation of the SrTiO<sub>3</sub> (110) surface by means of LEED, scanning tunneling microscopy and Auger spectroscopy," *Surface science*, 389[1] 349-65 (1997).
  46. A. Gunhold, K. Gömann, L. Beuermann, V. Kempter, G. Borchardt, and W. Maus-Friedrichs, "Changes in the surface topography and electronic structure of SrTiO<sub>3</sub> (110) single crystals heated under oxidizing and reducing conditions," *Surface science*, 566 105-10 (2004).
  47. A. Subramanian and L. Marks, "Surface crystallography via electron microscopy," *Ultramicroscopy*, 98[2] 151-57 (2004).
  48. Y. Zhang, A. M. Schultz, P. A. Salvador, and G. S. Rohrer, "Spatially selective visible light photocatalytic activity of TiO<sub>2</sub>/BiFeO<sub>3</sub> heterostructures," *Journal of Materials Chemistry*, 21[12] 4168-74 (2011).
  49. J. Robertson and C. Chen, "Schottky barrier heights of tantalum oxide, barium strontium titanate, lead titanate, and strontium bismuth tantalate," *Applied Physics Letters*, 74[8] 1168-70 (1999).
  50. L. Forro, O. Chauvet, D. Emin, L. Zuppiroli, H. Berger, and F. Levy, "High mobility n - type charge carriers in large single crystals of anatase (TiO<sub>2</sub>)," *Journal of Applied Physics*, 75[1] 633-35 (1994).
  51. A. Imanishi, E. Tsuji, and Y. Nakato, "Dependence of the work function of TiO<sub>2</sub>

- (rutile) on crystal faces, studied by a scanning auger microprobe," *The Journal of Physical Chemistry C*, 111[5] 2128-32 (2007).
52. H. Tang, F. Levy, H. Berger, and P. Schmid, "Urbach tail of anatase TiO<sub>2</sub>," *Physical Review B*, 52[11] 7771 (1995).
53. F. Lenzmann, J. Krueger, S. Burnside, K. Brooks, M. Grätzel, D. Gal, S. Rühle, and D. Cahen, "Surface photovoltage spectroscopy of dye-sensitized solar cells with TiO<sub>2</sub>, Nb<sub>2</sub>O<sub>5</sub>, and SrTiO<sub>3</sub> nanocrystalline photoanodes: Indication for electron injection from higher excited dye states," *The Journal of Physical Chemistry B*, 105[27] 6347-52 (2001).
54. W. J. Albery and P. N. Bartlett, "The transport and kinetics of photogenerated carriers in colloidal semiconductor electrode particles," *Journal of the Electrochemical Society*, 131[2] 315-25 (1984).

## Chapter 3 Experimental

*The purpose of this chapter is to describe the general sample preparation method and characterization techniques used in this research, while specifics are also given in the following results chapters. The main methods for sample preparation covered in this chapter are solid-state reaction of ceramics and pulsed laser deposition of thin films. The characterization techniques addressed include photochemical activity determination, optical microscopy, scanning probe microscopy, orientation determination, and the thin film phase and thickness characterization.*

### 3.1 Sample Preparation

#### 3.1.1 SOLID-STATE REACTION & SAMPLE ANNEALING

To study how the photochemical activity and surface potential of hematite depend on substrate orientation, ceramic polycrystalline pellets were fabricated via a solid state route<sup>1</sup>. First, Fe<sub>2</sub>O<sub>3</sub> powder (Alfa Aesar 99.945 %) and 1.5 wt% polyethylene glycol binder (PEG, MW8000) were ball milled overnight in ethanol using yttria-stabilized zirconia grinding media. The slurry was then put in a drying oven at 85 °C to evaporate the ethanol.

The dried powders were put in a stainless steel die and compressed into pellets under a load of 5000 pounds/cm<sup>2</sup>. The pellets were  $\approx$  1 cm in diameter and 2-3 mm in thickness. Then, the pellets were placed into an alumina crucible (99.6%) and covered with excess of hematite powder. The pellets were annealed at 600 °C for 12 hours to burn off the binder and then sintered at 1250 °C for 48 hours. The heating and cooling rates were 10 °C/min. The random texture of the as synthesized Fe<sub>2</sub>O<sub>3</sub> polycrystalline pellets allows the properties to be measured across the entire range of possible orientations.

After synthesis, the Fe<sub>2</sub>O<sub>3</sub> pellets were polished using a Logitech auto-polisher (Logitech PM5, Glasgow, Scotland). First, the pellets were lapped flat with an aqueous Al<sub>2</sub>O<sub>3</sub> suspension (grain size = 3 μm). Because Fe<sub>2</sub>O<sub>3</sub> is a hard material, a typical time for lapping flat is around 1 hour. After lapping flat, the pellets were polished with a 0.02 μm colloidal SiO<sub>2</sub> (Buehler) or 0.05 μm Al<sub>2</sub>O<sub>3</sub> (Allied) and a polyurethane polishing pad for 4-5 hours, to result in surfaces with roughnesses < 10 nm. The polished pellets were carefully washed by DI water. Note that, if the sample was polished using SiO<sub>2</sub> suspension, it was first immersed in a 10 % NaOH solution and ultrasonically cleaned for 1 hour to dissolve SiO<sub>2</sub> residue on the surface before DI water washing. To repair damage from polishing and improve surface crystallinity, the polished and cleaned Fe<sub>2</sub>O<sub>3</sub> pellets were heated at 10 °C/min to 1100 °C, annealed for 6 hours, and cooled to room temperature at  $\sim$ 10 °C/min.

For the experiments involving SrTiO<sub>3</sub>, we used commercially available single side polished SrTiO<sub>3</sub> (111) and (110) single crystals (MTI company,  $\pm$  0.5 °, roughness < 15 Å). The sample was sonicated for 10 min, first in an acetone and then a methanol bath. The sample was annealed above 1000 °C in a covered alumina crucible. The SrTiO<sub>3</sub> (111) and (110) surface developed a step and terrace structure after annealing, leaving the

terraces atomically flat. To prevent possible contamination from the muffle furnace, samples were contained in covered high-purity alumina combustion boats while annealing. No other precipitate or contamination phases were found based on XRD and XPS results.

### **3.1.2 PULSED LASER DEPOSITION (PLD)**

Atomically flat TiO<sub>2</sub> thin films from 1 to 16 nm thick were grown using pulsed laser deposition (PLD). Deposition parameters are adopted, with minor adjustments, from previous work in which TiO<sub>2</sub> films were grown on BiFeO<sub>3</sub> and BaTiO<sub>3</sub> substrates.<sup>2, 3, 4</sup> A schematic illustration of a PLD set up is depicted in Fig. 3.1. The KrF laser (248 nm wavelength) is first focused through lenses before entering the chamber. The focused laser enters the vacuum chamber through the quartz optical window and hits the rotating target surface. A plume of the target material is ablated in a direction normal to the target surface. The size and shape of the plume in the vacuum chamber is determined by the energy density of the incident laser and the vacuum pressure. The plume's shape and size directly determines the amount of target material arriving at the substrate surface for film growth. Therefore, it directly affects the growth rate and roughness of the film surface. The substrate is glued to the substrate holder by silver paste. During the deposition process, the substrate holder heats the substrate to a designated temperature. As the plume reaches the substrate, the target material diffuses on the surface and crystallizes to form a film.

A deposition chamber from Neocera (Beltsville, MD) was used for all film growth described in this dissertation. A KrF excimer laser (Coherent, Santa Clare, CA, wavelength = 248 nm) was used for ablation. Before depositions, the substrate was sonicated for 10 minutes each in an acetone and methanol bath. The cleaned substrate was affixed to the

substrate holder using silver paste cured at 120 °C. The target was mounted and the target to substrate distance was fixed at 6 cm in the deposition chamber. The chamber was then evacuated to a pressure of  $\sim 10^{-5}$  Torr and the substrate heated to the designated temperature with 15 °C/min heating rate. Once the temperature was reached, a flow of oxygen was introduced to the chamber to maintain the desired pressure of deposition. For all deposition process, the output laser energy density was set to 2 J/cm<sup>2</sup>. Before actual deposition, the target was cleaned and conditioned for 15 minutes by pulsing the laser at 3 Hz. A shield was put between the target and substrate to block the plume from reaching the surface. After conditioning, the shield was removed, and the target was hit with a predetermined number of laser pulses at specified rates to deposit the films. Immediately after deposition was completed, the chamber was sealed, and oxygen gas was vented into the chamber to minimize the number of oxygen vacancies. Then the chamber was cooled to room temperature using a 25 °C/min cooling rate.

The substrate temperature and the pressure of oxygen during deposition are two key parameters that control the phase of film, while the laser energy density, number, and rate of laser pulses control the film thickness and roughness. The exact deposition conditions for TiO<sub>2</sub> films were adopted from previous studies,<sup>2,3,4</sup> with minor adjustments. In general, TiO<sub>2</sub> films were deposited at 700 °C, in 30 ~ 40 mTorr O<sub>2</sub>, with the laser pulsed at 3 Hz. Although the output laser density was set to 160 mJ/pulse ( $\approx 2$  J/cm<sup>2</sup>), it was decreased to less than half of the original energy because residue on the quartz window absorbed some of the energy. However, the deposition rate using the dirty quartz window produced a very low reproducible growth rate resulting in atomically flat films, so we did not modify the procedure (i.e., we did not remove the residue).

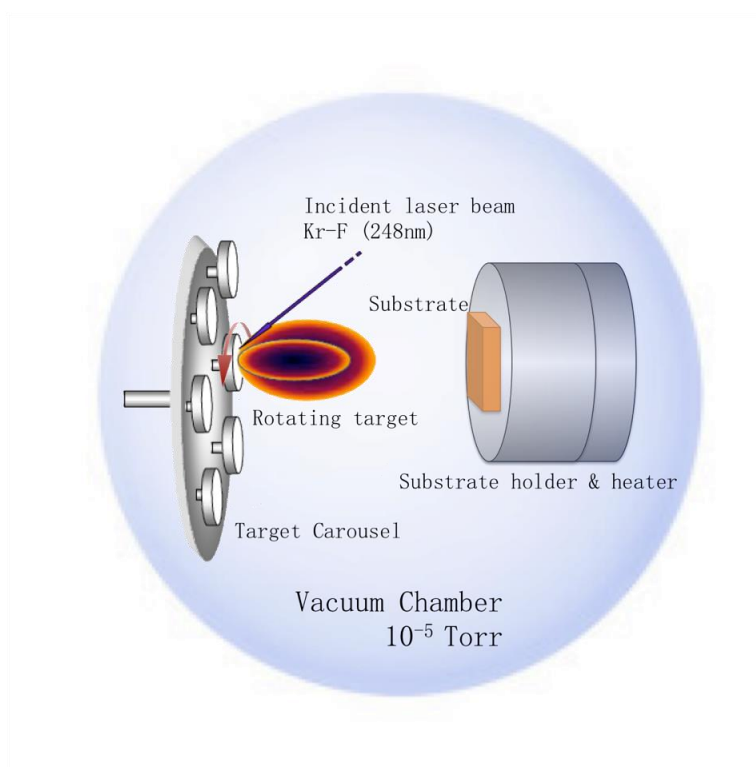
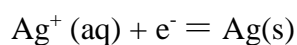


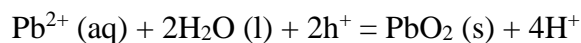
**Figure 3.1.** Schematic of the pulsed laser deposition vacuum chamber used in this work, showing the location of the substrate, target and incident laser beam.

## 3.2 Characterization Techniques

### 3.2.1 MARKER REACTION

Silver-reduction and lead-oxidation marker reactions have been used for a long time to characterize the photoreduction and photooxidation reactivity of many materials, including  $\text{TiO}_2$ ,<sup>5, 6</sup>  $\text{BaTiO}_3$ ,  $\text{SrTiO}_3$ ,<sup>7</sup>  $\text{BiFeO}_3$ <sup>8</sup> and  $\text{BiVO}_4$ .<sup>9</sup> The reduction of  $\text{Ag}^+$  by photoelectrons and oxidation of  $\text{Pb}^{2+}$  by photoholes are described by the following reactions:





Since both reactions leave insoluble products on the surface, a photocatalyst's surface will have Ag or Pb-containing particles deposited after reaction corresponding to the photoreduction and photooxidation sites, respectively. Note that the produced Ag or Pb-containing particles can be removed after sonicating in acetone or methanol bath for 10 minutes, followed by swiping with cotton swabs. The cleaned surface can be repeatedly used for other photoreactions. The counter reaction for silver reduction (lead oxidation) is the oxidation (reduction) of water, but the produced  $\text{O}_2$  ( $\text{H}_2$ ) is dissolved into the solution and cannot be detected in the experiment.

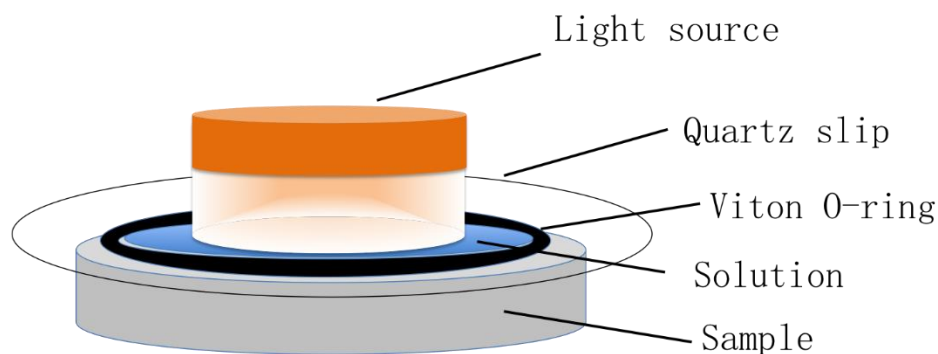


**Figure 3.2.** Schematic of photochemical marker reaction

The setup for the photochemical marker reaction experiments is depicted in Fig. 3.2. A Viton O-ring (> 1 mm thick) was placed on the sample surface and the interior volume was filled with 0.115 M  $\text{AgNO}_3$  or  $\text{Pb}(\text{CH}_3\text{COO})_2$  solution. A quartz slip was placed on top, sealing the solution in the O-ring by capillarity without an air bubble. Then, a commercially available blue LED light source ( $\lambda_{\text{peak}} = 470$  nm, Philips Lumileds, San Jose, CA) or a mercury arc lamp (Newport, Irvine, CA) was placed with its lens facing downward and in contact with the quartz slip. For all experiments, the power of the blue LED was set to 3 W and the mercury lamp's power was set to 300 W. After switching off

the blue LED, the quartz cover slip and the O-ring were removed, and the sample was immersed into de-ionized water twice to wash off remaining solution. The surface was then dried using a 99.995% nitrogen gas stream. The light source used for each experiment was determined by the sample's band gap. Because hematite has a narrow band gap of 1.9 eV  $\sim$  2.3 eV,<sup>10</sup> it is a good absorber of visible light, and the blue LED light was used in the photochemical marker reactions. TiO<sub>2</sub> and SrTiO<sub>3</sub> have wider band gaps and can only absorb UV light, so the mercury lamp was used for reactions on SrTiO<sub>3</sub> single crystals and TiO<sub>2</sub>/SrTiO<sub>3</sub> heterostructure.

### **3.2.2 CHARACTERIZATION OF SURFACES AFTER MARKER REACTION**

After the marker reactions were carried out, the distribution of products (Ag or PbO<sub>2</sub>) were mapped to determine the photoreduction or photooxidation sites on a sample surface. Two main characterization techniques that were used in this dissertation were atomic force microscopy (AFM) and dark field optical microscopy.

AFM measures the surface topography by sensing the force between a sharp tip and the (much flatter) sample. As the tip moves across the surface and the local height of the sample surface changes, the amplitude of the tip's oscillation changes and this alters the intensity of the laser reflected from the back of the tip. This change in the location of the laser is sensed by a photodetector and the microscope adjusts the height of the tip to until the previous (target) oscillation amplitude is restored. The height adjustment is recorded, which corresponds to the height change in the sample surface. The standard deviation of such height measurements is around 1 Å, allowing reaction products significantly larger than this to be detected. However, mapping a reacted surface by AFM is limited by the rate

of image acquisition and the lateral field of view. The maximum scan rate for an AFM topography measurement with satisfactory image quality is 30  $\mu\text{m/s}$  and the maximum image area (without forming a montage) is limited to 100  $\mu\text{m} \times 100 \mu\text{m}$ . Therefore, using AFM to characterize large area surfaces is time-consuming; if a sample has a large grain size, a single image only covers a few grains.

An AFM (NTegra or Solver-NEXT, Russia) was used to examine the surface topography of all hematite,  $\text{SrTiO}_3$ , and heterostructured sample surfaces, both before and after marker reactions. Sharpened pyramidal silicon probes (NSG10 or FMG01, nt-mdt, Russia) were used to map the surface in a semi-contact mode. In this thesis, the local height of the surface is represented in two dimensional color images by the color brightness. One example of an AFM topography image of a reacted surface is shown in Fig. 3.3(a). The sample was an annealed hematite polycrystal after a silver photoreduction marker reaction was conducted under blue LED illumination. The bright contrast in the image is attributed to the silver particles, selectively deposited on some of the grains. The heights of silver particles can be directly measured from the AFM height profiles. From the image, the spatial selection is obvious. The photoreduction reactive grains almost have no reactant deposit on it. Therefore, the migration of reactants from neighboring grains is unlikely. Marker reactions only happen locally, and are a straightforward way to highlight the photoreduction and photooxidation sites on surface.

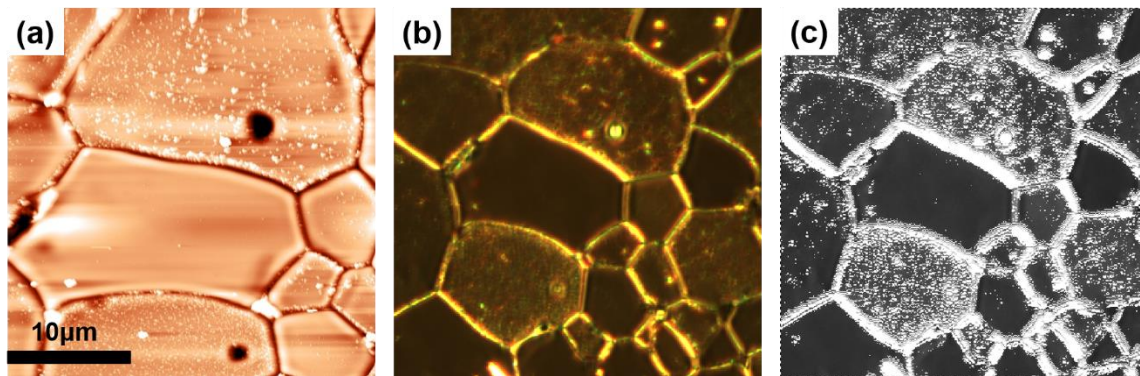


**Figure 3.3.** (a) AFM topography image, (b) dark field optical microscopy image and (c) processed dark field optical microscopy image of the same area of the surface of an annealed hematite polycrystal after a silver marker reaction.

To observe the distribution of reaction products over a much larger field of view, dark field optical microscopy was used to image  $\text{Fe}_2\text{O}_3$  surfaces after silver reduction reactions. In dark field microscopy, the contrast is created using light scattered from the sample surface and captured in the objective lens. It is ideal for revealing abrupt height change on sample surfaces. Rather than illuminating the sample with a full cone of light, as done in bright field microscopy, the condenser lens forms a hollow cone in dark field microscopy, resulting in weak contrast in dark field microscopy. An example dark field optical microscopy image is shown in Fig. 3.3(b). The grain boundaries and silver particles appear as bright contrast in the image because they scatter light (here using yellow light illumination), and dark field microscopy yields bright contrast for strongly scattering regions. The hematite grains without silver deposits are (nearly) atomically flat and do not scatter light strongly (they reflect it) and, therefore, have dark (black) contrast.

To improve the contrast and make it possible to quantify the amount of product on each grain, we processed the dark field image using Photoshop and Matlab software. First, the acquired dark field microscopy image was converted in to a black and white image

using Photoshop. We found that in the black and white microscopy image, the grey value of pixels in the silver particles were generally greater than the neighboring pixels that belong to the grain surface by six brightness values (on a zero to 255 brightness scale). According to this, a Matlab program was used to set the pixels that belongs to silver particles and grain boundaries to be white (gray value=255). The resulting image processed from that in Fig. 3.3(b) is shown in Fig. 3.3(c). The contrast in Fig. 3.3(c) is greatly enhanced compared to the original image in Fig. 3.3(b). Below is the Matlab program script:

```
A=imread('Image.tif');
for i=2:(size(A,1)-2)
    for j=2:(size(A,2)-2)
        if A(i,j)>(A(i-1,j)+20)
            A(i,j)=255;
        else if A(i,j)>(A(i+1,j)+20)
            A(i,j)=255;
        end
    end
end
end
imshow(A)
imwrite(A,'ProcessedImage.png','png');
```

When compared to the AFM image of the same area (Fig. 3.3(a)), the white pixels in the processed image (Fig. 3.3(c)) represent well the distribution of silver particles. The area that has more silver particles according to the AFM image, has a higher density of white pixels in the processed image. Moreover, the processed image allows us to quantify the reactivity by calculating the percentage of white pixels for each grain. The physical meaning for the fractional white pixel value is the percentage of a grain area that is covered by silver particles. For this calculation, white pixels associated with, or close to, the grain

boundaries were excluded for the statistics; in other words, silver particles at the grain boundaries were ignored. This is because, first, contrast from particles and grain boundaries are hard to distinguish, and second, light absorption in the grain boundary area is different than other flat facets, so that the photochemical activity at grain boundaries cannot comparing with others.

### **3.2.3 KELVIN PROBE MICROSCOPY: SURFACE POTENTIAL MEASUREMENT**

Because my hypothesis is that the specific photochemical reaction sites are directly correlated to the local surface potential of photocatalysts, including polycrystalline  $\text{Fe}_2\text{O}_3$  and  $\text{SrTiO}_3$  (111) and (110) single crystals, a method to quantify the local surface potential is needed. The local potential of the surface was measured by amplitude modulated Kelvin probe force microscopy (AM-KFM). The KFM technique is a two pass scanning probe force microscopy technique, essentially a method based on AFM. In the first pass, the surface height is measured by conventional AFM in semi-contact mode. In the second pass, the conducting AFM probe is lifted to a fixed distance from the surface. If the tip and the sample have different work functions (Fig. 3.4(a)) or the sample is charged (Fig. 3.4(b)), there is a Coulomb force between the conducting tip and the sample. To enhance the Coulomb interaction and make it easier to detect, an AC voltage is applied at a frequency that causes the probe to vibrate. Then an adjustable DC voltage is applied to fully compensate the charges, so the Coulomb force is nullified and the vibration ceases. The offset DC voltage reflects the sample's local work function and surface charges. The

surface potential that is measured is equal in magnitude and opposite in sign to the DC voltage (Fig. 3.4(c)).<sup>11, 12</sup>

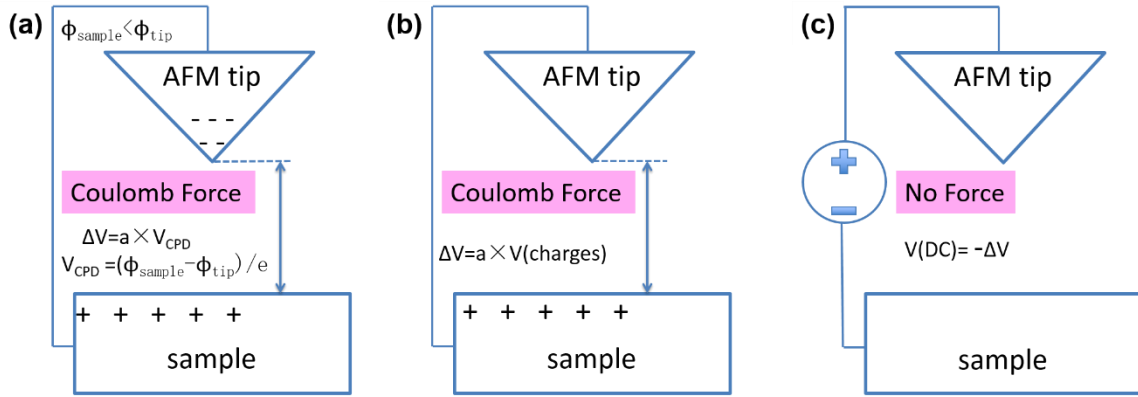


**Figure 3.4.** Schematic illustration of KFM working theory. (a) Coulomb force between tip and sample of different work functions (assume  $\phi_{\text{sample}} < \phi_{\text{tip}}$ ) (b) Coulomb force for a charged surface (c) external DC voltage applied to nullify the force.

For typical KFM imaging, we use conductive probes coated by TiN (FMG01/TiN, nt-mdt, Russia), PtIr (NSG01/Pt by nt-mdt, Russia), or PtCr (Tap190E-G by BudgetSensor, Bulgaria). During the second pass that measures surface potential, the probe was lifted 10 nm above the surface, and the scan rate was set between 6-10  $\mu\text{m}/\text{sec}$ .

For some measurements (acquired using NTegra AFM, Russia) in the hematite project (Chapter 4), I found the output surface potential value was sometimes (rather unpredictably) inverted from the expectations (either by machine function or environmental conditions<sup>13, 14, 15, 16</sup>). In other words, when the same surface was imaged, specific features observed with high and low potential in one measurement had opposite potentials in a subsequent measurement. Further, a Au-Pt standard sample was used to calibrate the KFM for every experiment, and the inversion was observed for the control. Because the work function of Au (5.1 eV) is smaller than that of Pt (5.7 eV),<sup>17</sup> the surface potential value should be more positive for Au than for Pt,<sup>18, 19</sup> according to Eq. 2.1 in §

2.4. However, the correct relative values was only observed in 30 % of the experiments (during this project only). In the remaining 70 %, Pt had a more positive potential than did Au. Whenever the potential values of Au and Pt in the control sample were reversed (in order and in sign), so were the potential values from the Fe<sub>2</sub>O<sub>3</sub> grains. Therefore, in the result chapter of hematite project (§ 4), we report only data from datasets exhibiting inverted (reversed) control values, because these represented the majority (70 %) of experiments. The values reported § 4 were, however, corrected (sign inverted) such that they agree with the expectations and can be discussed in a consistent fashion with other results. It should be noted that the data from the Fe<sub>2</sub>O<sub>3</sub> grains from the 30 % of the experiments in which the potentials of the control sample had the expected order were still consistent with the more extensive sign-inverted data set presented in §4.

### **3.2.4 ELECTRON BACKSCATTER DIFFRACTION**

Electron backscatter diffraction (EBSD) is a scanning electron microscopy (SEM) technique capable of mapping the crystallographic orientation of a crystalline sample surface.<sup>20, 21</sup> It was employed in this work to determine the crystallographic orientation of individual grains in polycrystalline hematite.

The hematite polycrystal was mounted on a stub with carbon tape; grounded carbon tape was attached to a corner of the sample to eliminate charge accumulation during the characterization. The SEM chamber Quanta 200 SEM (FEI, Hillsboro, OR) was pumped to low vacuum in the presence of water vapor ( $\sim 10^{-2}$  Torr). The electron beam accelerating voltage was set to 25 kV with a spot size of 5. The sample was moved to a 10 mm working distance and tilted to 70°. Accelerated electrons, incident on the tilted sample surface,

penetrate the surface, some are backscattered, and the backscattered electrons that escape the crystal interact with the crystal lattice planes. These interactions cause the electrons to form interference patterns called Kikuchi bands, which can be detected on the phosphor screen and which have crystallographic information encoded. Each band corresponds to a specific plane, and the width of band is proportional to the plane's  $d$ -spacing. Using the information in the collected Kikuchi pattern, commercial software (TSL, EDAX, Mahwah, NJ) automatically determines the local orientation associated with the electron beam "spot", a volume which has linear dimensions on the order of tens of nm in each direction.

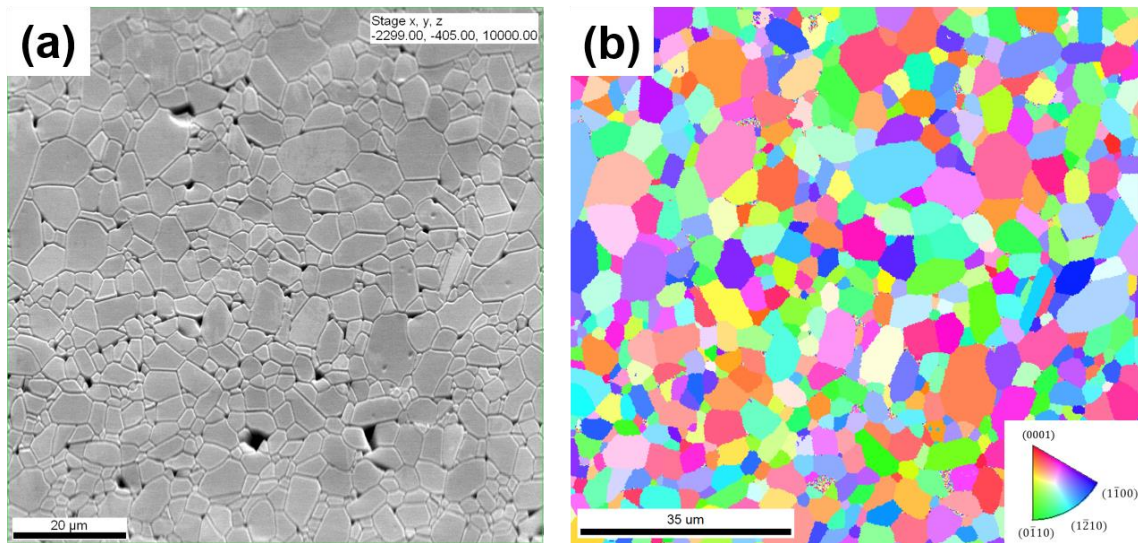


**Figure 3.5.** Examples of EBSD orientation mapping of an  $\text{Fe}_2\text{O}_3$  polycrystal. (a) SEM image. (b) EBSD orientation map of the same area, where the colors are correlated to orientations, defined in the legend.

Representative images of a hematite polycrystal are presented in Fig. 3.5. Image (a) is an SEM image showing the surface of annealed polycrystalline hematite. The granular structure is obvious because the grain boundaries are grooved and display dark contrast. Image (b) is an inverse pole figure map of the orientation normal to the surface (an IPFz map) measured using EBSD. In (b), the color of each pixel represents the local surface

normal orientation, with the color key given as an inset. Any grouping of >50 pixels, with disorientations  $<5^\circ$ , was defined as a grain (using the commercial software). In fact, the image in (b) was processed (cleaned) using two steps of data cleaning. After assigning grain identifications, the first processing step assigned each pixel in a grain the value of that grain's average orientation value. The second processing step removed pixels whose orientations were not determined with reasonable confidence. Diffraction patterns recorded at grain boundaries, non-planar regions, or areas of poor crystalline quality generally result in the software assigning a low confidence index ( $< 0.1$ ) to any solution. Pixels with this low confidence index value ( $< 0.1$ ) were replaced with the most common orientation in the neighboring pixels. After these two steps of image processing, the final grain orientation maps were always similar to that shown in Fig. 3.5(b). In other words, similar grains were easily identified between images from EBSD and other microscopy techniques, and the orientation assigned to specific grains were uniform and of high confidence.

### **3.2.5 X-RAY DIFFRACTION AND REFLECTOMETRY**

Conventional X-ray diffraction (XRD) was used to verify the phase of the photocatalyst and the crystallinity of the Ag particles after the silver-reduction experiment. A Philip X'Pert Pro MRD system was used for the measurements and was operated at 40 kV and 45 mA with a Cu anode generating an X-ray beam of wavelength 0.154 nm (Cu- $K\alpha_1/K\alpha_2$ ). After the diffraction pattern was collected, the results were compared with standard diffraction peak positions and intensities from the International Center of Diffraction Data database.<sup>22</sup>

X-ray reflectometry<sup>23</sup> was used to measure the TiO<sub>2</sub> film thicknesses, which was used to calibrate the PLD growth rate. During the measurement, the angle of the grazing incident X-ray beam is slowly varied. As the reflected angle changes, the reflected beams from the film surface and the film-substrate interface exhibit (constructive or destructive) interference patterns (see Fig. 3.6(a)). Therefore, the detected x-ray intensity changes periodically (oscillates) with the incident angle. The spacing between maxima in the oscillations is directly proportional to the film thickness, as shown in Fig. 3.6(b). The relation between film thickness,  $d$ , and the angular difference two neighboring bumps,  $\Delta\alpha$ , is given by the following equation:

$$d = \frac{\lambda}{2\Delta\alpha} \quad (\text{Eq. 3.1})$$

According to this relationship, there will be fewer oscillations for thinner samples. Note that the maximum incident angle range in the measurement is  $\approx 2^\circ$ ; after  $2^\circ$ , the reflected intensity signal is very low, lower than the noise. Therefore, the thinnest film that the X-ray reflectivity technique can characterize is around 5 nm, which will only show two oscillations in the intensity vs. angle plots. The thicknesses of films thinner than 5 nm were estimated according to the film growth rate established from measurements of thicker films.

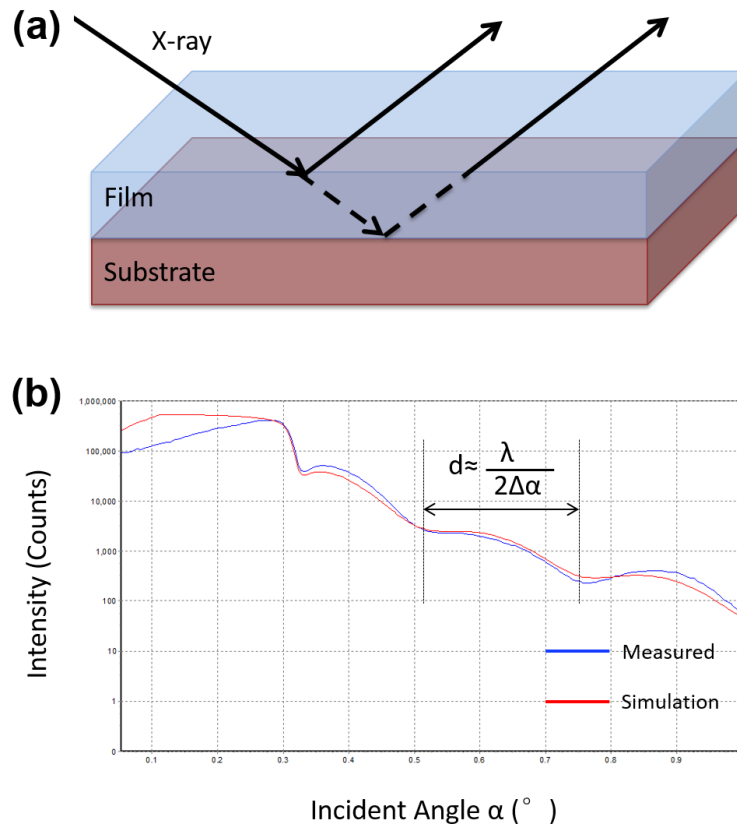


**Figure 3.6.** (a) Illustration of the principle of X-ray reflectivity (b) Example of an X-ray reflectivity curve measured on a TiO<sub>2</sub> film/SrTiO<sub>3</sub> (111) single crystal heterostructure. The spacing between the bumps determines the film thickness. In the simulation, it is assumed that the roughness of film is 8 Å, the roughness of the substrate is 2 Å, and film thickness (d) is 16 nm.

## Reference

1. A. M. Schultz, "The growth and photochemical activity of hematite films on perovskite substrates," (2012).
2. Y. Zhang, A. M. Schultz, P. A. Salvador, and G. S. Rohrer, "Spatially selective visible light photocatalytic activity of  $\text{TiO}_2/\text{BiFeO}_3$  heterostructures," *Journal of Materials Chemistry*, 21[12] 4168-74 (2011).
3. Y. Zhang, A. M. Schultz, L. Li, H. Chien, P. A. Salvador, and G. S. Rohrer, "Combinatorial substrate epitaxy: A high-throughput method for determining phase and orientation relationships and its application to  $\text{BiFeO}_3/\text{TiO}_2$  heterostructures," *Acta Materialia*, 60[19] 6486-93 (2012).
4. N. V. Burbure, P. A. Salvador, and G. S. Rohrer, "Photochemical reactivity of titania films on  $\text{BaTiO}_3$  substrates: origin of spatial selectivity," *Chemistry of Materials*, 22[21] 5823-30 (2010).
5. K. Tanaka, K. Harada, and S. Murata, "Photocatalytic deposition of metal ions onto  $\text{TiO}_2$  powder," *Solar Energy*, 36[2] 159-61 (1986).
6. J. Lowekamp, G. Rohrer, P. Morris Hotsenpiller, J. Bolt, and W. Farneth, "Anisotropic photochemical reactivity of bulk  $\text{TiO}_2$  crystals," *The Journal of Physical Chemistry B*, 102[38] 7323-27 (1998).
7. J. L. Giocondi and G. S. Rohrer, "Structure Sensitivity of Photochemical Oxidation and Reduction Reactions on  $\text{SrTiO}_3$  Surfaces," *Journal of the American Ceramic Society*, 86[7] 1182-89 (2003).
8. A. M. Schultz, Y. Zhang, P. A. Salvador, and G. S. Rohrer, "Effect of Crystal and Domain Orientation on the Visible-Light Photochemical Reduction of Ag on  $\text{BiFeO}_3$ ," *ACS applied materials & interfaces*, 3[5] 1562-67 (2011).
9. R. Li, F. Zhang, D. Wang, J. Yang, M. Li, J. Zhu, X. Zhou, H. Han, and C. Li, "Spatial separation of photogenerated electrons and holes among {010} and {110} crystal facets of  $\text{BiVO}_4$ ," *Nature communications*, 4 1432 (2013).
10. C. Gleitzer, J. Nowotny, and M. Rekas, "Surface and bulk electrical properties of the hematite phase  $\text{Fe}_2\text{O}_3$ ," *Applied Physics A*, 53[4] 310-16 (1991).
11. K. Sorokina and A. Tolstikhina, "Atomic force microscopy modified for studying electric properties of thin films and crystals. Review," *Crystallography Reports*, 49[3] 476-99 (2004).
12. B. Bhushan and A. V. Goldade, "Measurements and analysis of surface potential change during wear of single-crystal silicon (100) at ultralow loads using Kelvin probe microscopy," *Applied surface science*, 157[4] 373-81 (2000).
13. M. Rohwerder and F. Turcu, "High-resolution Kelvin probe microscopy in corrosion science: scanning Kelvin probe force microscopy (SKPFM) versus classical scanning Kelvin probe (SKP)," *Electrochimica Acta*, 53[2] 290-99 (2007).
14. T. Hochwitz, A. K. Henning, C. Levey, C. Daghljan, and J. Slinkman, "Capacitive effects on quantitative dopant profiling with scanned electrostatic force microscopes," *Journal of Vacuum Science & Technology B*, 14[1] 457-62 (1996).
15. A. K. Henning, T. Hochwitz, J. Slinkman, J. Never, S. Hoffmann, P. Kaszuba, and C. Daghljan, "Two - dimensional surface dopant profiling in silicon using

- scanning Kelvin probe microscopy," *Journal of applied physics*, 77[5] 1888-96 (1995).
16. D. Ziegler and A. Stemmer, "Force gradient sensitive detection in lift-mode Kelvin probe force microscopy," *Nanotechnology*, 22[7] 075501 (2011).
  17. H. B. Michaelson, "The work function of the elements and its periodicity," *Journal of Applied Physics*, 48[11] 4729-33 (1977).
  18. M. Nonnenmacher, M. o'Boyle, and H. Wickramasinghe, "Kelvin probe force microscopy," *Applied physics letters*, 58[25] 2921-23 (1991).
  19. S. Mugo and J. Yuan, "Influence of Surface Adsorption on Work Function Measurements on Gold-Platinum Interface Using Scanning Kelvin Probe Microscopy," pp. 012030 in *Journal of Physics: Conference Series*. Vol. 371.
  20. D. Dingley and D. Field, "Electron backscatter diffraction and orientation imaging microscopy," *Materials Science and Technology*, 13[1] 69-78 (1997).
  21. R. A. Schwarzer, D. P. Field, B. L. Adams, M. Kumar, and A. J. Schwartz, "Present state of electron backscatter diffraction and prospective developments," pp. 1-20. in *Electron backscatter diffraction in materials science*. Springer, 2009.
  22. "International Centre for Diffraction Data," *Microscopy Today*, 21[SupplementS1] 8-8 (2013).
  23. E. Chason and T. Mayer, "Thin film and surface characterization by specular X-ray reflectivity," *Critical Reviews in Solid State and Material Sciences*, 22[1] 1-67 (1997).

## Chapter 4 The Orientation Dependence of the Photochemical Activity of $\alpha$ -Fe<sub>2</sub>O<sub>3</sub>

*The orientation dependence of the visible-light stimulated photochemical reduction of aqueous Ag<sup>+</sup> on polycrystalline hematite Fe<sub>2</sub>O<sub>3</sub> was determined by observing the relative amount of reduced Ag<sup>0</sup> on crystals of known surface orientation over all possible orientations. The results show that surfaces oriented within 20 ° of the (1 $\bar{1}$ 02) plane are the most active and surfaces close to the (0001) plane are the least active. A strong correlation is observed between the orientation dependent activity and that of the surface potentials measured by scanning Kelvin-probe force microscopy. Surfaces near the most active (1 $\bar{1}$ 02) plane and least active (0001) plane are respectively at the most positive and the least positive ends of the potential range among all grains. The trends in activity are concluded to arise from a combination of internal fields associated with surface charges and bulk transport effects.*

## 4.1 Introduction

Hematite ( $\alpha\text{-Fe}_2\text{O}_3$ ) is a promising photocatalyst because it absorbs visible light, it is inexpensive, readily available, and chemically stable in aqueous environments, and it doesn't contain environmentally hazardous elements. The band gap energy of 2.2 eV<sup>1</sup> is near the intensity maximum of the solar spectrum. While hematite can readily photooxidize water to generate oxygen, it cannot photoreduce water to produce hydrogen because the conduction band lies 0.21 eV below the reduction level of hydrogen. Nevertheless, hematite has been widely studied as a heterogeneous photocatalyst.<sup>2-8</sup> Despite its promise, the photocatalytic efficiency of hematite is limited by low carrier mobilities and short carrier lifetimes.<sup>2</sup> Because these carrier mobilities are a function of orientation, one expects the photochemical activity of hematite to be anisotropic. Anisotropic activity can also arise from orientation dependent surface features, including chemical terminations, reconstructions, and adsorbates, because these affect the net surface charge and the near surface space charge region. In this paper, we explore the anisotropic photochemical reduction of aqueous  $\text{Ag}^+$  to solid  $\text{Ag}^0$  on hematite surfaces of all orientations under visible light illumination, and demonstrate a strong correlation between the local activity to the local surface potential.

$\alpha\text{-Fe}_2\text{O}_3$  adopts the hexagonal corundum crystal structure (see Fig. 2.4 in §2.5.1) that consists of layers of close-packed oxygen anions ( $\text{O}^{2-}$ ) stacked along the c-axis, with iron cations ( $\text{Fe}^{3+}$ ) filling two-thirds of the octahedral interstitial sites. The anisotropic bonding in the hexagonal structure is reflected in the electronic properties: the measured (n-type) electronic conductivity along the c-axis is four orders of magnitude lower than along directions perpendicular to it.<sup>9,10</sup> As a result, the photocurrent density on orientations perpendicular to the c-axis is 5 to 10 times higher than on the basal faces.<sup>11</sup>

Surface properties are also expected to be strongly anisotropic. Schematic examples of ideal bulk-truncated (0001) and ( $1\bar{1}02$ ) surfaces are given in Fig. 2.5 (see §2.5.1), highlighting the possibility of surfaces having different terminations and charges. While the real surfaces of hematite differ considerably from these ideal versions, their terminations still vary with orientation and they can be charged. Chemisorption of O<sub>2</sub> occurs in one second when the pressure is higher than 10<sup>-2</sup> Torr,<sup>13</sup> which implies oxygen termination is likely in dry air. H<sub>2</sub>O chemisorption occurs above 10<sup>-4</sup> Torr,<sup>14</sup> and the partial pressure of H<sub>2</sub>O in air varies from 0.1 to 33 Torr. Generally, there are three types of adsorbed hydroxyls: single-, double- and triple-coordinated hydroxyls, having charge states of  $-\frac{1}{2}$ , 0,  $+\frac{1}{2}$ , respectively. The amount and type of these hydroxyls vary with the surface orientation and preparation methods,<sup>16-19</sup> and further affect the local surface charge density and activity.<sup>15</sup>

Whatever the origin of this surface charge, it causes the near surface bands to bend in a semiconductor and generates an internal electric field that affects the driving force for photogenerated carriers to move to the surface. Examples of this band bending are shown in Fig. 4.1(a), (b), and (c) for a neutral, positive, and negative surface, respectively. Each of these images are schematics of the relevant electronic energies (see caption for definitions) associated with both a sample (left side) and a nearby metallic tip (right side) to which the sample is grounded. As a result of the band bending in (b) and (c), two things occur for the positively (negatively) charged surface that favor reduction (oxidation) reactions: the population of electrons at the surface of the n-type semiconductor increases (decreases), as does the driving force for the photogenerated electrons (holes) to drift to the surface. Another consequence of band bending is that the contact potential difference between the tip and sample varies with the local surface charge, shown as E<sub>CPD</sub> in Fig. 4.1. Smaller work function materials and more positively charged surfaces will result in a less

positive (more negative) values of  $E_{CPD}$ . Kelvin-Probe Force Microscopy (KFM) is a high throughput scanning probe analytical method that yields a measure of this contact potential difference; such measurements should therefore allow correlations to be made between the local surface potential and reactivity.

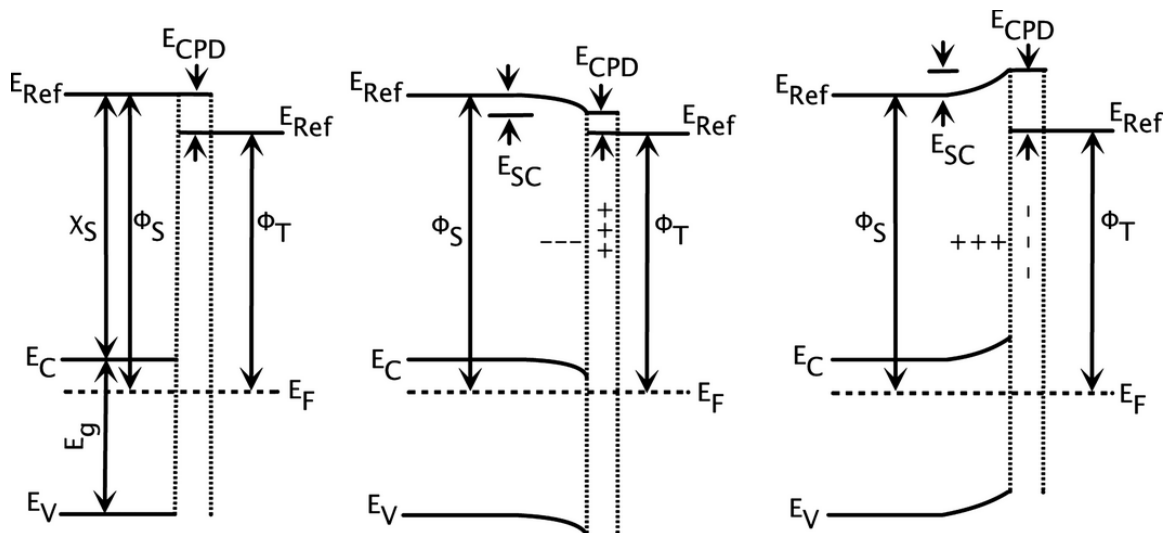


**Figure 4.1.** Schematic electronic energy level diagrams of a sample (left side) and a conductive AFM tip (right side). The Fermi levels ( $E_F$ ) are aligned and the reference level ( $E_{Ref}$ ) discontinuities represent the contact potential difference ( $E_{CPD}$ ).  $E_C$ ,  $E_V$ ,  $E_g$ ,  $\chi_S$ ,  $\Phi_S$ , and  $\Phi_T$ , represent respectively the energies of the conduction band edge, the valence band edge, the bandgap, the sample electron affinity, the sample work function, and the tip work function. The surface is (a) neutral, (b) positive, and (c) negative, with a near surface space charge region ( $E_{SC}$ ) in (b) and (c).

The purpose of this paper is to describe the relative photochemical activity of all possible orientations of  $\alpha\text{-Fe}_2\text{O}_3$  and to correlate this with local surface charge. For the activity, we employ a method used earlier to study the photochemical anisotropy of  $\text{BiVO}_4$ <sup>20</sup> and  $\text{TiO}_2$ .<sup>21</sup> The orientations of many crystals at the surface of an  $\alpha\text{-Fe}_2\text{O}_3$  polycrystal were determined by electron backscatter diffraction (EBSD). Aqueous  $\text{Ag}^+$  was then photochemically reduced to insoluble  $\text{Ag}^0$  on the surface and the locations of reduction were correlated to the crystal orientation. The most active orientations are found to be near the  $(1\bar{1}02)$  orientation, while the most inactive orientations are found close to the basal plane (0001). We then measured the relative surface potential of each

plane using Kelvin-Probe Force Microscopy (KFM). We find that the surface potential is strongly correlated to activity, with (1 $\bar{1}$ 02) having the most positive surface potential and (0001) having the least positive surface potential.

## 4.2 Experimental Procedure

Polycrystalline Fe<sub>2</sub>O<sub>3</sub> was produced and polished by conventional powder processing as described in §3.1.1. After thermal annealing, the orientations of the surface grains were determined using electron backscatter diffraction (EBSD). Patterns were automatically analyzed and indexed using TSL orientation imaging microscopy data collection and analysis software (EDAX, Mahwah, NJ).<sup>22,23</sup> The photochemical reduction of aqueous silver ions to neutral solid silver under blue LED illumination ( $\lambda_{\text{peak}} = 470$  nm, Philips Lumileds, San Jose, CA) was used to mark the locations of the reaction, and was carried out as described previously (see §3.2.1 and §3.2.2).<sup>7,12,20,21,24</sup> After reaction, the samples were rinsed with deionized water. Photodeposited products were confirmed to be crystalline Ag<sup>0</sup> on select samples using a combination of energy dispersive spectroscopy (EDS) in a scanning electron microscope (SEM) and x-ray diffraction (XRD). The surfaces were examined before and after photochemical reaction with optical, atomic force (AFM), and Kelvin force (KFM) microscopy. Conventional AFM images were obtained using an Ntegra or Solver Next AFM (NT-MDT, Moscow, Russia). The local surface potential of active and inactive grains was measured (with the sample covered and not exposed to ambient light sources) using KFM with either NSG03 tips coated by Pt/Ir or 190E-G tips coated by Cr/Pt ( $\Phi \approx 5.1$  eV). A lengthy description of the KFM measurements are given in §2.4 and §3.2.3.

### 4.3 Results

Two characteristic topographic AFM images are shown in Fig. 4.2, which were recorded after a 10 min photochemical reaction. Bright (dark) regions are topographically high (low). The dark interconnected lines arise from the thermally grooved grain boundaries. The relatively uniform intermediate contrast enclosed by the grain boundaries arise from the relatively smooth surfaces of individual grains. The small bright features arise from particles of photodeposited silver, which was confirmed using energy dispersive spectroscopy in a scanning electron microscope and x-ray diffraction.

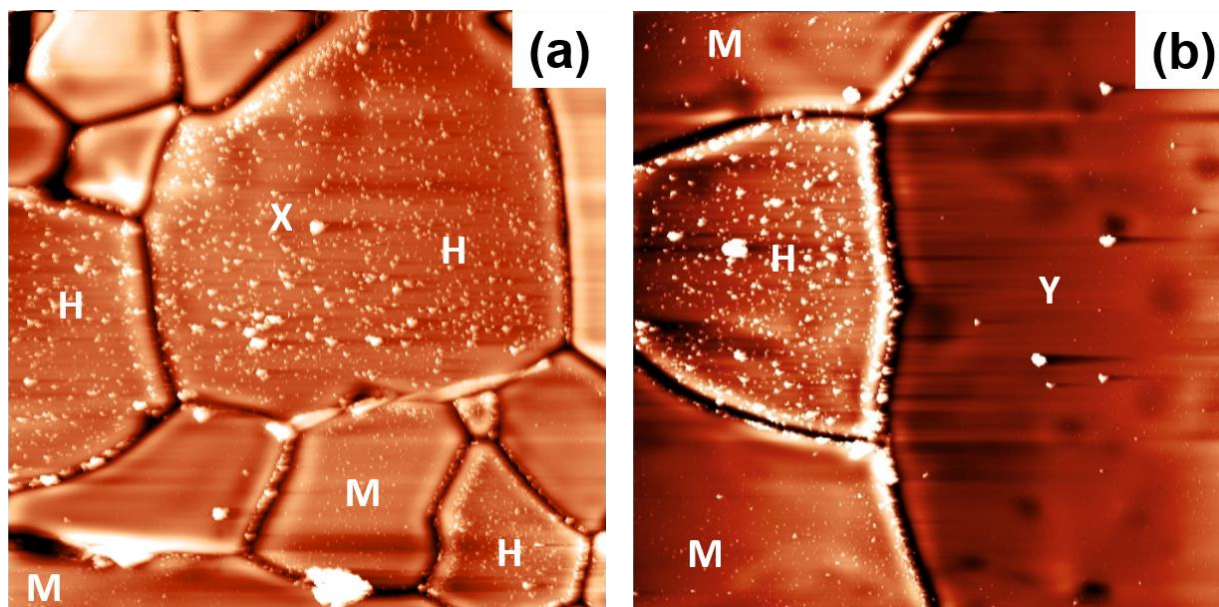


**Figure 4.2.** (a) and (b) are both representative AFM images of  $\alpha$ -Fe<sub>2</sub>O<sub>3</sub> surfaces after silver reduction. Grains classified as highly (moderately) active are marked “H” (“M”), while inactive grains are unmarked. Grains marked with “X” and “Y” identify common grains with Fig. 4.3. The size of each image is 30  $\mu$ m  $\times$  30  $\mu$ m.

It is immediately clear that not all grains have the same relative activity for Ag<sup>+</sup> photoreduction, based simply on the relative number or total amount of bright particles on different grains. We classified the relative activity into three groups: highly (denoted with “H”), moderately

(denoted with “M”), or poorly (grains unmarked in Fig. 4.2) active. The classification was based on the relative area of the grain surface that was covered with bright particles. H (M) grains exhibited Ag<sup>0</sup> particles uniformly spread across their surface covering over 10 % (between 2 to 8 %) of the total grain area. Poorly active grains either had no observable Ag<sup>0</sup> particles, or a few randomly distributed particles covering less than 1% of the grain area. We recorded eleven similar AFM images (each 30 μm × 30 μm) from different regions on the surface after silver photoreduction, and classified their grains in an identical fashion. Overall we characterized 69 grains for activity using AFM images, with 21 (or 30 %), 20 (or 29 %), and 28 (or 41 %) classified as highly, moderately, and poorly active, respectively.

The orientations of the surface grains that were classified for their activity were then determined using EBSD. In the inverse pole figure (IPF) map given in Fig. 4.3, each pixel is colored according to the orientation of the local surface normal (the legend is given as an inset). Regions of constant color correspond to grains of constant average orientation. For reference, the regions shown in Fig. 4.2 (Fig. 4.5) are marked and outlined by white squares (red rectangle) in Fig. 4.3.

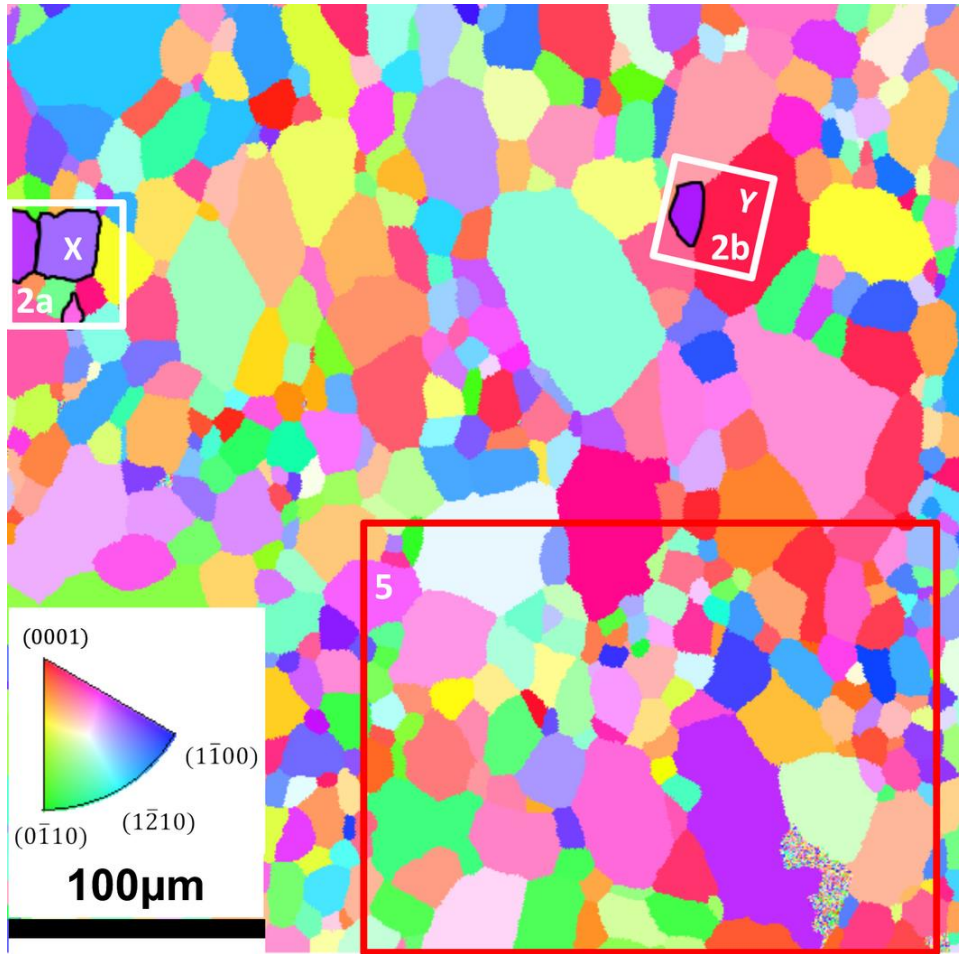


**Figure 4.3.** Inverse pole figure (orientation) maps of the  $\alpha$ -Fe<sub>2</sub>O<sub>3</sub> surface. The color code is given as the standard stereographic triangle of a hexagonal crystal. Grains marked with "X" and "Y" identify common grains with Fig. 4.2. The white (red) boxes indicate the regions shown in Fig. 4.2 (Fig. 4.5). Highly active grains from Fig. 4.2 are outlined by black lines.

The activity of different grains is plotted versus their orientation on a stereographic projection in Fig. 4.4. The symbols correspond to the relative activity of each grain. Most of the 21 highly active grains (red solid triangles) are clustered near the  $(1\bar{1}02)$  orientation. While most of the grains near  $(1\bar{1}02)$  are highly active, not all are. More than half of the poorly active (open circles) grains are within  $40^\circ$  of the  $(0001)$  orientation: 17 of the 28 existing in the angular space of the triangle from  $(0001)$  to  $(0\bar{1}14)$ . Most of the poorly active grains are away from  $(1\bar{1}02)$  orientation, with one outlying poorly (highly) active grain overlapping (outside) the region of

orientation space in which the highly active grains mainly exist. The moderately active grains are spread in orientation space, but they mainly separate the regions of highly and poorly active grains, while having a significant overlap with these other clusters.

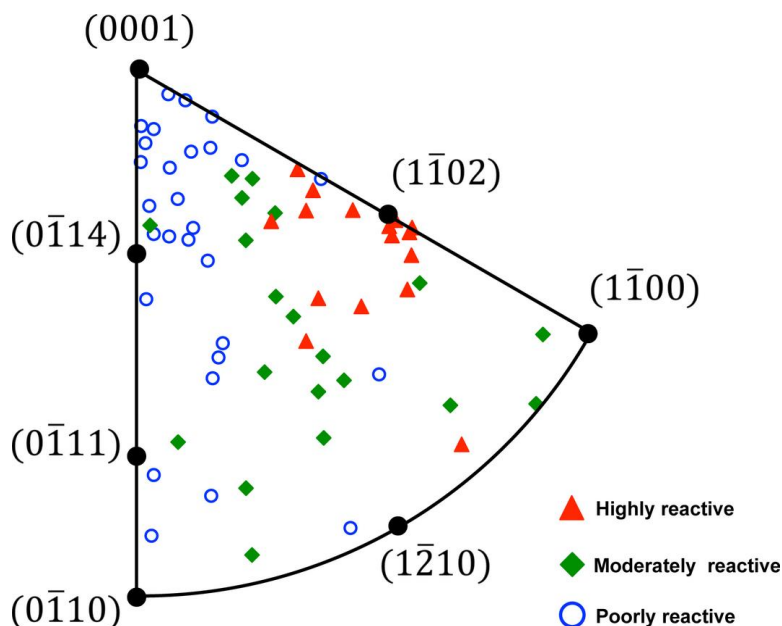


**Figure 4.4.** Orientation dependent activity (as determined from AFM measurements) of 89 grains plotted on the standard stereographic triangle for hexagonal crystals. Each point indicates the activity classification (see legend) and the location in the triangle represents the orientation.

While AFM is a good indicator of the initial activity, owing to its high sensitivity to topographic variations, it is time consuming to generate significantly larger data sets. As such, dark field (DF) optical microscopy (OM) was used to quantify the relative coverage of silver particles on a much larger set of grains spread over a much larger area. Fig. 4.5(a) is a DF-OM image of the  $\text{Fe}_2\text{O}_3$  surface after the photochemical reduction of silver (for 20 mins). In the image, the grain surfaces appear dark, while the grooves at the boundaries and the silver nanoparticles appear bright. The corresponding area is marked by the red rectangle in Fig. 4.3. To improve the contrast in the image and to quantify the activity, the DF-OM images were further analyzed using Photoshop and Matlab. First, the reacted surfaces were converted to greyscale images (0 - 255

levels). Then, pixels with greyscale values more than 6 greater than the average of neighboring pixels, which belong to reactants or grain boundaries, were set to white (level 255). The image after this processing is shown in Fig. 4.5(b). An AFM topography image is shown in Fig. 4.5(c), which was taken from the region outlined with a red rectangle in Fig. 4.5(b). The processed DF-OM from this region is shown in Fig. 4.5(d). Comparing Fig. 4.5(c) and 4.5(d), there is very good correlation between the bright silver particles in AFM and the white pixels (away from the grain boundaries) in the processed DF-OM image. As such, it is reasonable to assign the white pixels in the DF-OM, away from the grain boundaries, as representing silver particles on the hematite surfaces.

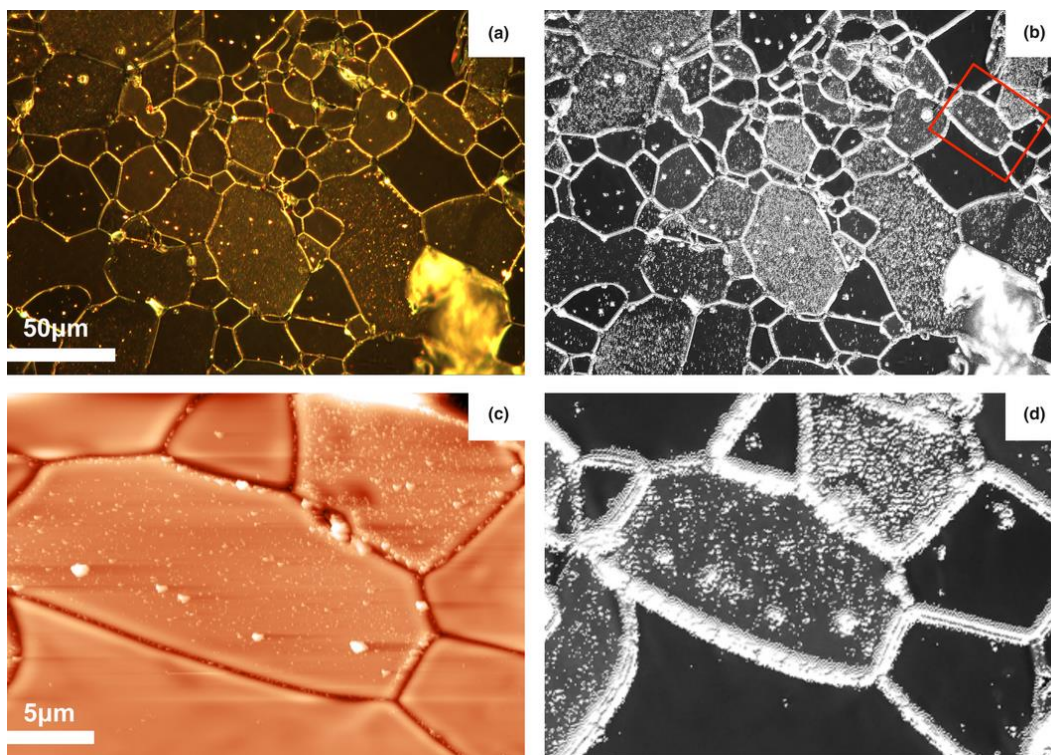


**Figure 4.5.** Dark field optical microscopy images of the  $\alpha\text{-Fe}_2\text{O}_3$  surface (corresponding to the grains in the red rectangle in Fig. 4.3) after the photochemical reduction of Ag. The unprocessed image is given in (a) and the processed image (see text) in (b). The red box in (b) outlines the region from which the AFM topographic image, given in (c), and the magnified processed DF-OM image, given in (d), are taken.

We again classified the relative activity of grains by quantifying the percentage of each grain covered by  $\text{Ag}^0$ , as indicated by the percentage of white pixels on the each grain surface (away from the boundaries) in the processed DF-OM images. 4 DF-OM images were used, taken from regions also characterized with EBSD; the data set contained 547 grains (compared to the 69 used in the AFM dataset). The percentage of white pixels varied from 0 to 46.5 %. Finally the activity was classified as poorly, moderately, and highly active when the silver coverage (white pixel percentage) was 0-3 %, 3-20 %, and more than 20 %, respectively. This resulted in the assignment of 247 (or 45%), 234 (or 43 %), and 66 (or 12 %) for poorly, moderately, and highly active grains, respectively.

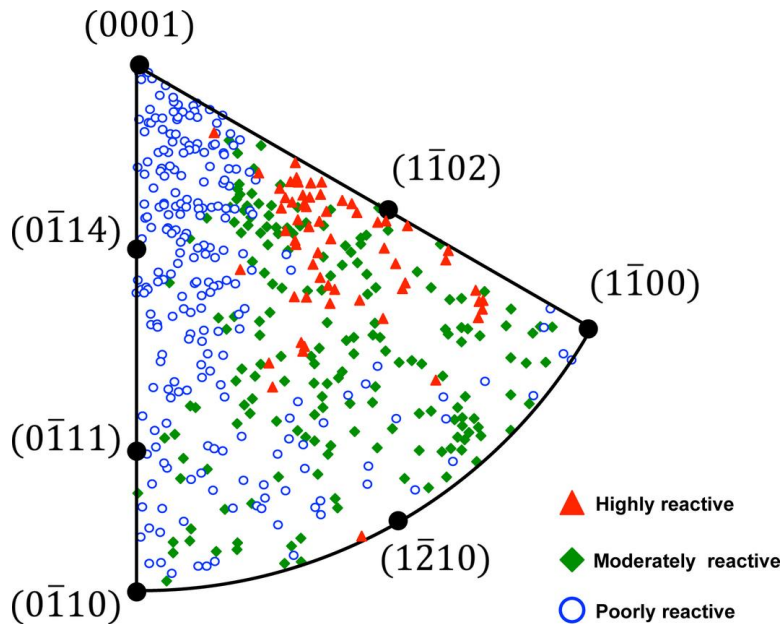


**Figure 4.6.** Orientation dependent activity (as determined from optical microscopy measurements) of 547 grains plotted on the standard stereographic triangle for a hexagonal crystal. Each point indicates the activity classification (see legend) and the location in the triangle represents the orientation.

The relative activity of these 547 grains (based on the DF-OM analysis) is plotted versus their orientation on a stereographic projection in Fig. 4.6. The relative activity distribution shown in Fig. 4.6 is similar to the result from AFM analysis (in Fig. 4.4), and there is a considerable

overlap between the moderately active grains and the other classifications. Still, the highly active grains are clustered around the  $(1\bar{1}02)$  orientation, with a few extra outliers in this larger dataset. Also, almost every grain near the  $(1\bar{1}02)$  orientation is either highly or moderately active. Grains near  $(0001)$  are almost exclusively poorly active; over 90% of the grains within  $30^\circ$  of the  $(0001)$  plane are poorly active (most grains within the angular space of the triangle from  $(0001)$  to  $(0\bar{1}14)$  are poorly active). Grains in the region nearby the triangle edge from  $(0001)$  to  $(0\bar{1}10)$  are generally inactive, with the number of moderately active grains increasing in this region on moving away from the  $(0001)$ . In the remainder of the triangle, the moderately and poorly active grains are intermingled. However, the number of moderately (poorly) active grains increases (decreases) on moving from the region near  $(0\bar{1}10)$  to the region near  $(1\bar{1}00)$ .

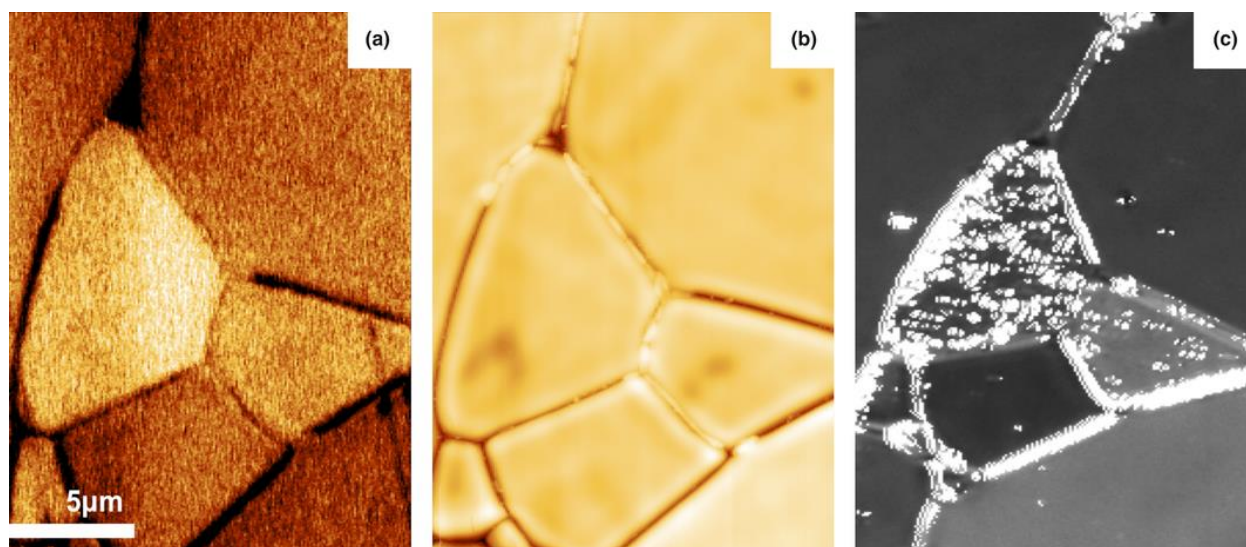


**Figure 4.7.** A representative KFM image (a) and the associated AFM topography image (b), as well as the DF-OM image after reaction (c). The horizontal scale is the same in all images, given in (a). The color range in the KFM image runs from  $-220$  mV (dark) to  $-100$  mV (light), and in the AFM image from  $0$  nm (dark) to  $200$  nm (light).

KFM measurements were used to quantify the surface potentials of the grains investigated with the DF-OM analysis. A representative example of these results is shown in Fig. 4.7. The potential and topographic images recorded from a clean surface are shown in Fig. 4.7(a) and (b),

respectively. The processed DF-OM image from this region, after reaction, is shown in Fig. 4.7(c). Two active grains, covered by silver, and portions of five adjacent poorly active grains are shown in the DF-OM image. The active grains have measured KFM potentials (Fig. 4.7(a)) that are more positive (less negative) than the poorly active ones.

There is a significant variability in the KFM measurements taken from many different images, because the absolute potential value (even from a single grain) varies with the tip shape, the coating type, wear of the probe, as well as instrumental and environmental factors. To analyze the data consistently and to be able to compare different images, we used the following procedure. First we determined the average surface potential of an image, excluding the grain boundaries (for the image in Fig. 4.7(a), this value is -159 mV). Then we determined the average surface potential of each grain in the image (for the image in Fig. 4.7(a), the value of the two active grains are -135 mV and -153 mV). These steps were carried out using the Gwyddion software package. Finally, we determined the difference between the grain's average value and the image's average value (for the image in Fig. 4.7(a), the value of the two active grains are +24 mV and +6 mV). Using this approach, we can compare the relative surface potential of individual grains taken from many different KFM images.

We carried out this procedure on 167 separate grains in 16 separate KFM images, where the scan areas varied from  $30 \times 30 \mu\text{m}^2$  to  $80 \times 80 \mu\text{m}^2$ . The range in relative surface potential values for all grains was from  $-35 \text{ mV}$  to  $+45 \text{ mV}$  (all values being relative to the average potential in the image from which they were taken). The orientation dependence of the measured relative surface potential is given in Fig. 4.8(a). For simplicity of presentation, we segmented the stereographic projection into 39 regions, separated along a  $10^\circ$  grid line for the hexagonal system, and plot the number average relative potential of all grains in the region. There are an average of

$\approx 4$  grains per region, with the lowest having 1 and the highest having 9 grains. Orientations within  $30^\circ$  from the (0001) plane are at one extreme of the potential range, having the least positive relative surface potential. Orientations within  $30^\circ$  of the  $(1\bar{1}02)$  plane are at the opposite potential extreme, having the most positive relative surface potential. Note that the potential values of grains belong to the same region can be very different from each other. Standard deviation of regions containing more than 3 potential data were calculated. However, the standard deviation is not orientation dependent and meaningless, therefore, not presented in this document.

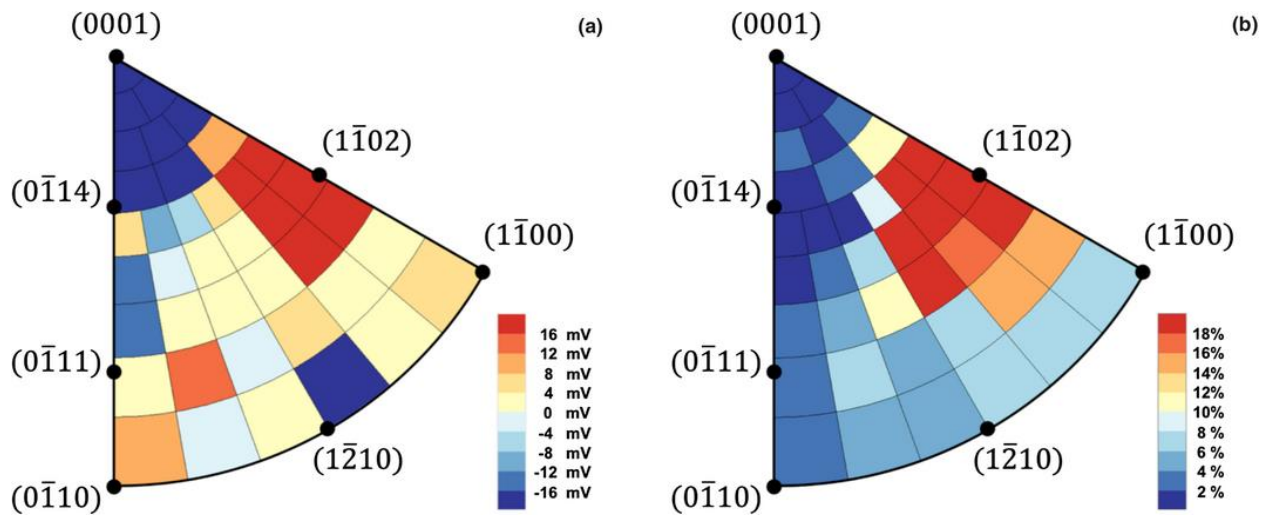


**Figure 4.8.** (a) The average relative potential value (see text) measured by KFM (for 167 grains from 16 different images) plotted versus orientation on a stereographic projection broken into 39 regions. (b) A similar plot of the average activity (see text) measured from DF-OM images (for 547 total grains).

The absolute activity (not using the classification scheme of Fig. 4.6) of the 547 grains from the DF-OM analysis is plotted in Fig. 4.8(b) versus their orientation on the same stereographic projection given in Fig. 4.8(a). The values plotted are the number average percentage of Ag coverage (white pixels) for all grains in the region, according to the color legend in the figure. There is a very strong correlation between the relative activity (absolute coverage of Ag) and the extremes in the measured relative surface potentials: grains close to the (0001) orientation are the most inactive grains and they have the most negative surface potential values, while grains

near  $(1\bar{1}02)$  are the most active grains and they have most positive surface potentials. It should be pointed out that outliers were observed: not all active grains had positive surface potentials (though most did), and not all grains with large positive surface potentials were active (though most were).

A number of experiments were conducted to test the reproducibility of the observations and the sensitivity to the experimental conditions. First, a surface layer thinner than the average grain size was removed by polishing, and the high temperature thermal etching treatment was repeated. When the reduction reaction was also repeated, the same grains were active. Second, KFM images recorded after an extended immersion in water and KFM images recorded after drying at 120 °C were compared: there were no significant differences in the measured relative surface potentials between these experiments. Third, when the silver was removed from the surface after the reaction, the measured relative surface potential was the same as that measured before the reaction. Finally, samples were annealed under different temperatures and using different times. Most often we found the results described above, and we always found a correlation between activity and surface potentials, the primary observation of this work. Also, the  $(0001)$  was always the least active orientation and had the least positive surface potential. However, we did observe that the orientation of the highly active grains with the most positive surface potentials was sometimes found to be within 15 ° of the  $(1\bar{2}10)$  prismatic plane, for a small number of samples. This phenomenon is possibly due to a different surface reconstruction and surface absorption layer for samples processed in different conditions.

## 4.4 Discussion

The results show that the photochemical activity of  $\alpha\text{-Fe}_2\text{O}_3$  for the reduction of aqueous  $\text{Ag}^+$  to solid  $\text{Ag}^0$  is strongly anisotropic, as are the measured KFM surface potentials. Surfaces oriented near (0001) are significantly less active than other orientations, while surfaces oriented near  $(1\bar{1}02)$  are significantly more active than others (for samples annealed at 1100 °C). The measured KFM surface potentials are strongly correlated with the activity: surfaces oriented near (0001) have least positive surface potentials than other orientations, while surfaces oriented near  $(1\bar{1}02)$  have more positive surface potentials than others.

The idealized bulk-truncated surfaces of the  $(1\bar{1}02)$  plane were depicted in Fig. 2.5(b) in §2.5.1. The oxygen terminated surfaces depicted in Fig. 2.5 (b) would be neutral or negatively charged, in contrast to the observations. The  $(1\bar{1}02)$  plane is reported to be usually hydrated and  $\approx 75\%$  of the absorbed water molecules are dissociated at surface.<sup>25,26</sup> The hydrated surfaces are also reported to be positively charged in a  $\text{pH} < 8.5$  environment,<sup>25,27</sup> which is in accordance with the KFM measurements that indicate the surface is positively charged. The hydrated (0001) plane is predominantly terminated by doubly coordinated hydroxyls,<sup>28</sup> which are relatively inert to the protonation–deprotonation reactions, and is reported to be more negatively charged compared to all other prismatic and rhombohedral planes under acidic to neutral conditions.<sup>11,28,29</sup> Our KFM observations are generally consistent with these earlier reports, and the reactivity is well correlated to the measured surface charge.

The anisotropic photochemical properties of oxides can arise from both bulk and surface properties. Past studies focusing on the anisotropic properties of hematite  $\alpha\text{-Fe}_2\text{O}_3$  have focused on bulk property differences between basal (perpendicular to the c-axis) and prismatic planes

(parallel to the c-axis). As noted earlier, photocurrent densities measured for prismatic surfaces are larger than basal surfaces.<sup>11</sup> This was attributed to the greater electronic conductivity parallel to the basal plane, which improved the electron-hole separation and therefore decreases recombination. While the low conductivity (and associated low mobility of carriers) along the [0001] direction of hematite is consistent with the poor activity of its basal plane, these bulk properties alone cannot explain why the  $(1\bar{1}02)$  has the highest activity. The bulk conductivity favors activity on the prismatic faces, which have normals in directions of highest conductivity,<sup>30</sup> not on the  $(1\bar{1}02)$  face.

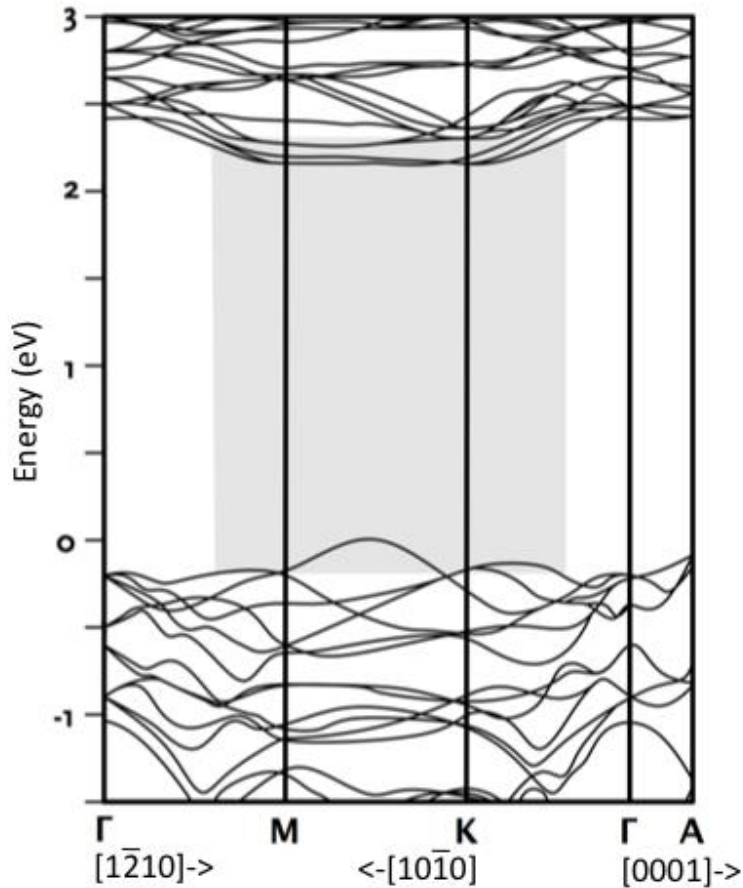


**Figure 4.9.** A calculated<sup>32</sup> electronic band structure for hematite, with the bands rigidly shifted to reflect the experimentally observed band gap. The shaded region represents the momentum states where vertical transitions are possible on absorption of blue light.

It is possible that anisotropic light absorption, relative to the momentum of the photogenerated carriers, affects the overall activity, as proposed for SrTiO<sub>3</sub>.<sup>31</sup> A calculated band dispersion diagram for hematite Fe<sub>2</sub>O<sub>3</sub> is shown in Fig. 4.9.<sup>32</sup> In this energy level diagram,  $\Gamma$  represents the center of the Brillouin zone,  $\Gamma \rightarrow A$  represents states with momentum along the c-axis (parallel [0001]),  $\Gamma \rightarrow M$  represents states with momentum perpendicular to the (1 $\bar{1}$ 02) plane (parallel to a prismatic axis), and  $\Gamma \rightarrow K$  represents states with momentum perpendicular to the (1 $\bar{1}$ 00) orientation, traveling in a direction inclined by 30° to the prismatic axis, along a close packed oxygen direction. This anisotropic absorption behavior further reinforces an expected low activity of (0001) because the direct band gap for electrons traveling perpendicular to this face is 0.3-0.5 eV larger than for electrons traveling toward the prismatic and rhombohedral faces. This would result in fewer photogenerated carriers traveling in these directions, and a resultant lower activity. However, one expects no significant difference in electron populations (based on bandgap absorption) for directions normal to (1 $\bar{2}$ 10), (1 $\bar{1}$ 00), and (1 $\bar{1}$ 02). Again, while the anisotropy of this bulk property supports the poorly active nature of the (0001) basal plane, it cannot explain the higher activity of the (1 $\bar{2}$ 10) plane compared to the prismatic planes.

Reports<sup>33-36</sup> suggest that the increased activity of certain orientations of TiO<sub>2</sub> results from the presence of certain highly active surface planes. The anisotropic activity of SrTiO<sub>3</sub> has been attributed both to the differences in the energies needed to create electron-hole pairs with momentum along different crystallographic directions<sup>31</sup> and to differences in surface polarity.<sup>12</sup> Surface polarity from internal polarization in ferroelectrics has also been shown to be an important factor in local activity.<sup>24,37-39</sup> More recently, it was shown that centrosymmetric ferroelastics can exhibit surface polarizations that directly affect surface photochemical reactions.<sup>40</sup> The correlation observed here for Fe<sub>2</sub>O<sub>3</sub> between the anisotropic surface potential measured with KFM and the

anisotropic activity indicate that surface charges play a significant role in determining the local photochemical activity. A similar effect was reported for ZnO, for which the high photochemical activity of the (110) plane was ascribed to greater upward band bending and higher surface conductance.<sup>41</sup>

Fig. 4.1 depicts the energy band diagram of hematite surfaces with different surface charges, in the dark. Assuming the illumination is low enough such that the photogenerated carrier populations is much lower than the background, these diagrams will be appropriate to describe reaction conditions. Because the conduction band of hematite is 0.21 V vs. NHE,<sup>32</sup> it lies 0.59 eV above the reduction level of silver (0.8 V, not shown in diagram). Therefore, band edge electrons at the surface have significant excess energy towards the the silver-reduction reaction, regardless of that surface charge (or type of band bending). Therefore, the population of photoelectrons at surface controls the silver-reduction activity.

A positively (negatively) charged surface is expected to increase the downward (upward) surface band bending, leading to an increase (decrease) in the electron population in the near surface space-charge region and to an internal electric field that helps photogenerated electrons (holes) drift to the surface. Therefore, a positively charged surface is expected to be more reactive for photoreduction as the population of electrons (native and photogenerated) is larger. The highly active (1 $\bar{1}$ 02) surfaces have the most positive surface charges, while the poorly active (0001) surfaces have the most negative surface charges. The idea that the active grains have a more positive surface potential is supported by the KFM measurements: highly active grains were on average 60 mV more positive than poorly active grains. While the magnitude of this difference is affected by a variety of screening phenomena, and the value should not be interpreted as an absolute difference in surface potential, it can be interpreted as a relative difference in surface

charge. Such modifications of activity based on the surface band bending are analogous to the photochemical reaction on ferroelectrics, where positive domains reduce solution species and negative domains oxidize them. All of this indicates that control of surface charges is an attractive approach to optimizing the activity of photocatalysts.

#### 4.5 Conclusions

Experimental observations indicate that surfaces of  $\alpha$ -Fe<sub>2</sub>O<sub>3</sub> (annealed at 1100 °C) oriented within 30 ° of the (1 $\bar{1}$ 02) plane are far more active than others for the photochemical reduction of aqueous Ag<sup>+</sup> to solid Ag<sup>0</sup>, and surfaces oriented within 30 ° of the (0001) plane are far less active than others. The surface potentials of the highly active (poorly active) grains, measured using scanning Kelvin probe microscopy, are more (less) positive than the surface potentials of the other grains. The anisotropy of the activity can be rationalized considering the relative internal fields arising from surface charges along with the bulk absorption and carrier transport, which work together to make the activity of the (1 $\bar{1}$ 02) plane superior and the activity of the (0001) plane inferior.

## Reference

1. Y. Lin, G. Yuan, S. Sheehan, S. Zhou, and D. Wang, "Hematite-based solar water splitting: challenges and opportunities," *Energy Environ. Sci.*, **4** [12] 4862-69 (2011).
2. K. Sivula, F. le Formal, and M. Grätzel, "Solar Water Splitting: Progress using Hematite ( $\alpha$ - $\text{Fe}_2\text{O}_3$ ) Photoelectrodes," *Chemsuschem*, **4** [4] 432-49 (2011).
3. M. A. Gondal, A. Hameed, Z. H. Yamani, and A. Suwaiyan, "Production of hydrogen and oxygen by water splitting using laser induced photocatalysis over  $\text{Fe}_2\text{O}_3$ ," *Appl. Catal. A*, **268** [1-2] 159-67 (2004).
4. J. Y. Cao, T. Kako, N. Kikugawa, and J. H. Ye, "Photoanodic properties of pulsed-laser-deposited  $\alpha$ - $\text{Fe}_2\text{O}_3$  electrode," *J. Phys. D*, **43** [32] 325101:1-7 (2010).
5. Y. Lin, S. Zhou, S. W. Sheehan, and D. Wang, "Nanonet-based Hematite Heteronanostructures for Efficient Solar Water Splitting," *J. Am. Chem. Soc.*, **133** [8] 2398-401 (2011).
6. J. Luo and P. A. Maggard, "Hydrothermal Synthesis and Photocatalytic Activities of  $\text{SrTiO}_3$ -coated  $\text{Fe}_2\text{O}_3$  and  $\text{BiFeO}_3$ ," *Adv. Mater.*, **18** [4] 514-17 (2006).
7. A. M. Schultz, P. A. Salvador, and G. S. Rohrer, "Enhanced photochemical activity of  $\alpha$ - $\text{Fe}_2\text{O}_3$  films supported on  $\text{SrTiO}_3$  substrates under visible light illumination," *Chem. Comm.*, **48** [14] 2012-14 (2012).
8. Y. Wang, T. Yu, X. Chen, H. Zhang, S. Ouyang, Z. Li, J. Ye, and Z. Zou, "Enhancement of photoelectric conversion properties of  $\text{SrTiO}_3/\alpha$ - $\text{Fe}_2\text{O}_3$  heterojunction photoanode," *J. Phys. D*, **40** [13] 3925-30 (2007).
9. N. Iordanova, M. Dupuis, and K. M. Rosso, "Charge transport in metal oxides: A theoretical study of hematite  $\alpha$ - $\text{Fe}_2\text{O}_3$ ," *J. Chem. Phys.*, **122** [14] 144305:1-10 (2005).
10. D. Benjelloun, J. P. Bonnet, J. P. Doumerc, J. C. Launay, M. Onillon, and P. Hagenmuller, "Anisotropie des proprietes electrique de l'oxyde de fer  $\text{Fe}_2\text{O}_3\alpha$ ," *Mater. Chem. Phys.*, **10** [6] 503-18 (1984).
11. C. M. Eggleston, A. J. A. Shankle, A. J. Moyer, I. Cesar, and M. Grätzel, "Anisotropic photocatalytic properties of hematite," *Aquat. Sci.*, **71** [2] 151-59 (2009).
12. J. L. Giocondi and G. S. Rohrer, "Structure sensitivity of photochemical oxidation and reduction reactions on  $\text{SrTiO}_3$  surfaces," *J. Am. Ceram. Soc.*, **86** [7] 1182-89 (2003).
13. R. L. Kurtz and V. E. Henrich, "Surface electronic structure and chemisorption on corundum transition-metal oxides:  $\alpha$ - $\text{Fe}_2\text{O}_3$ ," *Phys. Rev. B*, **36** [6] 3413-21 (1987).
14. P. Liu, T. Kendelewicz, G. E. Brown Jr., E. J. Nelson, and S. A. Chambers, "Reaction of water vapor with  $\alpha$ - $\text{Al}_2\text{O}_3(0001)$  and  $\alpha$ - $\text{Fe}_2\text{O}_3(0001)$  surfaces: synchrotron X-ray photoemission studies and thermodynamic calculations," *Surf. Sci.*, **417** [1] 53-65 (1998).
15. V. Barrón and J. Torrent, "Surface Hydroxyl Configuration of Various Crystal Faces of hematite and Goethite," *J. Colloid Interf. Sci.*, **177** [2] 407-10 (1996).
16. K. S. Tanwar, J. G. Catalano, S. C. Petitto, S. K. Ghose, P. J. Eng, and T. P. Trainor, "Hydrated  $\alpha$ - $\text{Fe}_2\text{O}_3(1\bar{1}02)$  surface structure: Role of surface preparation," *Surf. Sci.*, **601** [12]: L59-64 (2007).
17. T. P. Trainor, A. M. Chaka, P. J. Eng, M. Newville, G. A. Waychunas, J. G. Catalano, and G. E. Brown Jr., "Structure and reactivity of the hydrated hematite (0001) surface," *Surf. Sci.*, **573** [2] 204-24 (2004).
18. M. A. Henderson, "Insights into the (1 $\times$ 1)-to-(2 $\times$ 1) phase transition of the  $\alpha$ - $\text{Fe}_2\text{O}_3$  (012) surface using EELS, LEED and water TPD," *Surf. Sci.*, **515** [1] 253-62 (2002).

19. J. G. Catalano, P. Fenter, and C. Park, "Water ordering and surface relaxations at the hematite (110)–water interface," *Geochim. Cosmochim. Ac.*, **73** [8] 2242-51 (2009).
20. R. Munprom, P.A. Salvador and G.S. Rohrer, "The orientation dependence of the photochemical reactivity of BiVO<sub>4</sub>," *J. Mater. Chem. A*, **3** [5] 2370-7 (2015).
21. J. B. Lowekamp, G. S. Rohrer, P. A. Morris Hotsenpiller, J. D. Bolt, and W. E. Farneth, "Anisotropic Photochemical Reactivity of Bulk TiO<sub>2</sub> Crystals," *J. Phys. Chem. B*, **102** [38] 7323-27 (1998).
22. D. J. Dingley and D. P. Field. "Electron backscatter diffraction and orientation imaging microscopy," *Mater. Sci. Tech.* **13** [1] 69-78 (1997).
23. R. A. Schwarzer, D. P. Field, B. L. Adams, M. Kumar, and A. J. Schwartz, "Present State of Electron Backscatter Diffraction and Prospective Developments," pp. 1-20 in "Electron Backscatter Diffraction in Materials Science, 2<sup>nd</sup> Edition," Eds. A. J. Schwartz, M. Kumar, B. L. Adams, D. P. Field, Springer (2009).
24. A. M. Schultz, Y. Zhang, P. A. Salvador, and G. S. Rohrer, "Effect of Crystal and Domain Orientation on the Visible-Light Photochemical Reduction of Ag on BiFeO<sub>3</sub>," *ACS Appl. Mater. Inter.*, **3** [5] 1562–67 (2011).
25. J. R. Rustad, E. Wasserman, and A. R. Felmy, "Molecular modeling of the surface charging of hematite: II. Optimal proton distribution and simulation of surface charge versus pH relationships." *Surf. Sci.*, **424** [1] 28-35 (1999).
26. M. A. Henderson, S. A. Joyce, and J. R. Rustad, "Interaction of water with the (1 × 1) and (2 × 1) surfaces of α-Fe<sub>2</sub>O<sub>3</sub> (012)." *Surf. Sci.*, **417** [1] 66-81 (1998).
27. G. A. Parks, and P. D. Bruyn. "THE ZERO POINT OF CHARGE OF OXIDES1." *J. Phys. Chem.*, **66** [6] 967-973 (1962).
28. S. V. Yanina, and K. M. Rosso. "Linked reactivity at mineral-water interfaces through bulk crystal conduction." *Science*, **320** [5873] 218-222 (2008).
29. S. Chatman, P. Zarzycki, and K. M. Rosso. "Surface potentials of (001),(012),(113) hematite (α-Fe<sub>2</sub>O<sub>3</sub>) crystal faces in aqueous solution." *Phys. Chem. Chem. Phys.*, **15** [33] 13911-13921 (2013).
30. S. Kerisit and K. M. Rosso. "Computer simulation of electron transfer at hematite surfaces," *Geochim. Cosmochim. Ac.*, **70** [8] 1888-903 (2006).
31. J. L. Giocondi, P. A. Salvador, and G. S. Rohrer, "The origin of photochemical anisotropy in SrTiO<sub>3</sub>," *Top. Catal.*, **44** [4] 529-33 (2007).
32. M. N. Huda, A. Walsh, Y. Yan, S.-H. Wei, and M. M. Al-Jassim, "Electronic, structural, and magnetic effects of 3d transition metals in hematite," *J. Appl. Phys.*, **107** [12] 123712:1-6 (2010).
33. P. A. Morris Hotsenpiller, J. D. Bolt, W. E. Farneth, J. B. Lowekamp, and G. S. Rohrer, "Orientation dependence of photochemical reactions on TiO<sub>2</sub> surfaces," *J. Phys. Chem. B*, **102** [17] 3216-26 (1998).
34. A. Imanishi, T. Okamura, N. Ohashi, R. Nakamura, and Y. Nakato, "Mechanism of Water Photooxidation Reaction at Atomically Flat TiO<sub>2</sub> (Rutile) (110) and (100) Surfaces: Dependence on Solution pH," *J. Am. Chem. Soc.*, **129** [37] 11569–78 (2007).
35. T. Ohno, K. Sarukawa, and M. Matsumura, "Crystal faces of rutile and anatase TiO<sub>2</sub> particles and their roles in photocatalytic reactions," *New J. Chem.*, **26** [9] 1167-70 (2002).
36. S. Liu, J. Yu, and M. Jaroniec, "Tunable Photocatalytic Selectivity of Hollow TiO<sub>2</sub> Microspheres Composed of Anatase Polyhedra with Exposed {001} Facets," *J. Am. Chem. Soc.*, **132** [34] 11914-6 (2010).

37. A. Bhardwaj, N. V. Burbure, A. Gamalski, and G. S. Rohrer, "Composition Dependence of the Photochemical reduction of Ag by  $Ba_{1-x}Sr_xTiO_3$ ," *Chem. Mater.*, **22** [11] 3527-34 (2010).
38. J. L. Giocondi and G. S. Rohrer, "The influence of the dipolar field effect on the photochemical reactivity of  $Sr_2Nb_2O_7$  and  $BaTiO_3$  microcrystals," *Top. Catal.*, **49** [1-2] 18-23 (2008).
39. Y. Inoue, K. Sato, K. Sato, and H. Miyama, "Photoassisted water decomposition by ferroelectric lead zirconate titanate ceramics with anomalous photovoltaic effects," *J. Phys. Chem.*, **90** [13] 2809-10 (1986).
40. R. Munprom, P. A. Salvador, and G. S. Rohrer, "Polar Domains at the Surface of Centrosymmetric  $BiVO_4$ ," *Chem. Mater.* **26** [9] 2774-76 (2014).
41. G. Li, Z. Yi, H. Wang, C. Jia, and W. Zhang, "Factors impacted on anisotropic photocatalytic oxidization activity of ZnO: Surface band bending, surface free energy and surface conductance," *Appl. Catal. B*, **158-9**, 280-5 (2014).

# Chapter 5 Controlling the Relative Areas of Photocathodic and Photoanodic Terraces on the SrTiO<sub>3</sub> (111) Surface

*SrTiO<sub>3</sub> (111) surfaces have been heated in air at 1250 °C, either alone or with reservoirs of TiO<sub>2</sub> and SrTiO<sub>3</sub> powders. The surface structure and properties were measured by atomic force microscopy, scanning Kelvin probe microscopy, x-ray photoelectron spectroscopy (XPS), and photochemical marker reactions that leave solid products on the surface at the site of the photochemical reaction. All of the surfaces are made up of atomically flat terraces of two distinguishable types. One terrace has a relatively higher surface potential and promotes the photochemical reduction of Ag<sup>+</sup>. The other terrace has a relatively lower positive potential and promotes the photochemical oxidation of Pb<sup>2+</sup>. XPS measurements show that the concentration of titanium at the surface increases with the fraction of TiO<sub>2</sub> in the powder reservoir during annealing, and marker reactions show the fraction of terraces that promote oxidation increases with the titanium content. The fractional area of terraces that promote oxidation was controlled between 45 % and 86 % of the total area*

## 5.1 Introduction

Photochemical reactions on semiconductor surfaces have been studied for decades with the goal of developing improved catalysts that can be used to separate hydrogen from water or degrade pollutants.<sup>1, 2, 3, 4, 5</sup> However, photocatalytic water-splitting is not yet a commercial technology because of its low efficiency when driven by visible light. Semiconducting oxides are one of the most promising types of photocatalysts because of their relative stability in sunlight and water. For an individual photocatalyst carrying out both photochemical half-reactions, the overall efficiency is limited by the slower of the two half-reactions.<sup>6</sup> Thus, controlling the relative areas of the surface that promote oxidation and reduction is a key to optimizing the overall efficiency of a photocatalyst. Local surface charges can cause an oxide surface to favor either oxidation or reduction. For example, at the surface of ferroelectric oxides, positively charged domains favor reduction and negatively charged domains favor oxidation.<sup>7, 8, 9</sup> The separation of electrons and holes to photocathodic and photoanodic sites has also been suggested to increase overall photochemical efficiency by reducing charge carrier recombination and the back reaction.<sup>10, 11, 12</sup> Therefore, it is of great interest to develop new methods to control local surface charges that impact local photochemical reactivity.

Here we focus on controlling surface charges on strontium titanate ( $\text{SrTiO}_3$ ), a well-known photocatalyst that can split water under UV-light.<sup>13, 14</sup> We choose to focus on single crystal (111) surfaces because the bulk truncated (111) surface is polar. Polar surface terminations are created when an ionic crystal is cleaved and the two new surfaces each have a net (and opposite) charge.  $\text{SrTiO}_3$  crystallizes in the cubic perovskite structure ( $a = 3.905 \text{ \AA}$ ), as shown in Fig. 5.1(a). The unreconstructed  $\text{SrTiO}_3$  (111) surface is polar because it can be terminated either by  $\text{Ti}^{4+}$  or  $\text{SrO}_3^{4-}$ , as shown in the side view depiction in Fig. 1(b). The spacing between two atomic layers of

different chemical compositions is an odd multiple of  $N$  ( $N = \sqrt{3}/6a = 1.12 \text{ \AA}$ ). For example, the step height between the  $\text{Ti}^{4+}$  and  $\text{SrO}_3^{4-}$  layers in Fig. 5.1(b) is  $3N$ . While this “bulk truncation” model is a reasonable starting point, it must be recognized that for samples exposed to air, submerged in aqueous solutions, or annealed at high temperature where diffusion is activated, the real  $\text{SrTiO}_3$  (111) surface is likely to be reconstructed in some way,<sup>15</sup> and will definitely have a layer of adsorbates<sup>16, 17</sup> and an associated space charge region.

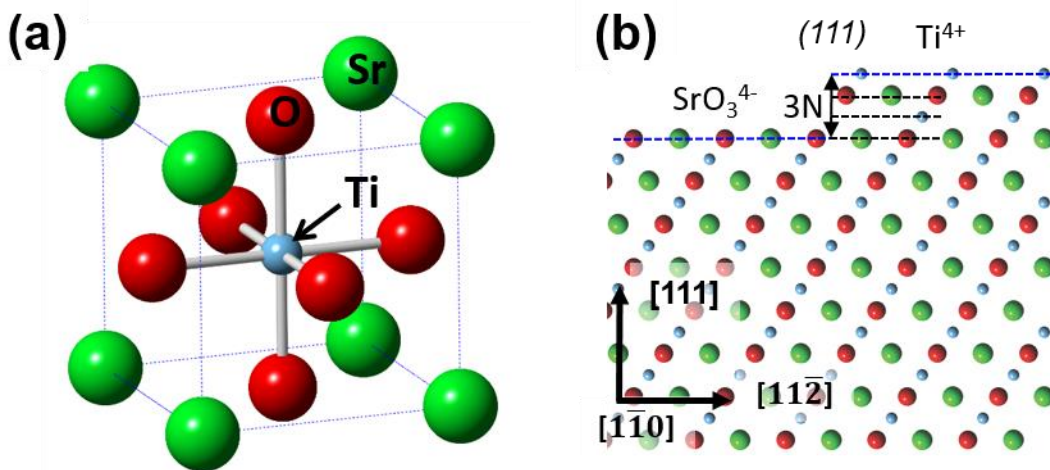


**Figure 5.1.** (a) The unit cell of perovskite  $\text{SrTiO}_3$ . (b) Schematic of  $\text{SrTiO}_3$  viewed along  $[\bar{1}\bar{1}0]$ . The dashed lines indicate the (111) planes. Along the  $[111]$  direction,  $\text{SrTiO}_3$  is comprised of alternating  $\text{SrO}_3^{4-}$  and  $\text{Ti}^{4+}$  atomic layers separated by  $N = 1.12 \text{ \AA}$ .

It has already been shown that distinct terraces on the  $\text{SrTiO}_3$  (111) surface separately promote reduction and oxidation in photochemical reactions.<sup>18</sup> In other words, one terrace is photocathodic and the other is photoanodic. However, the compositions and potentials of these different surfaces have not yet been measured. According to the results of semi-empirical Hartree-Fock method calculations, titanium rich surfaces have a greater work function than strontium rich surfaces by 0.3 eV to 0.8 eV, depending on the surface composition.<sup>19</sup> Experimental measurements yield smaller differences.<sup>20</sup> In fact, the Ti-rich surface can have a work function that is sometimes

greater than and sometimes less than the Sr-rich surface, depending on the way the surface is prepared.<sup>20</sup> In this work, Kelvin probe force microscopy (KFM) is used to measure the difference in the overall surface potential of the terraces with different reactivities. It will be shown that the two terraces have distinct contrast in KFM images, which makes them interact differently with electrons and holes, yielding different reactivities.

In the early work that identified photoanodic and photocathodic terraces on the SrTiO<sub>3</sub> (111) surface, it was not clear what determined the relative areas of the two terraces.<sup>18, 21</sup> Since then, others have produced surfaces with a uniform Ti-rich termination by thermal annealing in ultra high vacuum<sup>22</sup> or by etching with a buffered hydrogen fluoride solution.<sup>23, 24, 25</sup> The goal of creating uniform terminations was to promote improved thin film crystal growth. However, from a photochemical point of view, one would like to tailor the ratio of the two types of terminations to maximize the overall reaction rates by equalizing the net reduction and oxidation rates. In general, the area specific reaction rate (rate per surface area) is not expected to be the same for reactions on different terraces. However, the overall reaction rate could be optimized by creating surfaces with relative areas of the two terraces that are the inverse of their relative area specific reduction and oxidation rates. We describe a novel method to control the relative area of Ti-rich or Sr-rich surfaces, which is generally applicable to their use as photocatalysts and as substrates in thin film growth.

This chapter has two main purposes. The first is to expand what we know about the surface potential and chemical composition of the two different terraces on the SrTiO<sub>3</sub> (111) surface. The relative surface potentials will be measured by Kelvin probe force microscopy (KFM) and correlated to the relative reactivities measured by photochemical marker reactions and to the step heights between the terraces measured by atomic force microscopy (AFM). Furthermore, by

comparing X-ray photoelectron spectra (XPS) of surfaces with different measured potentials and reactivity, we can determine how the reactivity is correlated to the relative concentrations of Sr and Ti on the surface. The second purpose is to show that we can control the fractions of the surface that promote reduction and oxidation. We use a novel method that involves a high temperature anneal in the presence of reservoirs of  $\text{TiO}_2$  and  $\text{SrTiO}_3$  powder mixtures. By increasing the amount of  $\text{TiO}_2$  in the powder reservoir, we increase (or decrease) the amount of Ti (or Sr) on the surface. We show here that, by controlling the termination and surface potential distribution, we also control the photochemical properties of the surface, and that these properties are stable with time.

## 5.2 Experimental Procedure

Chemical-mechanical polished  $\text{SrTiO}_3$  (111) single crystals (MTI company, (111)  $\pm 0.5^\circ$ , roughness  $< 5 \text{ \AA}$ ) were sonicated in a methanol bath for 10 min and then placed in a covered rectangular alumina combustion boat and annealed in a muffle furnace at  $1250 \text{ }^\circ\text{C}$  for 10 h (ramp rates were  $5 \text{ }^\circ\text{C}/\text{min}$ ). After annealing, atomically flat terraces,  $0.5$  to  $3 \text{ }\mu\text{m}$  wide, were observed by AFM (Solver-Next, NT-MDT, Russia). A set of similar experiments was carried out to test the sensitivity of the surface structure to the annealing environment. In these experiments, the  $\text{SrTiO}_3$  (111) crystal was put at the center of the same combustion boat and then surrounded by reservoirs of  $\text{TiO}_2$  and  $\text{SrTiO}_3$  powder mixtures with different compositions. The combustion boat was then covered and heated with the schedule described above. All samples were annealed during September to November. The relative humidity in Pittsburgh ranges from  $52 \%$  to  $60 \%$ ,

Photochemically generated solid Ag and Pb-containing reaction products were used to mark the locations of the reduction and oxidation reactions, respectively.<sup>18, 26, 27, 28, 29, 30</sup> A 300 W mercury lamp (Newport, Irvine, CA) was used for the reaction. The exposure time was 8 seconds for Ag<sup>+</sup> reduction and 30 seconds for Pb<sup>2+</sup> oxidation.

Three scanning probe techniques were used to characterize the surface before and after the photochemical reactions. KFM was used to record the local surface potential of each terrace. A silicon AFM probe with a TiN (FMG01/TiN, NT-MDT) or PtCr (190E-G, budget sensor) conductive coating was used for the surface potential measurement. High-precision AFM images were used to measure the step height between neighboring terraces. For high-precision AFM, the noise level of the height measurement is typically 0.3 Å, making it possible to resolve vertical heights as small as 1 Å. It has been shown that, on the SrTiO<sub>3</sub> (111) surface, all terraces are separated by integer multiples of 1.12 Å, regardless of the type of reconstruction.<sup>18, 27</sup> The surface topography of the same area before and after the photochemical reaction was mapped by AFM operated in tapping mode. The Gwyddion software package<sup>31</sup> was used to extract height profiles, potential profiles, and to quantify the surface coverage of photochemical reaction product.

XPS spectra measured using Al K<sub>α</sub> (1486.6 eV) irradiation (PSP Vacuum Tech, UK) were recorded on annealed SrTiO<sub>3</sub> (111) surfaces. To quantitatively analyze the surface chemical composition, high-resolution XPS spectra were taken for Sr 3d, Ti 2p, and O 1s peaks and then analyzed using CasaXPS software.<sup>32</sup> The Spectra shown here were acquired with 0.07 eV energy step at 55° off-normal emission. So that the spectra are as representative as possible of the surface used for photochemistry, the crystals were loaded into the vacuum system and analyzed with no further treatment.

### 5.3 Results

The surface of the SrTiO<sub>3</sub> (111) single crystal substrate after annealing at 1250 °C in air (in the absence of a powder reservoir) is shown in Fig. 5.2(a). The terraces formed on the substrate are obvious. The roughness (root-mean-square average of the height profile) of each terrace is less than 1 Å, indicating that they are atomically flat. Fig. 5.2(b) shows the surface potential image of the same area. When compared to the surface topography, it becomes clear that there are two types of terraces with distinct surface potentials on the SrTiO<sub>3</sub> (111) surface. The measured surface potential from KFM (here measured using a TiN coated probe) is affected by the local work function and surface charge. The two types of terraces have KFM potentials that differ by approximately 7 to 15 mV. The high-precision AFM height profile and the surface potential profile of the lines drawn in Fig. 5.2(a) and (b) are plotted as solid and dashed lines, respectively, in Fig. 5.2(c). The line crosses four atomically flat terraces. From left to right, the first and second terraces (third and fourth terraces) both have more positive (negative) surface potentials, 0.165 V and 0.164 V (0.156 V and 0.157 V), respectively, and they are separated by 6.96 Å  $\approx$  6N (4.49 Å  $\approx$  4N). As noted before, terraces separated by step heights that are an even multiple of N (N = 1.12 Å) should have the same chemical termination. From the second to third terrace, the chemical termination switches because they are separated by a step of a height that is an odd multiple of N (10.09 Å  $\approx$  9N); their surface potential value also changes to a lower value at this transition.

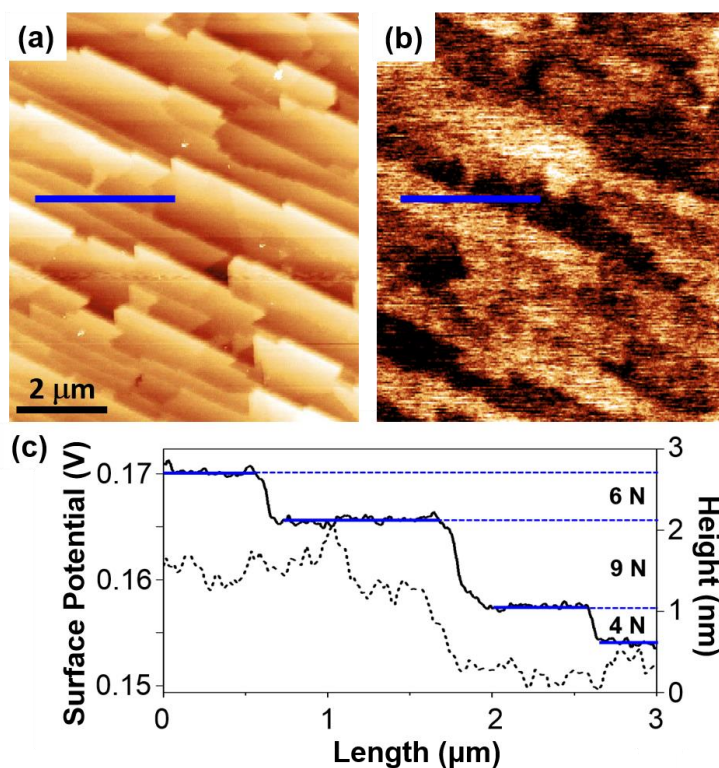


**Figure 5.2.** (a) Surface topography AFM image and (b) surface potential image recorded of the same area. Both images are  $8 \mu\text{m} \times 9.5 \mu\text{m}$ . The same locations are marked by blue lines in the images. The color range from dark-to-light is: (a) 0 to 3 nm, (b) 0.115 to 0.175 V. In (c), the black solid line is the height cross-section at the position of the blue line and the dashed line is potential profile at the same position.

After the sample was immersed in a silver nitrate (lead acetate) solution and illuminated, new contrast appeared on the surface, corresponding to reduced metallic silver (Pb-containing deposits), as shown in Fig. 5.3(a) (Fig. 5.3(b)). The blue line marks the same location as in Fig. 5.2. The fraction of the surface covered by the reaction product on specific terraces is represented in Fig 5.3(c). These two types of terraces behave quite differently for the silver-reduction reaction. Generally, the set of terraces that have a more positive surface potential also have white contrast in Fig. 5.3(a). On such terraces, more than 80 % of the terrace is covered by Ag after the reaction. Therefore, these terraces are strongly photocathodic. The other terraces, that have more negative potential values, have less than 3 % surface coverage.

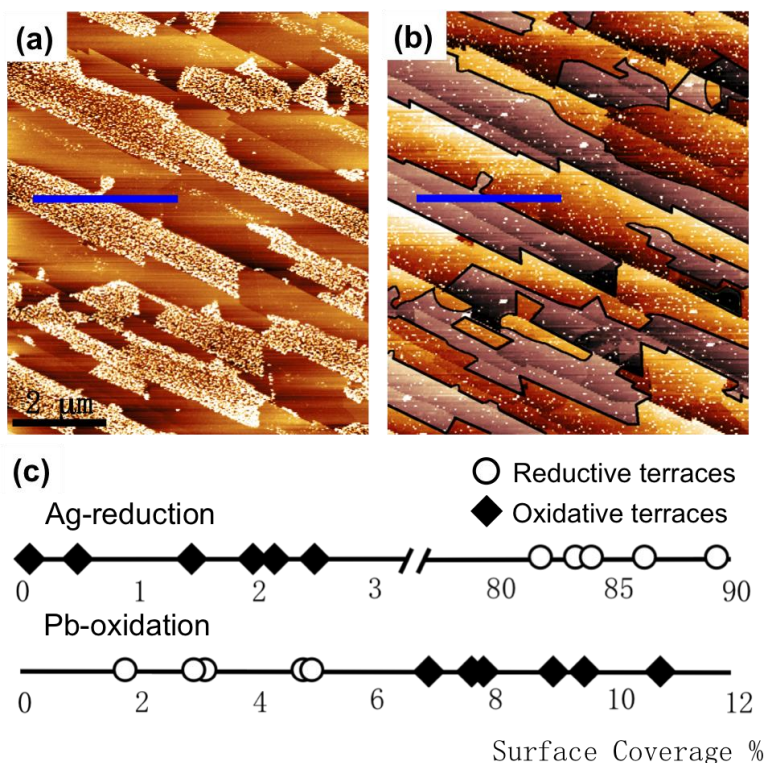


**Figure 5.3.** Topographic AFM images of the same area shown in Fig. 5.2, (a) after silver photoreduction and (b) lead photooxidation. For comparison, Fig. 5.3(b) is segmented using two color saturations. The high color saturation parts include terraces unreactive for photoreduction, and the other parts include terraces reactive for photoreduction. The blue line marks the same position shown in Fig 5.2. Vertical heights are indicated by the color range which is, from dark-to-light: (a) 0 – 10 nm and (b) 0 – 4 nm. In (c), the fractional surface coverage of Ag and Pb-containing particles on terraces from the low and high saturation parts in (b) are plotted as black diamonds and hollow circles, respectively.

When the same crystal was used to photooxidize  $\text{Pb}^{2+}$ , the reaction product appears as white dots as shown in Fig. 3(b). Lead oxidation is a more complex reaction compared to silver reduction. The reaction involves oxygen and the reaction rate is affected by the pH value of the solution.<sup>33, 34</sup> The image shows particles on all terraces, but different terraces have noticeably different densities of particles. In Fig. 3(b), the different terraces have been segmented into two types, indicated by different color saturations. The high color saturation areas only include the set of terraces that are unreactive for the photoreduction of silver (from Fig. 3(a)). The low color saturation areas include the other terraces (the photocathodic terraces reactive for Ag reduction).

The terraces with high color (low color) saturation have  $> 6\%$  ( $< 6\%$ ) of the surface covered by Pb-containing particles, which means that high color (low color) saturation terraces are more (less) reactive for photooxidation reactions.

The results in Fig. 5.3 show that complementary photochemical reactions occur preferentially on distinct terraces on the SrTiO<sub>3</sub> (111) surface. One set of terraces is reactive for the photoreduction of silver and is less reactive for the photooxidation of lead; these terraces are referred to here as photocathodic. The other set of terraces is more reactive for photooxidation and is nearly unreactive for the photoreduction of silver; these terraces are referred to here as photoanodic. Moreover, when correlated with Fig. 5.2(b), photocathodic terraces have a relatively higher surface potential, while photoanodic terraces have a relatively lower surface potential.

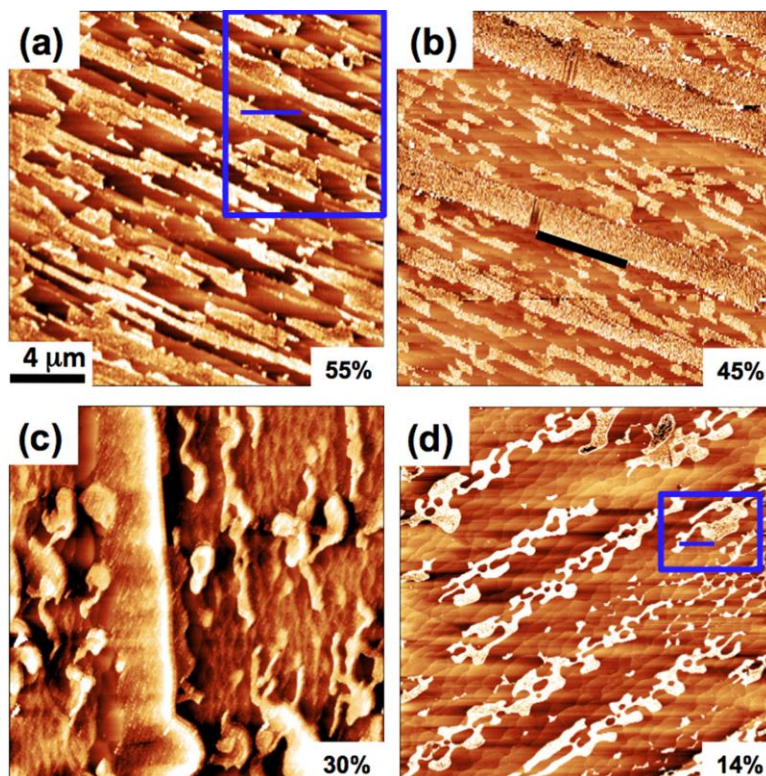


**Figure 5.4.** Topographic AFM images of samples annealed without (a) and with (b-d) different  $\text{TiO}_2/\text{SrTiO}_3$  powder mixtures after the photochemical reduction of silver. Heated with (a) no powder, (b) 31.4 wt % Ti, (c) 36.4 wt % Ti, and (d) 60.0 wt % Ti. All images are  $20\ \mu\text{m} \times 20\ \mu\text{m}$  laterally and the dark-to-light vertical scales are all 0 – 10 nm. The blue boxes and blue lines in (a) (and (d)) indicate the areas from which the high-precision AFM images presented in Fig. 5.2 (Fig. 5.6) were recorded. The black line in (b) marks the same location that is marked in Fig. 5.5 (b) and Fig. 5.7. The fractional coverage of photocathodic terraces in each image is marked in the lower right corner of each image.

Three more pieces of  $\text{SrTiO}_3$  (111) crystals were annealed in the same combustion boat, but with 2 g of  $\text{TiO}_2/\text{SrTiO}_3$  powder mixtures surrounding (but not in contact with) the crystal. The topographic AFM images in Fig. 5.4 compare the ability of surfaces to photochemically reduce silver when they were annealed with (a) no excess powder, (b) 31.4 wt % Ti powder ( $\text{TiO}_2:\text{SrTiO}_3 = 3:7$ ), (c) 36.4 wt % Ti powder ( $\text{TiO}_2:\text{SrTiO}_3=1:1$ ), and (d) 60 wt % Ti powder (pure  $\text{TiO}_2$ ). Each sample was exposed to light for the same amount of time in a solution with the same concentration of silver. The area shown in Fig. 4(a) contains the area already shown in Fig. 5.2 and Fig. 5.3

(enclosed by the blue box). For this control sample, the photocathodic terraces, covered by silver, make up about 55 % of the area. An AFM image of the sample annealed in a  $\text{TiO}_2/\text{SrTiO}_3$  powder mixture with a Ti concentration 31.4 wt % is shown in Fig. 5.4(b). About 45 % of the area is covered by silver particles after silver-reduction. An AFM image of the sample annealed in a  $\text{TiO}_2/\text{SrTiO}_3$  powder mixture with 36.4 wt % Ti is shown in Fig 5.4(c). For this sample, about 30 % of the area is covered by silver particles after silver-reduction. An AFM image of the sample annealed with 60.0 wt % Ti (i.e., pure  $\text{TiO}_2$  powder) is shown in Fig. 5.4(d). For this sample, only 14% of the surface is reactive for silver reduction.

Note that, as the excess Ti concentration in the powder increases, the shape of the terraces also changes from straight edges to curved edges. A clearer view of the changes in terrace shape is observable in Fig. 5.5, showing AFM images of the same areas, but without the reaction product. The topography of the sample annealed with pure  $\text{TiO}_2$  powder (Ti concentration 60.0%) is shown in Fig. 5.5(d). This is a majority photoanodic surface. For samples shown in Fig. 5.5(a) and (b), most terraces have straight edges. The samples shown in Fig. 5.5(c) and 5.5 (d) have terraces with wavy or curved edges.

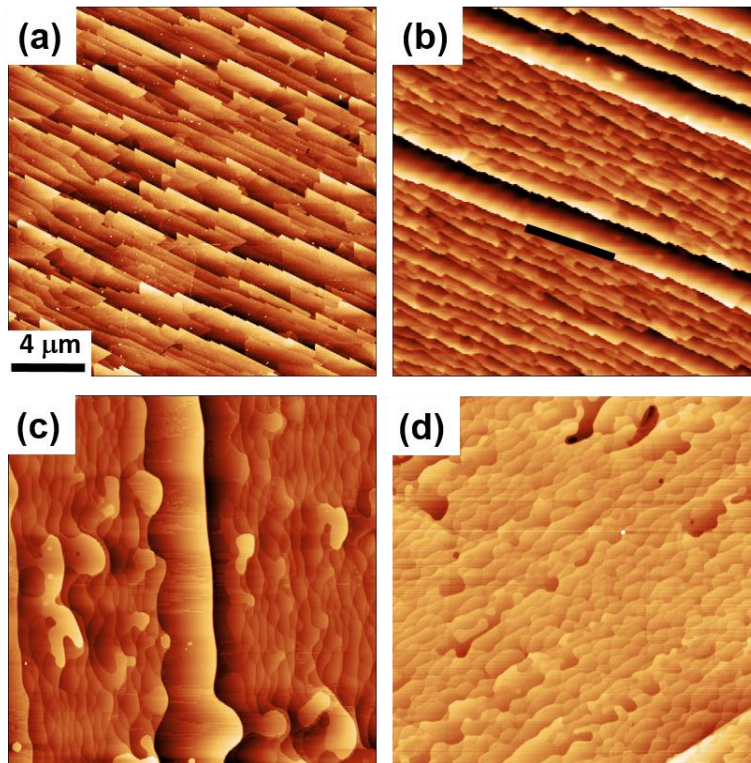


**Figure 5.5.** AFM topography images of the surface before any reactions (a) Sample annealed in air. (b)-(d) Samples were annealed with a powder reservoir. Samples shown in (b) and (c) were annealed with SrTiO<sub>3</sub>/TiO<sub>2</sub> powder mixtures. The Ti concentrations of the powders were 31.4 wt% and 36.4 wt%, respectively. The sample in (d) was annealed with pure TiO<sub>2</sub> powder (Ti concentration is 60.0 wt%). Each image has a 20 μm × 20 μm field of view. Vertical scales for all images are 0 – 4 nm. The black line in (b) marks the same location in Fig 4(b) and Fig. 5.7.

To exclude the possibility that a new phase is formed on the surface of the crystals annealed with excess powder, step height and KFM measurement were repeated on the sample annealed with pure TiO<sub>2</sub> powder. The high-precision topographic AFM image shown in Fig. 5.6(a) was recorded in the area denoted by the blue box in Fig. 5.4(d) (but on the clean surface). A topographic AFM image of the same location after the photoreduction of silver is shown in Fig. 5.6(b). A KFM image (mapped with a Pt/Cr coated probe) of the clean surface, in the same area that is shown in Fig. 5.4(d), is shown in Fig. 5.6(c). From the KFM image, we can clearly see that, similar to the observations from the sample annealed without powder, there are still two distinct contrast levels with a potential difference of 7 to 15 mV. Note that the absolute value of the surface potential

changed from the 155 to 175 mV range (Fig. 5.2(c)) to the -5 to 15 mV range (Fig. 5.6(d)); this is because the AFM probe was coated with a different metal with a different work function. After comparing the pattern of silver reduced on the surface in Fig. 5.4(d) with the potential contrast in Fig. 5.6(c), there is a clear correlation between surface potential and the photochemical reactivity. All photocathodic terraces have more positive potentials than the photoanodic terraces, as described previously.

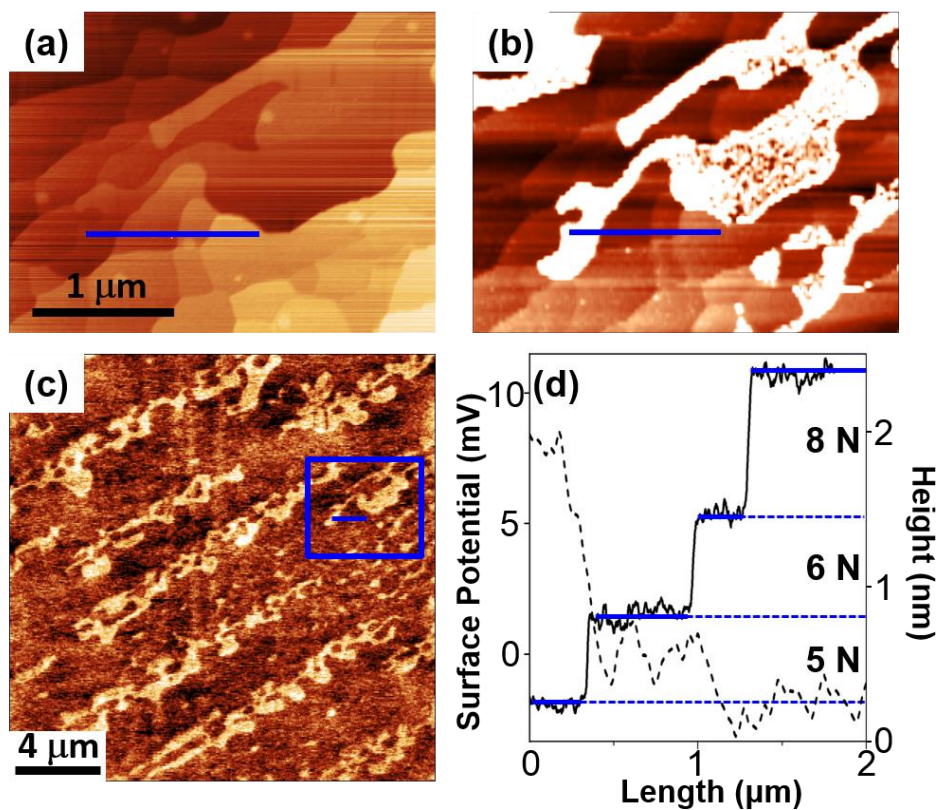


**Figure 5.6.** (a) High precision topographic AFM image recorded on the clean surface of a sample annealed with  $\text{TiO}_2$  powder. The field of view is  $3 \mu\text{m} \times 3.7 \mu\text{m}$ . (b) Image of the same area after the photoreduction of silver. (c) The surface potential image of the area shown in Fig 5.4(d). The field of view is  $20 \mu\text{m} \times 20 \mu\text{m}$ . (d) The height (solid line) and surface potential (dashed line) profiles from the location of the blue line in (a) and (c). The dark-to-light vertical contrast is: (a): 0 – 4 nm, (b): 0 – 10 nm, (c) -6 – 10 mV.

The height and surface potential profile along the line drawn in Fig. 5.6(a) and (d) are extracted and plotted in Fig. 5.6(c). The line crosses four terraces. From left to right, the first terrace was reactive for photoreduction according to the silver pattern, and the following three terraces were unreactive. As noted before, terraces separated by step heights of an even multiple of  $N$  ( $= 1.12 \text{ \AA}$ ) should have the same reactivity, and terraces separated by step heights equal to an odd multiple of  $N$  should have different reactivities. From left to right, the average heights of each terrace are  $2.34 \text{ \AA}$ ,  $8.19 \text{ \AA}$ ,  $14.71 \text{ \AA}$ , and  $23.61 \text{ \AA}$ . Therefore, the step height between the first and second terrace is  $5.85 \text{ \AA} \approx 5N$ , and the reactivity and surface potential both changed at this transition. The step heights between the second and third terraces and the third and fourth terraces are  $6.52 \text{ \AA}$  ( $6N$ ) and  $8.9 \text{ \AA}$  ( $8N$ ), respectively, and all three of these terraces are unreactive for the photoreduction of silver and have less positive potentials. The height profiles of five more lines were extracted from other locations and the step heights are all correlated with changes in reactivity and surface potential.

Experiments were also conducted to test the KFM measurement's sensitivity to the experimental conditions (see Fig. 5.7). The surface potential measured after thermal annealing is shown in Fig. 5.7 (a). The photochemical reactivity was corrected to the measured potential in the same way as was illustrated in Figs. 5.2, 5.3 and 5.6. Terraces with a more positive surface potential (bright contrast) preferentially reduce silver. The same sample was immersed in water for 20 h, and the surface potential was measured again (see Fig. 5.7 (b)). While the image does not have the same clarity as the one in Fig. 5.7 (a), it is clear the major components of the contrast are the same. After heating the sample in vacuum and imaging again, the contrast was recovered and looks identical to Fig. 5.7(a). The sample was also used to photochemically reduce silver, the silver was removed, and the surface potential was measured again (see Fig. 5.7(c)). The image in

Fig. 5.7(c) is not significantly different from the one in Fig. 5.7(a). Next, the surface potential was measured after being exposed to air for more than six months, and the contrast was not significantly different. Finally, the silver marker reaction was repeated again eight months after the initial anneal. Even after all of the treatments previously described, the pattern of reduced silver was essentially the same as in Fig. 5.4(b), with the exception of some scratches that resulted from the cleaning process to remove the silver. The fact that the surface properties are not changed by these treatments suggests that that chemical state of the surface (including hydration), is established by the original annealing treatment, and is stable for at least months in air and hours in aqueous solutions.

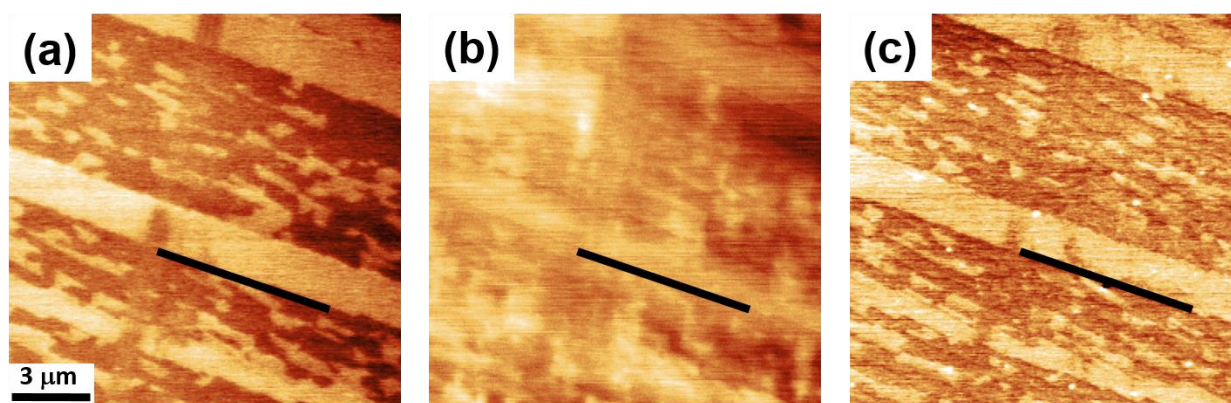


**Figure 5.7.** Surface potential images of the same location of the sample annealed with 31.4 wt% Ti powder mixtures. (a) The clean surface after thermal annealing. (b) The hydrated surface after soaking the sample in water for 20 h. (c) The surface after it was used to reduce silver and the silver was removed. All images are  $15\ \mu\text{m} \times 15\ \mu\text{m}$ . The black lines mark identical locations in the images. The vertical dark-to-light scales are 110 – 150 mV.

To explore how the elemental ratios of Sr, Ti, and O vary on surfaces annealed in different conditions, we used XPS to compare the surface chemistries of samples that are majority (55 %) photocathodic and majority (86 %) photoanodic. We note that the spectra were recorded on samples without any in vacuum treatments to remove surface contamination. Therefore, the absolute concentrations of elements on the surface are not expected to be accurate. However, we

assume the differences between the majority photoanodic and photocathodic surfaces are a meaningful measure of the relative concentration of Ti on the two surfaces. High-resolution XPS was used to measure the Sr 3d and Ti 2p spectra. The Sr/Ti atomic ratio was determined from the ratio of the integrated intensities of the Sr 3d and Ti 2p peaks.<sup>17,35</sup> We compared the sample heated with no powder (the majority photocathodic sample shown in Fig. 5.4(a)) and the one heated with pure TiO<sub>2</sub> powder (the majority photoanodic samples shown in Fig. 5.4(d)). The spectra for these samples are shown in Fig. 5.8. Consistent with previous reports,<sup>17</sup> the Sr / Ti ratios are consistently greater than one. The sample annealed with no powder and a 55 % photocathodic surface has a Sr / Ti ratio of 1.5. The sample annealed with TiO<sub>2</sub> powder and an 86 % photoanodic surface has a Sr / Ti ratio of 1.2. Based on this comparison, when the sample was annealed in the presence of excess TiO<sub>2</sub> powder, the surface averaged Sr / Ti ratio, surface potential, and photocathodic reactivity are all lower, while the photoanodic reactivity is higher. Therefore, high-temperature anneals in the presence of Sr- and Ti-containing powder reservoirs having stoichiometries different from SrTiO<sub>3</sub> can lead to modifications of the overall composition of the (111) SrTiO<sub>3</sub> single crystal surface.

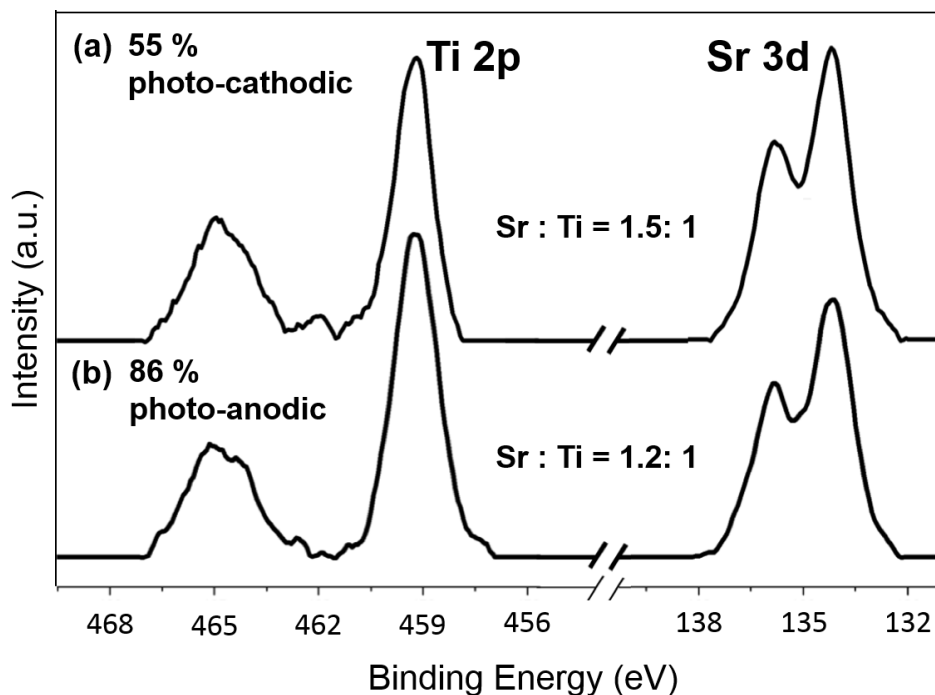


**Figure 5.8.** Ti 2p and Sr 3d core level XPS spectra from SrTiO<sub>3</sub> (111) surfaces with (a) 55 % photocathodic terraces and (b) 86 % photoanodic terraces.

The presence of hydroxyls on the surfaces was also verified by the XPS spectra of the O 1s peaks, as shown in Fig. 5.9. The main O 1s peak at 529.8 eV is ascribed to the Ti-O bonding and the second oxygen peak (the shaded area in Fig. 5.9) at 531.7 eV belongs to the hydroxyl species. The sample with the more photocathodic surface had 6 % oxygen bonded in the O-H state at surface while the more photoanodic surface has 21 %, relative to the total O 1s signal. These adsorbed species are likely to reduce the charge that is on the bare surfaces and affect the measured potential in the KFM images.

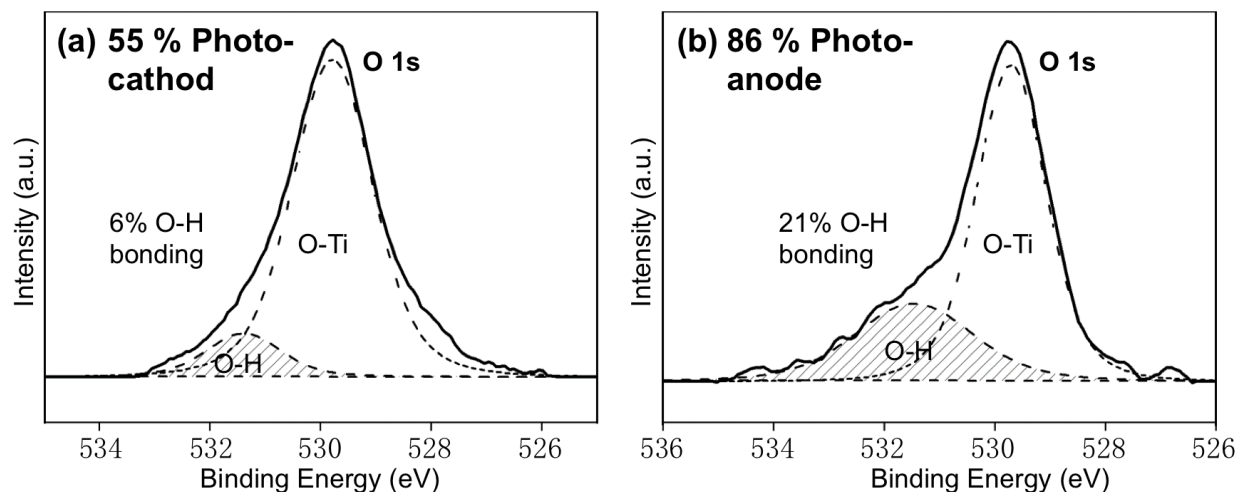


**Figure 5.9.** Oxygen 1s XPS spectra from SrTiO<sub>3</sub> (111) surfaces with (a) 55 % photocathodic terraces and (b) 86 % photoanodic terraces.

## 5.4 Discussion

The results presented here show that SrTiO<sub>3</sub> (111) surfaces annealed at 1250 °C exhibit two types of terraces that have distinct surface potentials in KFM images. The two types of terraces also have distinct photochemical properties: the terrace with the more positive surface potential is photocathodic and promotes reduction, while the terrace with the less positive surface potential is photoanodic and promotes oxidation. These observations are consistent with what has been observed on the surfaces of the polar domains of ferroelectrics,<sup>18, 36</sup> thin films supported by ferroelectrics,<sup>37, 38, 39</sup> ferroelastic materials,<sup>12, 40</sup> and on Fe<sub>2</sub>O<sub>3</sub> polycrystals.<sup>41</sup> In all cases, surfaces with a more positive potential have reduced upward (or increased downward) band bending at the surface. Therefore, it is easier for photogenerated electrons to reach the surface and participate in photoreduction reactions. For terraces with a less positive surface potential, increased upward band bending prevents electrons from getting to the surface while holes are driven “uphill” and can participate in oxidation reactions. The observation that some oxidation product appears on the

more positive, photocathodic terraces suggests that the bands are still bent upward on these surfaces, but not far enough to prevent reduction reactions from occurring. This line of argument has been supported quantitatively through simulations for thin films supported by ferroelectrics.<sup>42</sup>

After measuring the step heights between terraces on clean surfaces, it was determined that terraces of similar reactivity and surface potential were separated by even multiples of spacing between lattice planes (even- $N$ ,  $N = 1.12 \text{ \AA}$ ) that preserve the composition of the termination layer, while terraces of different reactivity were separated by odd- $N$  distances that change the composition of the termination layer. As mentioned before, all terraces, regardless of the type of reconstruction present, are separated by integer multiples of  $1.12 \text{ \AA}$  for  $\text{SrTiO}_3(111)$ .<sup>18, 25</sup> According to the model of the ideal, unreconstructed  $\text{SrTiO}_3(111)$  surface (illustrated in Fig. 5.1(b)), the Ti and  $\text{SrO}_3$  terminated surfaces have formal charges of +4 and -4, respectively. However, real terraces are unlikely to have these compositions and charges. Analysis of the  $\text{SrTiO}_3(111)$  surfaces using experiments such as mass spectroscopy of recoiled ions and coaxial impact-collision ion scattering spectroscopy lead to the conclusion that the surface in vacuum is Ti-rich,<sup>23</sup> or terminated by  $\text{TiO}_x$  layers.<sup>25, 43, 44</sup> When heated in vacuum, it has been shown that the  $\text{SrTiO}_3(111)$  surface reconstructs into a variety of Ti-rich structures with  $(n \times n)$  repeat units, with  $2 \leq n \leq 6$ .<sup>15</sup> The high temperature annealing used in the present experiments may have also led to surface modifications, but not necessarily those that have been observed in vacuum.

For  $\text{SrTiO}_3$  in aqueous solutions, the surfaces are covered with adsorbates, such as  $\text{OH}^-$ . For example, it has been reported that  $\text{H}_2\text{O}$  and  $\text{O}_2$  chemisorb on the reduced  $\text{SrTiO}_3(111)$  surface terminated by  $\text{Ti}^{3+}$ .<sup>16</sup> When irradiated with band gap light in vacuum, oxygen has been reported to photodesorb from the surface. However, illumination also increases the concentration of surface hydroxyls. Here, we have found that the photoanodic surface has more hydroxyls than the

photocathodic surface. This likely affects the surface charge and the measured potential in the KFM images.

The work function of the ideal  $\text{Ti}^{4+}$  termination is calculated to be 0.6 eV greater than the work function of the ideal  $\text{SrO}_3^{4+}$  termination.<sup>43</sup> The differences in the work functions of various  $\text{TiO}_x$  and  $\text{SrO}_x$  reconstructed surfaces are calculated to fall in the range of 0.3 to 0.8 eV and, in all cases, the  $\text{TiO}_x$  termination has a larger work function than the  $\text{SrO}_x$  termination.<sup>19</sup> These values are obviously larger than any of the potential differences that we measure with KFM. This is not surprising for measurements made in the ambient. For example, we regularly set up the instrument using a Pt-Au calibration standard. While these two metals have a work function difference of 0.6 eV, the difference in potential measured by ambient KFM is in the range of 20 to 30 mV. This reduction in measured potential difference is similar in magnitude to the difference we observe on the photoanodic and photocathodic terraces (about 10 mV). Measurements of the  $\text{SrTiO}_3$  (100) surface in vacuum with mixed terminations have also shown that there are potential differences between terraces of different termination (on the order of tens of mV), and that the actual difference was very sensitive to the surface preparation and Sr concentration.<sup>20</sup> All of these calculations and observations are consistent with the evidence presented here that terraces on the  $\text{SrTiO}_3$  (111) surface with different compositions have different potentials.

The reconstruction of the surface and the adsorption of charged species are thought to influence photochemical reactions on other oxides, such as hematite. Hematite's structure indicates its  $(1\bar{2}10)$  prismatic plane is polar terminated and its  $(1\bar{1}02)$  rhombohedral plane is charge neutral. However, KFM images of air-annealed hematite show that the  $(1\bar{2}10)$  plane has a very different surface potential and is the most reactive orientation for silver-reduction. The unexpected high surface potential on  $\text{Fe}_2\text{O}_3$  ( $1\bar{1}02$ ) may be caused by adsorbed hydroxyl species

and possibly surface reconstructions.<sup>41</sup> That the surface potential and reactivity are correlated on both the single crystal terraces and averaged over individual grains of polycrystals implies that these observations are a potentially generic avenue towards controlling spatially selective reactivity in photocatalysts.

Controlling the surface termination of a single crystal of SrTiO<sub>3</sub> using a reservoir of powders represents a straightforward and complementary method to vacuum annealing and solution chemical treatments developed for surface engineering thin film substrates<sup>21, 22, 23, 24</sup> for improved film growth.<sup>25, 45</sup> This process must work through a vapor phase interaction between the crystal surface and the powder reservoir during the annealing treatments, which results in a controllable modification in the ratio of photocathodic to photoanodic terraces. At these temperatures, the vapor pressure of titania is negligible. However, the vapor pressure of SrO is measurable<sup>46</sup> and the presence of water vapor converts strontium oxide to a hydroxide that has a vapor pressure which is larger by many orders of magnitude.<sup>47</sup> Therefore, the most likely explanation for the influence of the powder reservoir on the surface termination is that SrO vapor in the furnace reacts with excess titania in the powder bed and sets up a concentration gradient for the transport of the SrO. This is consistent with the observation that as the TiO<sub>2</sub> concentration in the powder bed increases, the surfaces are increasingly depleted of Sr (the Sr:Ti intensity in XPS decreases). This is also consistent with a report showing that Sr in SrTiO<sub>3</sub> evaporates at high temperature.<sup>48</sup>

The control of the ratio of photocathodic to photoanodic sites on separate terraces has the potential to impact the development of photocatalysts for water-splitting. Water splitting using suspended oxide particles has been determined to have a lower cost than photoelectrochemical cells (PECs).<sup>49</sup> Compared to PECs, the overall quantum efficiency of powders is lower, mainly

because of the constraint that both of the redox reactions must occur on the same surface and at the same potential. In such a case, the slowest of the two half reactions will determine the overall reaction rate. The overall rate will be maximized when the net oxidation and net reduction reactions occur at the same rate. Therefore, the ideal particle would have the appropriate ratio of photocathodic and photoanodic terraces to maximize the reaction rate. The spatial separation of the terraces would have the additional benefit of suppressing the back reaction of intermediate species. The fact that the ratio of oxidizing to reducing sites can be controlled and that they are stable, suggests that it will be possible to optimize the surface structure of photocatalyst particles using procedures similar to those described here.

## 5.5 Conclusions

SrTiO<sub>3</sub> (111) surfaces annealed in air exhibit two types of terraces with distinct surface potentials. The different types of terraces are separated by odd integer multiples of the interplanar spacing, corresponding to different chemical terminations of the bulk crystal. The terraces with the more positive (less positive) surface potential have photocathodic (photoanodic) surface properties. The different types of terraces exhibit different photochemical activities for oxidation or reduction reactions, which can be rationalized by considering which photogenerated carrier is attracted to the terrace based on surface potentials. The relative surface coverage of a specific type of terrace, and the surface reactivity, can be controlled by annealing the crystal in the presence of reservoirs of TiO<sub>2</sub>/SrTiO<sub>3</sub> powders. The concentration of titanium at the surface increases with the fraction of TiO<sub>2</sub> in the powder reservoir, as does the fraction of photoanodic terraces. The

relative area of photoanodic terraces can be manipulated through this method, and we demonstrate control within the range of 45 % to 86 % of the total area.

## Reference

1. F. Han, V. S. R. Kambala, M. Srinivasan, D. Rajarathnam, and R. Naidu, "Tailored titanium dioxide photocatalysts for the degradation of organic dyes in wastewater treatment: A review," *Appl. Catal., A*, 359[1-2] 25-40 (2009).
2. M. R. Hoffmann, S. T. Martin, W. Y. Choi, and D. W. Bahnemann, "Environmental applications of semiconductor photocatalysts," *Chem. Rev.*, 95[1] 69-96 (1995).
3. M. Kitano and M. Hara, "Heterogeneous photocatalytic cleavage of water," *J. Mater. Chem.*, 20[4] 627-41 (2010).
4. A. Kudo and Y. Miseki, "Heterogeneous photocatalyst materials for water splitting," *Chem. Soc. Rev.*, 38[1] 253-78 (2009).
5. F. E. Osterloh, "Inorganic nanostructures for photoelectrochemical and photocatalytic water splitting," *Chem. Soc. Rev.*, 42[6] 2294-320 (2013).
6. F. E. Osterloh and B. A. Parkinson, "Recent developments in solar water-splitting photocatalysis," *MRS Bull.*, 36[1] 17-22 (2011).
7. M. Batzill, "Fundamental aspects of surface engineering of transition metal oxide photocatalysts," *Energy Environ. Sci.*, 4[9] 3275-86 (2011).
8. A. Kakekhani and S. Ismail-Beigi, "Ferroelectric-Based Catalysis: Switchable Surface Chemistry," *ACS Catal.*, 5[8] 4537-45 (2015).
9. L. Li, P. A. Salvador, and G. S. Rohrer, "Photocatalysts with internal electric fields," *Nanoscale*, 6[1] 24-42 (2014).
10. L. Li, G. S. Rohrer, and P. A. Salvador, "Heterostructured Ceramic Powders for Photocatalytic Hydrogen Production: Nanostructured TiO<sub>2</sub> Shells Surrounding Microcrystalline (Ba,Sr)TiO<sub>3</sub> Cores," *J. Am. Ceram. Soc.*, 95[4] 1414-20 (2012).
11. L. Li, Y. L. Zhang, A. M. Schultz, X. Liu, P. A. Salvador, and G. S. Rohrer, "Visible light photochemical activity of heterostructured PbTiO<sub>3</sub>-TiO<sub>2</sub> core-shell particles," *Catal. Sci. Technol.*, 2[9] 1945-52 (2012).
12. R. Munprom, P. A. Salvador, and G. S. Rohrer, "Ferroelastic domains improve photochemical reactivity: a comparative study of monoclinic and tetragonal (Bi<sub>1-0.5x</sub>Na<sub>0.5x</sub>)(V<sub>1-x</sub>Mo<sub>x</sub>)O<sub>4</sub> ceramics," *J. Mater. Chem. A* (2016).
13. J. M. Lehn, J. P. Sauvage, and R. Ziessel, "Photochemical water splitting continuous generation of hydrogen and oxygen by irradiation of aqueous suspensions of metal loaded strontium-titanate," *New J. Chem.*, 4[11] 623-27 (1980).
14. T. K. Townsend, N. D. Browning, and F. E. Osterloh, "Nanoscale Strontium Titanate Photocatalysts for Overall Water Splitting," *Acs Nano*, 6[8] 7420-26 (2012).
15. B. C. Russell and M. R. Castell, "Surface of sputtered and annealed polar SrTiO<sub>3</sub>(111): TiO<sub>x</sub>-rich ( $n \times n$ ) reconstructions," *J. Phys. Chem. C*, 112[16] 6538-45 (2008).
16. S. Ferrer and G. A. Somorjai, "UPS and XPS studies of chemisorption of O<sub>2</sub>, H<sub>2</sub>, and H<sub>2</sub>O on reduced and stoichiometric SrTiO<sub>3</sub>(111) surfaces - the effects of illumination," *Surf. Sci.*, 94[1] 41-56 (1980).
17. P. V. Nagarkar, P. C. Searson, and F. D. Gealy, "Effect of surface-treatment on SrTiO<sub>3</sub> - an X-ray photoelectron spectroscopic study," *J. Appl. Phys.*, 69[1] 459-62 (1991).
18. J. L. Giocondi and G. S. Rohrer, "Structure sensitivity of photochemical oxidation and reduction reactions on SrTiO<sub>3</sub> surfaces," *J. Am. Ceram. Soc.*, 86[7] 1182-89 (2003).
19. A. Pojani, F. Finocchi, and C. Noguera, "Polarity on the SrTiO<sub>3</sub> (111) and (110) surfaces," *Surf. Sci.*, 442[2] 179-98 (1999).

20. L. Aballe, S. Matencio, M. Foerster, E. Barrena, F. Sanchez, J. Fontcuberta, and C. Ocal, "Instability and Surface Potential Modulation of Self-Patterned (001)SrTiO<sub>3</sub> Surfaces," *Chem. Mater.*, 27[18] 6198-204 (2015).
21. T. D. Doan, J. L. Giocondi, G. S. Rohrer, and P. A. Salvador, "Surface engineering along the close-packed direction of SrTiO<sub>3</sub>," *J. Cryst. Growth*, 225[2-4] 178-82 (2001).
22. W. M. Sigmund, M. Rotov, Q. D. Jiang, J. Brunen, J. Zegenhagen, and F. Aldinger, "A titanium-rich (111) surface of SrTiO<sub>3</sub> single crystals by thermal annealing," *Appl. Phys. A Mater. Sci. Process.*, 64[2] 219-20 (1997).
23. A. Biswas, P. B. Rossen, C. H. Yang, W. Siemons, M. H. Jung, I. K. Yang, R. Ramesh, and Y. H. Jeong, "Universal Ti-rich termination of atomically flat SrTiO<sub>3</sub> (001), (110), and (111) surfaces," *Appl. Phys. Lett.*, 98[5] 051904 (2011).
24. J. Chang, Y.-S. Park, and S.-K. Kim, "Atomically flat single-terminated SrTiO<sub>3</sub> (111) surface," *Appl. Phys. Lett.*, 92[15] 152910 (2008).
25. I. Hallsteinsen, M. Nord, T. Bolstad, P.-E. Vullum, J. E. Boschker, P. Longo, R. Takahashi, R. Holinestad, M. Lippmaa, and T. Tybell, "Effect of Polar (111)-Oriented SrTiO<sub>3</sub> on Initial Perovskite Growth," *Cryst. Growth Des.*, 16[4] 2357-62 (2016).
26. S. Dunn, P. M. Jones, and D. E. Gallardo, "Photochemical growth of silver nanoparticles on c- and c+ domains on lead zirconate titanate thin films," *J. Am. Chem. Soc.*, 129[28] 8724-28 (2007).
27. J. L. Giocondi and G. S. Rohrer, "Spatial separation of photochemical oxidation and reduction reactions on the surface of ferroelectric BaTiO<sub>3</sub>," *J. Phys. Chem. B*, 105[35] 8275-77 (2001).
28. R. Li, F. Zhang, D. Wang, J. Yang, M. Li, J. Zhu, X. Zhou, H. Han, and C. Li, "Spatial separation of photogenerated electrons and holes among {010} and {110} crystal facets of BiVO<sub>4</sub>," *Nat. Commun.*, 4 1432 (2013).
29. J. B. Lowekamp, G. S. Rohrer, P. A. M. Hotsenpiller, J. D. Bolt, and W. E. Farneth, "Anisotropic photochemical reactivity of bulk TiO<sub>2</sub> crystals," *J. Phys. Chem. B*, 102[38] 7323-27 (1998).
30. R. Munprom, P. A. Salvador, and G. S. Rohrer, "The orientation dependence of the photochemical reactivity of BiVO<sub>4</sub>," *J. Mater. Chem. A*, 3[5] 2370-77 (2015).
31. Gwyddion, "Available from World Wide Web: <http://gwyddion.net/resources.php>." in., 2011.
32. N. Fairley, "CasaXPS VAMAS processing software." in *Available from World Wide Web: <http://www.casaxps.com>*. (2010).
33. K. Tanaka, K. Harada, and S. Murata, "Photocatalytic deposition of metal-ions onto TiO<sub>2</sub> powder," *Sol. Energy*, 36[2] 159-61 (1986).
34. J. Torres and S. Cerveramarch, "Kinetics of the photoassisted catalytic-oxidation of Pb(II) in TiO<sub>2</sub> suspensions," *Chem. Eng. Sci.*, 47[15-16] 3857-62 (1992).
35. T. Hikita, T. Hanada, M. Kudo, and M. Kawai, "Structure and electronic state of the TiO<sub>2</sub> and SrO terminated SrTiO<sub>3</sub>(100) surfaces," *Surf. Sci.*, 287 377-81 (1993).
36. A. Schultz, Y. Zhang, P. Salvador, and G. Rohrer, "Effect of Crystal and Domain Orientation on the Visible-Light Photochemical Reduction of Ag on BiFeO<sub>3</sub>," *ACS Appl. Mater. Interfaces*, 3[5] 1562-67 (2011).
37. N. V. Burbure, P. A. Salvador, and G. S. Rohrer, "Photochemical Reactivity of Titania Films on BaTiO<sub>3</sub> Substrates: Origin of Spatial Selectivity," *Chem. Mater.*, 22[21] 5823-30 (2010).

38. N. V. Burbure, P. A. Salvador, and G. S. Rohrer, "Photochemical Reactivity of Titania Films on BaTiO<sub>3</sub> Substrates: Influence of Titania Phase and Orientation," *Chem. Mater.*, 22[21] 5831-37 (2010).
39. Y. L. Zhang, A. M. Schultz, P. A. Salvador, and G. S. Rohrer, "Spatially selective visible light photocatalytic activity of TiO<sub>2</sub>/BiFeO<sub>3</sub> heterostructures," *J. Mater. Chem.*, 21[12] 4168-74 (2011).
40. R. Munprom, P. A. Salvador, and G. S. Rohrer, "Polar Domains at the Surface of Centrosymmetric BiVO<sub>4</sub>," *Chemistry of Materials*, 26[9] 2774-76 (2014).
41. Y. Zhu and A. M. R. Schultz, Gregory S. Salvador, Paul A., "The Orientation Dependence of the Photochemical Activity of  $\alpha$ -Fe<sub>2</sub>O<sub>3</sub>," *J. Am. Ceram. Soc.* (2016).
42. J. J. Glickstein, P. A. Salvador, and G. S. Rohrer, "A Computational Model of Domain Specific Reactivity on Coated Ferroelectric Photocatalysts," *J. Phys. Chem. C*, DOI: 10.1021/acs.jpcc.6b03875 in press (2016).
43. A. N. Chiamonti, C. H. Lanier, L. D. Marks, and P. C. Stair, "Time, temperature, and oxygen partial pressure-dependent surface reconstructions on SrTiO<sub>3</sub>(111): A systematic study of oxygen-rich conditions," *Surf. Sci.*, 602[18] 3018-25 (2008).
44. L. D. Marks, A. N. Chiamonti, F. Tran, and P. Blaha, "The small unit cell reconstructions of SrTiO<sub>3</sub>(111)," *Surf. Sci.*, 603[14] 2179-87 (2009).
45. J. L. Blok, X. Wan, G. Koster, D. H. A. Blank, and G. Rijnders, "Epitaxial oxide growth on polar (111) surfaces," *Appl. Phys. Lett.*, 99[15] 151917 (2011).
46. R. H. Lamoreaux, D. L. Hildenbrand, and L. Brewer, "High-temperature vaporization behavior of oxides 2. Oxides of Be, Mg, Ca, Sr, Ba, B, Al, Ga, In, Tl, Si, Ge, Sn, Pb, Zn, Cd, and Hg," *J. Phys. Chem. Ref. Data*, 16[3] 419-43 (1987).
47. T. Zhang and S. Wang, "Seals for Planar Solid Oxide Fuel Cells: The State of the Art," pp. 58. in *Nanostructured and Advanced Materials for Fuel Cells*. Edited by S. P. Jiang and P. K. Shen. CRC Press, Taylor Francis Group, Boca Raton, FL, 2008.
48. Z. Wang, F. Yang, Z. Zhang, Y. Tang, J. Feng, K. Wu, Q. Guo, and J. Guo, "Evolution of the surface structures on SrTiO<sub>3</sub>(110) tuned by Ti or Sr concentration," *Phys. Rev. B*, 83[15] 155453 (2011).
49. R. Sathre, C. D. Scown, W. R. Morrow, III, J. C. Stevens, I. D. Sharp, J. W. Ager, III, K. Walczak, F. A. Houle, and J. B. Greenblatt, "Life-cycle net energy assessment of large-scale hydrogen production via photoelectrochemical water splitting," *Energy Environ. Sci.*, 7[10] 3264-78 (2014).

## Chapter 6 Controlling the Termination and Photochemical Reactivity of the SrTiO<sub>3</sub> (110) Surface

*(110) orientated SrTiO<sub>3</sub> crystals have been heated to temperatures between 1000 °C and 1200 °C in air, alone or in the presence of TiO<sub>2</sub> or Sr<sub>3</sub>Ti<sub>2</sub>O<sub>7</sub> powder reservoirs. In these conditions, the surface is terminated by two types of atomically flat terraces. One has a relatively higher surface potential and promotes the photochemical reduction of silver (it is photocathodic) and the other promotes the photochemical oxidation of lead (it is photoanodic). Measurements of the step heights between the terraces indicate that the surfaces with different properties have different terminations. By adjusting the time and temperature of the anneal, and in some cases including reservoirs of TiO<sub>2</sub> or Sr<sub>3</sub>Ti<sub>2</sub>O<sub>7</sub>, it is possible to change the surface from 98 % photocathodic to 100 % photoanodic. The surface is more photocathodic when the annealing temperature is lower, the durations shorter, and if Sr<sub>3</sub>Ti<sub>2</sub>O<sub>7</sub> is present. The surface more photoanodic if the temperature is higher, the annealing duration longer, and if TiO<sub>2</sub> is present.*

## 6.1 Introduction

Photocatalysis is a promising method for the large scale production of hydrogen, a high energy density clean energy source, by directly splitting water using solar energy.<sup>1,2,3,4</sup> To split water, photogenerated electrons and holes must migrate to the catalyst surface where they can reduce and oxidize water to produce hydrogen and oxygen, respectively. For colloidal catalysts, the reduction and oxidation reactions must happen on the surface of one particle and with no externally applied potential. These conditions lead to enhanced photogenerated charge carrier recombination and the back-reaction of reduced and oxidized species and, as a result, efficiencies are low.<sup>1,5</sup> The low sunlight to hydrogen conversion efficiency is one of the reasons that photocatalysis is not yet a commercial technology for water splitting. While it is not possible to apply an external field that would separate charges and reduce recombination, it is possible in some materials to control internal fields that influence the charge carrier transport near the surface. It has been reported that internal fields resulting from ferroelectric polarization,<sup>6</sup> phase boundaries,<sup>7</sup> and flexoelectric phenomena<sup>8</sup> can increase efficiency by separating photogenerated electrons and holes and reducing recombination.<sup>9</sup> In this paper, we show how electric fields between terraces on the same surface that have different potentials can be controlled to influence the photochemical activity on oxide surface.

The surface potential of a semiconductor is determined by the work function and any surface charges that might be present. For an n-type semiconductor, a positive surface charge or a reduced work function results in a greater surface potential. This bends the energy bands downward as they approach the surface and this increases the concentration of electrons on the surface. On the other hand, negative surface charge or a larger work function leads to a lower surface potential value and the resulting upward band bending will attract holes to surface. There

are a number of materials that have been shown to have, on the same surface, relatively electron rich areas that promote reduction reactions (we will refer to such surfaces as photocathodic) and relatively hole rich areas that promote oxidation reactions (we will refer to such surfaces as photoanodic).<sup>10, 11, 12, 13</sup> In such cases, it would obviously be advantageous to be able to control the ratio of the photoanodic to photocathodic areas so that reduction and oxidation could occur at equal rates to optimize efficiency. We recently showed that on the SrTiO<sub>3</sub> (111) surface, it was possible to make surfaces that had from 45 % and 86 % of the area photoanodic.<sup>14</sup> Here, we show that the more stable SrTiO<sub>3</sub> (110) surface can be made 100 % photoanodic, 98 % photocathodic, or any combination in between.

Strontium titanate (SrTiO<sub>3</sub>) is a well-known perovskite structured ( $a = 3.905 \text{ \AA}$ ,  $E_g = 3.2 \text{ eV}$ )<sup>15, 16</sup> photocatalyst that can split water under UV-light irradiation.<sup>17, 18</sup> As illustrated in Fig. 6.1, the SrTiO<sub>3</sub> (110) surface is polar, which means that it is terminated in such a way that any atomically flat terrace must have a net charge. For example, the unreconstructed polar SrTiO<sub>3</sub> (110) surface can be either SrTiO<sup>4+</sup> terminated or O<sub>2</sub><sup>4-</sup> terminated. It has already been shown that this leads to photocathodic and photoanodic terraces.<sup>11</sup> As indicated in Fig. 6.1, the spacing between these two layers is  $N = \sqrt{2}/4a = 1.38 \text{ \AA}$ , and terraces of the same (different) chemical component are separated by even-N (odd-N). Because the samples in our experiments are exposed to air and aqueous solutions, the real SrTiO<sub>3</sub> (110) polar surface is likely to differ from the ideal bulk termination, possibly be reconstructed,<sup>19, 20, 21, 22, 23, 24</sup> and definitely have a layer of adsorbates.<sup>25, 26</sup> Because of these factors, the amount of surface charge and the extent of the associated space charge region is difficult to estimate. In this research, Kelvin Probe Force Microscopy (KFM) is used to measure the local surface potential and how it varies on different

atomically flat terraces. Furthermore, topographic measurements will be used to determine if changes in potential are correlated to steps of odd-N height.

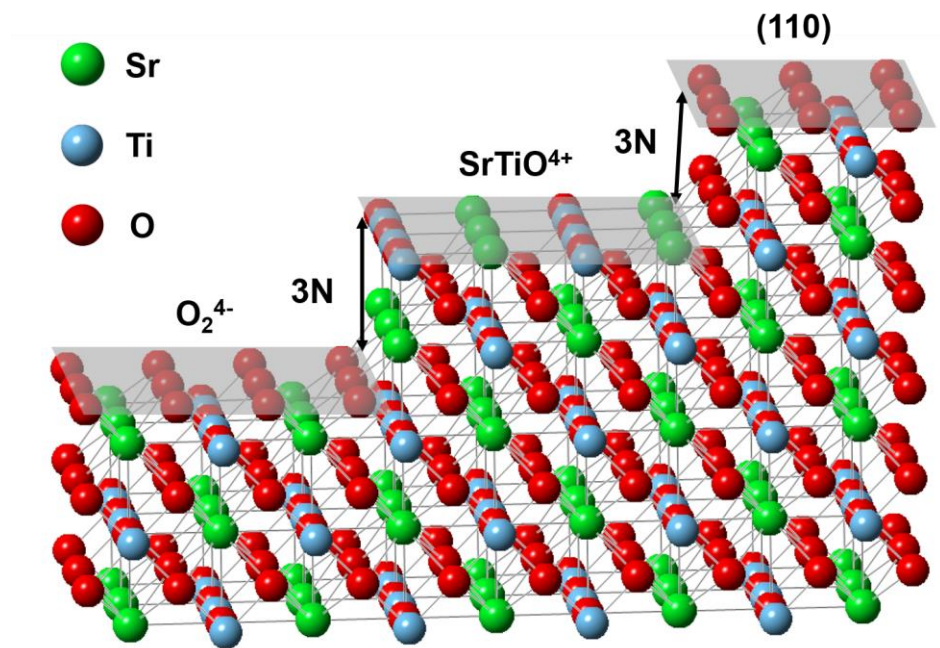


**Figure 6.1.** Schematic of SrTiO<sub>3</sub> viewed along [001] direction. The (110) planes is highlighted by the transparent blue planes. Along the [110] direction, SrTiO<sub>3</sub> is comprised of alternating SrTiO<sub>4</sub><sup>+</sup> and O<sub>2</sub><sup>4-</sup> atomic layers separated by  $N = 1.38 \text{ \AA}$ .

SrTiO<sub>3</sub> (110) surfaces with uniform oxygen termination have been prepared by thermal annealing in ultra high vacuum<sup>27</sup> and by etching with a buffered hydrogen fluoride solution.<sup>28</sup> These studies were motivated by the desire to have completely uniform surfaces that promote heteroepitaxial crystal growth. In this paper, we show that high temperature annealing can be used to continuously tune the ratio of photocathodic to photoanodic area and, by controlling this ratio, we also control the photochemical properties of the surface.

## 6.2 Experimental Procedure

A chemical-mechanical polished SrTiO<sub>3</sub> (110) single crystal (MTI company, 1 cm × 1 cm, (110) ± 0.5°, roughness < 5 Å) was cut into 16 smaller pieces (2.5 mm × 2.5 mm each). Each sample was ultrasonicated in a methanol bath for 10 min, placed in a covered rectangular alumina combustion boat, heated in a muffle furnace (to 1000 °C, 1100 °C or 1200 °C) at a rate of 10 °C/min, annealed 0 to 24 h, and then cooled at 10 °C/min. After annealing, atomically flat terraces were observed by atomic force microscopy (AFM) (Solver-Next, NT-MDT, Russia). To control the ratio of photoanodic to photocathodic surfaces, some samples were annealed with reservoirs of TiO<sub>2</sub> or Sr<sub>3</sub>Ti<sub>2</sub>O<sub>7</sub> powder. In these experiments, the SrTiO<sub>3</sub> (110) crystal was put at the center of the combustion boat and the powder reservoirs were placed around, but not in contact with, the crystal. The combustion boat was then covered and heated to the designated temperature using the same heating and cooling rate described above.

The photoreduction of Ag<sup>+</sup> and the photooxidation of Pb<sup>2+</sup> leave insoluble products on the surface at the site of the reaction and are therefore used to mark the locations of the photoreduction and photooxidation reactions.<sup>10, 11, 12, 13, 29</sup> The fiber optic waveguide attached to a 300 W mercury lamp (Newport, Irvine, CA) was used for illumination. For Ag reduction, the sample was exposed to the light for 4 to 30 seconds and for lead oxidation, 90 to 150 seconds exposures were used. The larger photocathodic (photoanodic) surface coverage, the longer silver reduction (lead oxidation) reaction time. The need for longer exposures for the lead oxidation is thought to be related to the complexity of the reaction. The lead oxidation reaction involves oxygen and the reaction rate is affected by the solution pH.<sup>30, 31</sup> After illumination, the SrTiO<sub>3</sub> (110) sample was rinsed with de-ionized water and dried using a stream of 99.995% nitrogen gas. The products from

these two marker reactions can be removed by ultra-sonication in acetone and methanol baths for 10 minutes each, and then swiping the surface with cotton swab.

The topography of annealed SrTiO<sub>3</sub> (110) surface before reaction and the distribution of photochemical reaction products at the same location after reaction was determined by AFM imaging in tapping mode. High-precision AFM images were used to measure the step height between neighboring terraces. As mentioned before, the SrTiO<sub>3</sub> (110) terraces are separated by integer multiples of 1.38 Å. The high-precision AFM has a noise level of 0.3 Å, making it possible to measure the difference between even-N and odd-N step heights. All topographic images were made with an alumina coated silicon probe with a tip radius of < 10 nm (Tap 300AL-G, budget sensor). The local surface potential of each terrace was measured using Kelvin probe force microscopy (KFM), using a silicon AFM probe with a PtCr (190E-G, budget sensor) conductive coating. KFM images of the relevant areas of the clean surface were collected before the photochemical reactions. All of the scanning probe microscopy data were processed and analyzed using the Gwyddion software package.<sup>32</sup>

### 6.3 Results

The topography of the clean SrTiO<sub>3</sub> (110) surface after annealing for 6 h in air at 1200 °C is shown in Fig. 6.2(a). After annealing, the surface is covered by atomically flat terraces. From the image, it is obvious that one set of atomic terraces has brighter contrast; these terraces are 0.4 nm to 1 nm higher than their neighboring terraces. The surface potential image of the same area is shown in Fig. 6.2(b). There are two dominant contrast levels such that the potential of one set of terraces is 10 – 25 mV higher than the other set of terraces. When compared to Fig. 6.2(a),

it is clear that those terraces that are 0.4 nm to 1 nm higher than their surroundings also have the higher surface potential.

After the sample was illuminated by a mercury lamp in the lead acetate (silver nitrate) solution, new contrast appeared on the surface, corresponding to Pb-containing deposits (metallic silver) as shown in Fig. 6.2(c) (Fig. 6.2(d)). These two images show that part of the surface is photocathodic and promotes reduction and the rest of the surface is photoanodic and promotes oxidation. We refer to this as complimentary reactivity. When the marker reaction results are correlated with the surface potential image, we find that the low surface potential terraces are only reactive for photooxidation of lead and the high surface potential terraces are only reactive for photoreduction of silver. This is consistent with observations of the SrTiO<sub>3</sub> (111) surface.<sup>14</sup> Based on the coverage of reaction products in this area, 74 % of the area is photoanodic (oxidizes lead) and 26 % is photocathodic (reduces silver).

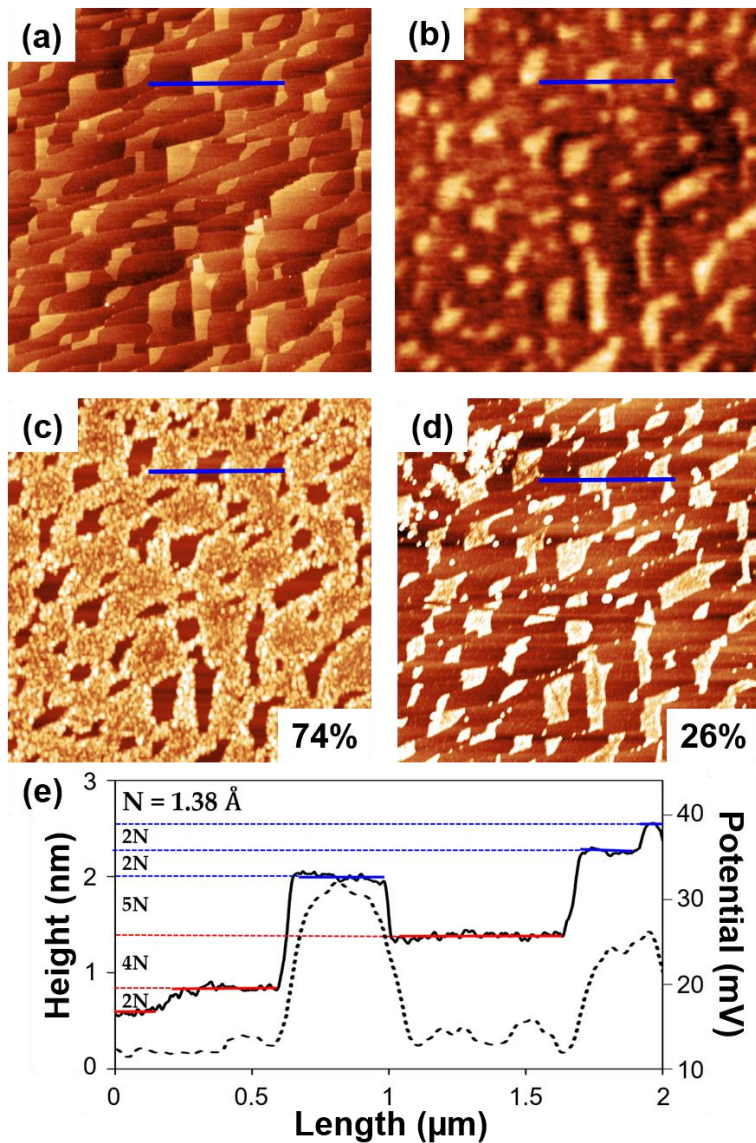


**Figure 6.2.** (a) Topographic AFM image (b) surface potential image (c) topographic image after lead photooxidation (d) topographic image after silver photoreduction. (a-d) are the same area of the surface and have a  $5 \mu\text{m} \times 5 \mu\text{m}$  field of view. The blue lines mark the same location in each image. The color range from dark-to-light is: (a) 0 – 2 nm, (b) 0 to 40 mV (c) 0 – 6 nm and (d) 0 – 4 nm. In (c) and (d), the fractional coverage of photoanodic and photocathodic terraces, respectively, are given in the lower right corner. In (e), the black solid line is the height cross-section at the position of the blue line and the dashed line is potential profile at the same position. Red lines mark the photoanodic terraces and blue lines mark the photocathodic terraces.

The high-precision AFM height profile and the surface potential profile along the blue lines drawn in Fig. 6.2(a) and (b) are extracted and plotted as solid and dashed lines, respectively, in Fig. 6.2(e). The line crosses six atomically flat terraces. The same location is also marked in Fig.

6.2(c) and Fig. 6.2(d). From left to right, the first, second and fourth terraces (marked by the red lines in Fig. 6.2(e)) are all reactive for photooxidation of lead according to Fig. 6.2(c). The average heights of these three terraces are 5.59 Å, 8.19 Å and 13.75 Å. As noted before, terraces separated by an even multiple of N ( $N = 1.38 \text{ \AA}$ ) should have the same chemical termination. The step heights from the first to second terrace and the second to fourth terrace are  $2.60 \text{ \AA} \approx 2N$  and  $5.56 \approx 4N$  respectively. Therefore, these three terraces have the same type of termination, and their surface potentials are in the range of 10-14 mV. The third, fifth and sixth terraces (marked by the blue lines in Fig. 6.2(e)) all are reactive for the reduction of silver according to Fig. 6.2(d). Their step heights are 20.30 Å, 22.79 Å, and 25.47 Å from left to right. Therefore, the third to fifth terraces and fifth to sixth terraces are all separated by  $2N$ , indicating they have the same type of termination. The surface potential of these three terraces varies from 23-31 mV. Note that The third and fourth terraces are separated by  $6.55 \text{ \AA} \approx 5N$ . This means their chemical terminations are different and this presumably explains the difference in their reactivities and surface potentials.

We found that the fraction of the surface that was photoanodic depended on the length of time it was annealed at 1200 °C. The surfaces of samples annealed for 24 h (a), 12 h (b), 3 h (c) and 0 h (d) are shown in Fig. 6.3, after oxidizing lead. When we refer to a 0 h anneal, it means the sample was heated to 1200 °C and then immediately cooled. The sample that was annealed for 24 h is fully covered by Pb-containing particles (see Fig. 6.3(a)). Therefore, the surface is 100 % photoanodic. After annealing for 12 h, the area fraction of photoanodic terraces decreases to 89 % (see Fig. 6.3(b)). This trend continues with samples heated for 6 h (Fig. 6.2(d)), 3 h (Fig. 6.3(c), and 0 h (Fig. 6.3(d)), being 74 %, 60 %, and 45 % photoanodic, respectively. These results show a clear trend that as annealing time at 1200 °C increases, the fraction of the surface that is photoanodic also increases until it reaches 100 % after 24 h.

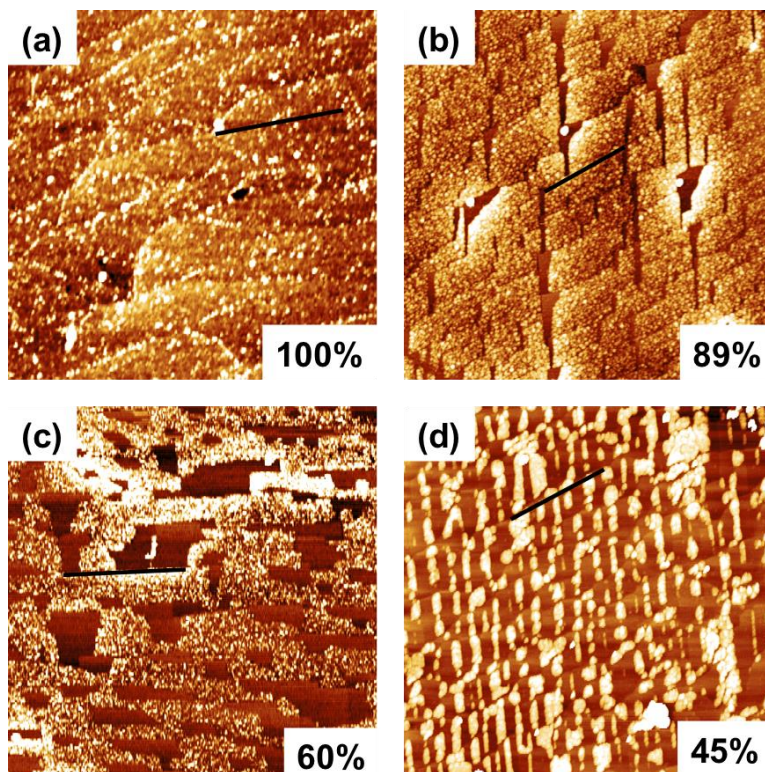


**Figure 6.3.** Topographic AFM image of samples annealed at 1200 °C for (a) 24 h (b) 12 h (c) 3 h and (d) 0 h after the photochemical oxidation of lead. All images are  $5\ \mu\text{m} \times 5\ \mu\text{m}$  laterally and the dark-to-light vertical contrast is 0 – 6 nm. The fractional coverage of photoanodic terraces is given in the lower right corner. The black lines mark the same locations that are marked in Fig. 6.4 and Fig. 6.5.

Images of the surfaces after the photochemical reduction of silver and the clean surface are shown in Figs. 6.4 and 6.5, respectively. Comparing Fig. 6.3 and Fig. 6.4 demonstrated that the reactions are complementary. Photoreduction and photooxidation reactions happen on different terraces.

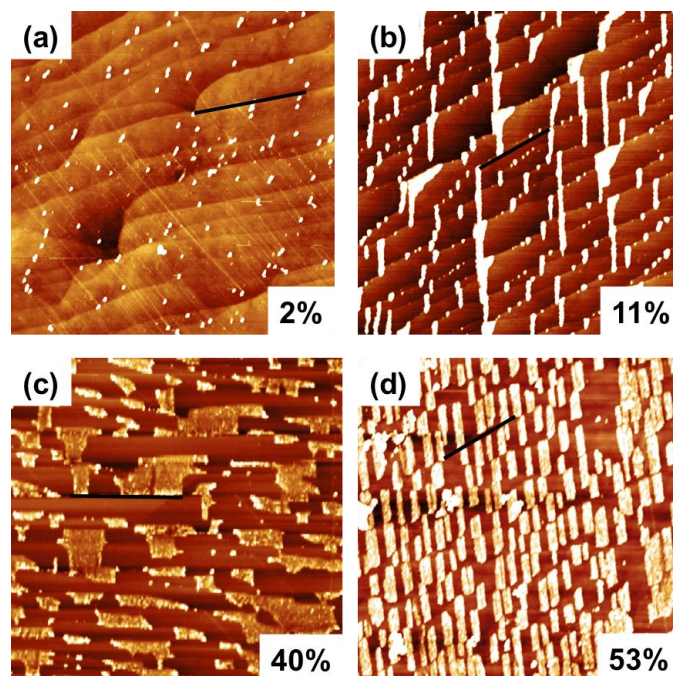


**Figure 6.4.** Surface topography AFM image of samples annealed at 1200 °C for (a) 24 hours (b) 12 hours (c) 3 hours and (d) 0 hour after the photochemical reduction of silver. All images are 5  $\mu\text{m} \times 5 \mu\text{m}$  laterally and the dark-to-light vertical scales are 0 – 4 nm. The percentage in lower corner marks the fractional coverage of photocathodic terraces in each image. The black lines mark the same locations that is marked in Fig. 6.3 and Fig. 6.5.

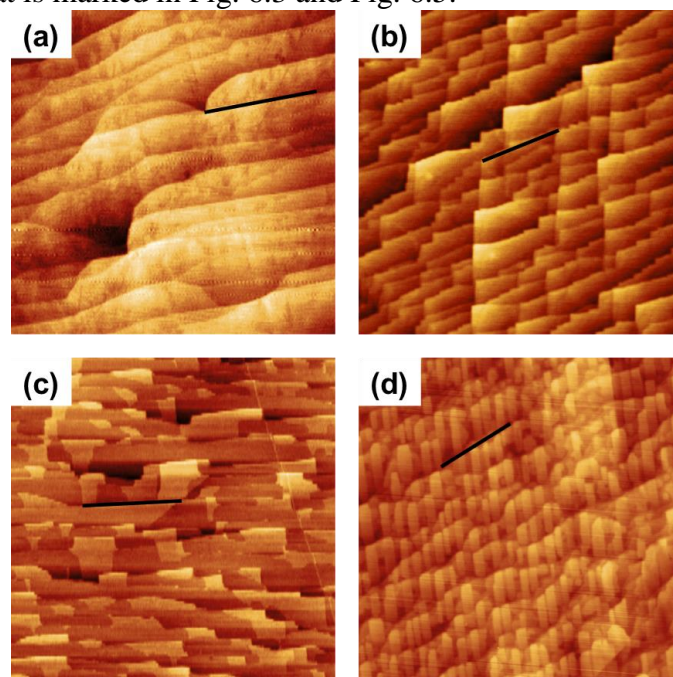


**Figure 6.5.** Surface topography AFM image scanned on clean surface of samples annealed at 1200 °C for (a) 24 hours (b) 12 hours (c) 3 hours and (d) 0. All images are 5  $\mu\text{m} \times 5 \mu\text{m}$  laterally and the dark-to-light vertical scales are 0 – 2 nm. The black lines mark the same locations that is marked in Fig. 6.3 and Fig. 6.4.

To explore the influence of temperature, four samples were annealed at 1100 °C and 1000 °C for 0 and 6 h. Figs. 6.6(a) and 6.6(b) (Figs 6.6(c) and 6.6(d)) show topographic images of the samples after the photooxidation of lead for samples heated to 1100 °C (1000 °C) for 6 h and 0 h, respectively. The trend at these temperatures is similar to what was observed at 1200 °C. The fractional coverage of photoanodic terraces increases with annealing time, from 38 % to 68 % (15 % to 32 %) for 0 h and 6 h anneals at 1100 °C (1000 °C).

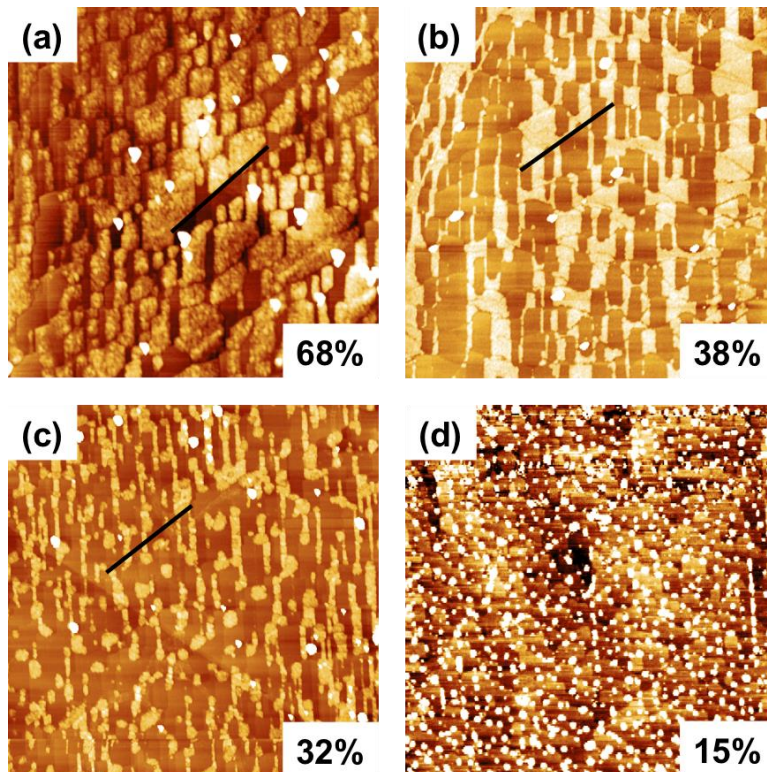
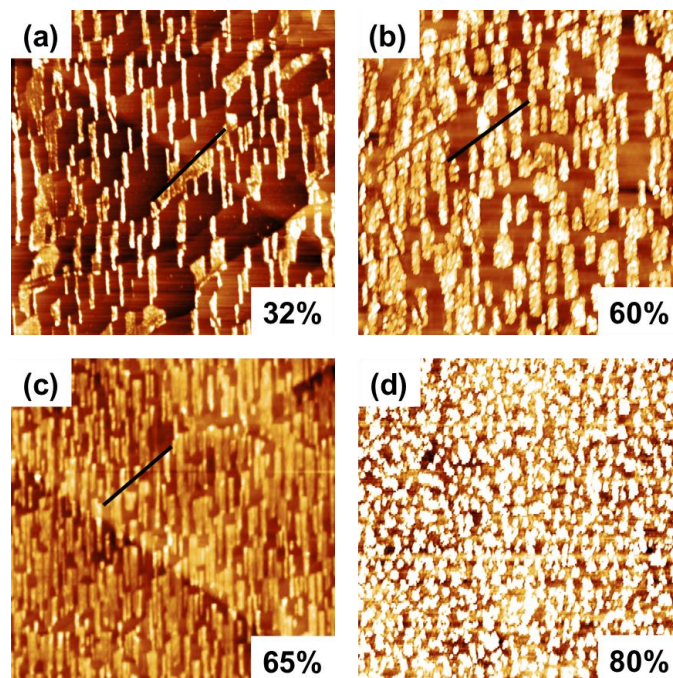


**Figure 6.6.** Topographic AFM images after lead photooxidation for samples annealed at 1100 °C for (a) 6 h (b) 0 h and samples annealed at 1000 °C for (c) 6 h (d) 0 h. Lateral image dimensions: (a) – (c) 5  $\mu\text{m}$   $\times$  5  $\mu\text{m}$  and (d) 3  $\mu\text{m}$   $\times$  3  $\mu\text{m}$ . The dark-to-light vertical scales are (a) – (c) 0 – 6 nm (d) 0 – 3 nm. The fractional coverage of photoanodic terraces is given in the lower right corner. The black lines mark the same location that is marked in Fig. 6.7 and Fig. 6.8

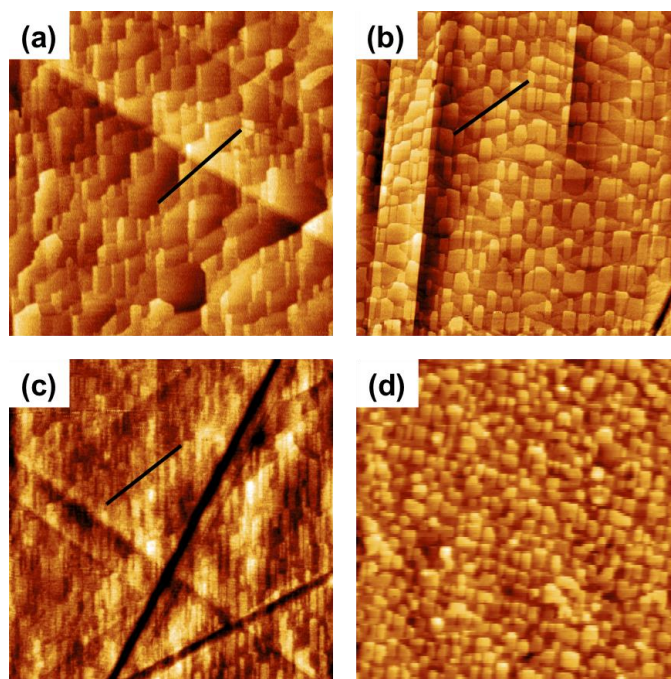
When we compare the samples annealed at different temperature for the same amount of time, we can easily conclude that the fractional coverage of photoanodic terraces also increases with increasing annealing temperature. For example, three samples were annealed for 6 h at different temperatures. The surface of the sample annealed at 1000 °C was 32 % photoanodic (see

Fig. 6.6(c)), the sample annealed at 1100 °C was 68 % photoanodic (see Fig. 6.6(a)), and the sample annealed at 1200 °C was 68 % photoanodic (see Fig. 6.2(c)). The same is true for the three samples annealed for 0 h, whose surfaces are 15 %, 38 %, and 45 % photoanodic at 1000 °C, 1100 °C, and 1200 °C, respectively.

Topographic AFM images of the surfaces after photooxidation of lead are shown in Fig. 6.6, but after the photoreduction of Ag, can be found in Fig. 6.7. As before, the oxidation and reduction reactions are complementary. The terraces reactive for the photoreduction of silver are unreactive for the photooxidation of lead and the terraces reactive for the photooxidation of lead are unreactive for the photoreduction of silver. In each case, if we determine the fraction of photocathodic surfaces by evaluating the fractional silver coverage in Figs. 6.4 and 6.7, the result is the same, within 5%, of simply subtracting the fractional photoanodic area from 100 %. Images of the clean surfaces are shown in Figs. 6.5 and 6.8. In general, the terraces that are higher than the neighboring terraces are reactive for the photoreduction of silver and the lower terraces are reactive for the photooxidation of lead. This is consistent with the result shown in Fig. 6.2.



**Figure 6.7.** Surface topography AFM image after silver photoreduction for samples annealed at 1100 °C for (a) 6 hours (b) 0 hours and samples annealed at 1000 °C for (c) 6 hours (d) 0 hours. Dimension of images are: (a) – (c) 5  $\mu\text{m} \times 5 \mu\text{m}$  and (d) 3  $\mu\text{m} \times 3 \mu\text{m}$  laterally. The dark-to-light vertical scales are 0 – 4 nm. The black lines mark the same locations that is marked in Fig. 6.6 and Fig. 6.8.



**Figure 6.8.** Surface topography AFM image scanned on clean surface of samples at 1100 °C for (a) 6 h (b) 0 h and samples annealed at 1000 °C for (c) 6 h (d) 0 h. All images are 5  $\mu\text{m} \times 5 \mu\text{m}$  laterally and the dark-to-light vertical scales are 0 – 2 nm. The black lines mark the same locations that is marked in Fig. 6.6 and Fig. 6.7.

In our previous study of SrTiO<sub>3</sub>(111), we found the surface composition could be altered by heating the sample in the presence of powder reservoirs with a different composition.<sup>14</sup> Images of a sample that was annealed at 1000 °C for 6 h surrounded by 2 g of TiO<sub>2</sub> powder are shown in Fig. 6.9. The topographic image in Fig. 6.9(a), recorded after the photooxidation of lead, shows that the sample is 79 % photoanodic. A sample annealed at the same time and temperature without the TiO<sub>2</sub> powder reservoir (Fig. 6.6(c)) was only 32 % photoanodic. Therefore, the addition of TiO<sub>2</sub> powder more than doubled the fractional coverage of the photoanodic surface. The topographic image after the reduction of silver (Fig. 6.9(b)) demonstrate the reaction is complementary. The topographic image and surface potential image of the same location before the reaction are shown in Figs 6.9(c) and 6.9(d). When the images are compared, it is clear that the terraces that are topographically higher also have a higher surface potential and promote the photoreduction reaction. In other words, they are photocathodic. The topographically lower terraces have a lower surface potential and are photoanodic. This is consistent with the observation on samples annealed without TiO<sub>2</sub> powder.

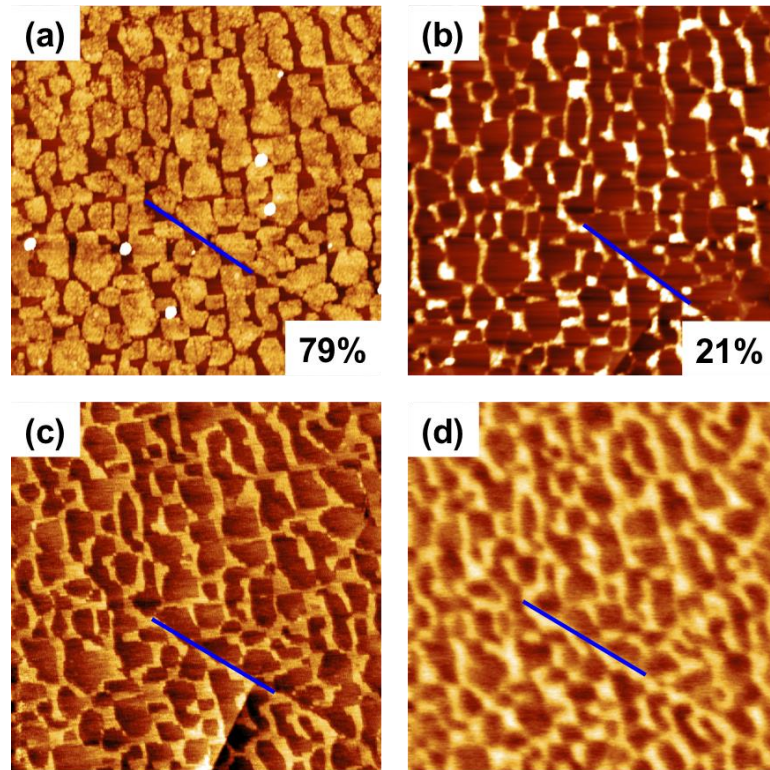


**Figure 6.9.** (a) Topographic AFM image after lead photooxidation, (b) topographic image after silver photoreduction recorded, (c) topographic image of the clean surface, and (d) surface potential image. All images are  $5 \mu\text{m} \times 5 \mu\text{m}$  and show the same area on a sample annealed with 2 g  $\text{TiO}_2$  powder at  $1000 \text{ }^\circ\text{C}$  for 6 h. The blue line marks the same locations. The vertical scale from dark-to-light is: (a) 0 to 6 nm, (b) 0 to 4 nm, (c) 0 to 2 nm and (d) 0 to 40 mV. The fractional coverage of photoanodic and photocathodic terraces in (a) and (b), respectively, are given in the lower right corners.

The results described above indicate that heating the crystals with a reservoir of  $\text{TiO}_2$  powder (Sr-poor conditions) increases the surface coverage of photoanodic terraces. To test the effect of heating in Sr-rich conditions,  $\text{SrTiO}_3$  crystals were heated with a  $\text{Sr}_3\text{Ti}_2\text{O}_7$  reservoir. In this case, the  $\text{SrTiO}_3$  sample was then annealed in a crucible with 0.02 g of  $\text{Sr}_3\text{Ti}_2\text{O}_7$  for 6 h at  $1100 \text{ }^\circ\text{C}$ . As illustrated in Fig. 6.10(a), the lead oxidation experiment indicates that only 37 % of the surface is photoanodic. For comparison, the sample heated in the same conditions without added  $\text{Sr}_3\text{Ti}_2\text{O}_7$  (see Fig. 6.6(a)) was 68 % photoanodic. As illustrated in Fig. 6.10(b), the silver reduction experiment indicated that 58 % of the surface area is photocathodic. So, as in other

cases, the oxidation and reduction reactions are complementary. In this case, the 58 % photocathodic area and the 37 % photoanodic areas do not sum to exactly 100 %. This may be because this particular surface had many very small terraces (see Fig. 6.10(c)) and our resolution of the areas covered by reduced silver or oxidized lead was not sufficient to distinguish all of the small terraces. The results show that heating  $\text{SrTiO}_3$  with a small amount of  $\text{Sr}_3\text{Ti}_2\text{O}_7$  changes the surface from majority photoanodic to majority photocathodic.

The surface potential image of the clean surface, at the same location, is shown in Fig. 6.10(d). Compare Fig. 6.10(d) with Fig. 6.10(b), it is clear that the same correlation that was observed in the previous experiments; the areas with the highest surface potentials are photocathodic and the areas with lower surface potentials are photoanodic. However, the contrast is weaker than in the other two KFM images (Figs 6.2(b) and 6.9(d)). It is likely that this is also an artifact of the small terrace width. The radius of the KFM probe is  $\sim 25$  nm and the lateral resolution of KFM images is  $> 100$  nm.<sup>33</sup> This is comparable to the average terrace width, which is about 250 nm. Because the terraces are closely spaced, in many locations the tip is influenced by a combination of photoanodic and photocathodic terraces, and the measured potential at any point is an average of those in the neighborhood and it does not reach maximums that are as high or minimums that are as low.

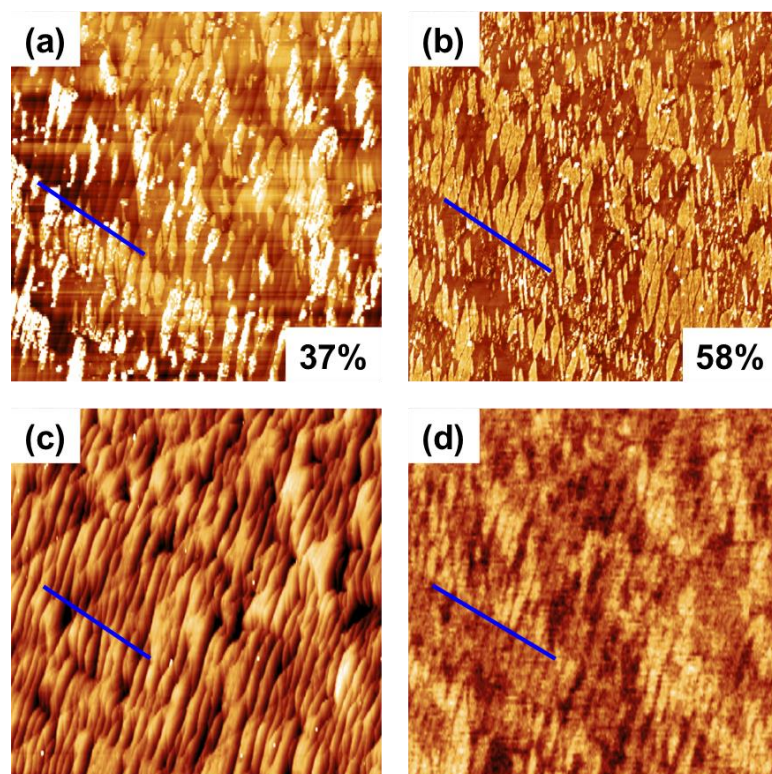


**Figure 6.10.** (a) Topographic AFM image after lead photooxidation, (b) topographic image after silver photoreduction recorded, (c) topographic image of the clean surface, and (d) surface potential image of the same area of the sample annealed at 1100 °C for 6 h with 0.02 g  $\text{Sr}_3\text{Ti}_2\text{O}_7$ . All images are  $10\ \mu\text{m} \times 10\ \mu\text{m}$ . The blue lines more the same position on each image. The vertical scale from dark-to-light is: (a) 0 – 6 nm, (b) 0 to 4 nm, (c) 0 – 2 nm and (d) 0 – 20 mV. The fractional coverage of photoanodic and photocathodic terraces in (a) and (b), respectively, are given in the lower right corners.

The experiments described above have shown that both higher annealing temperatures and heating in the presence of a  $\text{TiO}_2$  reservoir increases the fraction of the photoanodic surface. In an effort to create a completely photoanodic surface, a  $\text{SrTiO}_3$  sample was annealed with a 2.0 g reservoir of  $\text{TiO}_2$  for 6 h at 1100 °C. The image in Fig. 6.11(a) shows the surface after the photooxidation of lead and all of the terraces have lead deposits, indicating that the surface 100 % photoanodic. The image in Fig. 6.11(b) shows the surface after photoreducing silver. Silver is reduced only on the edges of the terraces, indicating that the terraces are inert for photoreduction, consistent with them being 100 % photoanodic.

Heating the in the presence of  $\text{Sr}_3\text{Ti}_2\text{O}_7$  powders was shown to increase the fraction of photocathodic surface area. In an attempt to make a 100 % photocathodic surface, a  $\text{SrTiO}_3$  sample was heated for 6 h at 1100 °C in a crucible containing 0.12 g of  $\text{Sr}_3\text{Ti}_2\text{O}_7$  powder. The surface topography after the photooxidation of lead is shown in Fig. 6.11(c). Only 2 % of the surface is covered by the lead containing deposits. As shown in Fig. 6.11(d), when the same surface is used to photoreduce silver, is almost completely covered by reduced silver. Therefore, the surface is 98 % photocathodic. Note that when  $\text{SrTiO}_3$  is heated in this condition, the surface does not develop terraces, as in the other experiments, but instead developed a microfaceted appearance.

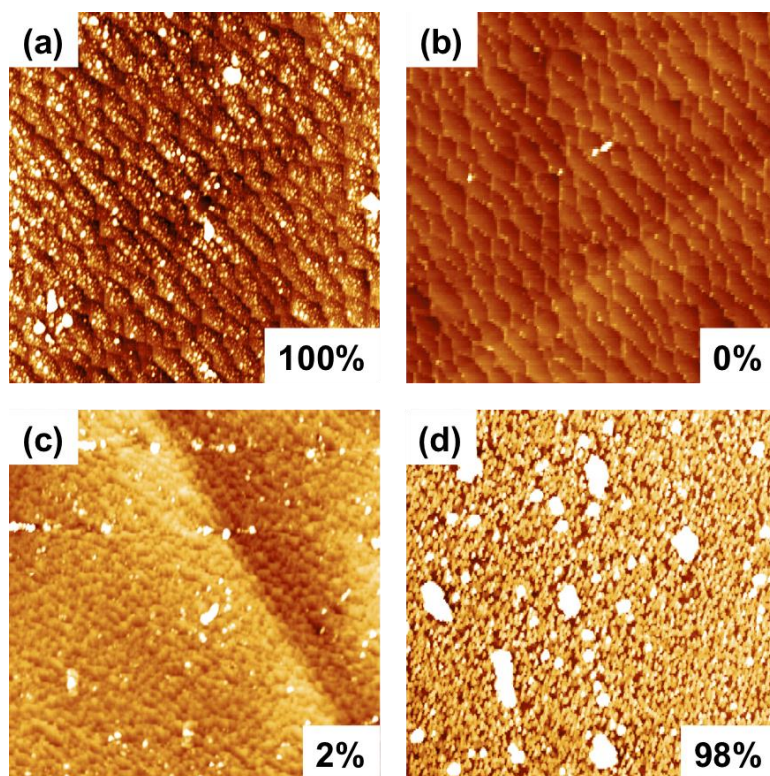


**Figure. 11.** Topographic AFM image of samples annealed with 2 g  $\text{TiO}_2$  powder (a) after lead photooxidation and (b) after silver photoreduction. Topographic AFM image of samples annealed with 0.12 g  $\text{Sr}_3\text{Ti}_2\text{O}_7$  powder (c) after lead photooxidation and (d) after silver photoreduction. Both samples were annealed at 1100 °C for 6 h. All images are  $5 \mu\text{m} \times 5 \mu\text{m}$  laterally and the dark-to-light vertical scales are (a) – (c) 0 – 5 nm (d) 0 – 10 nm. The fractional coverage of photoanodic (a & c) and photocathodic (b & d) terraces are given in the lower right corners.

The fractional coverage of photoanodic and photocathodic terraces versus the duration of the anneal, for different temperatures and conditions are summarized in Fig. 6.12. The temperature is given by the shape of the symbol and if there is a letter within the symbol, it indicates if  $\text{TiO}_2$  (T) or  $\text{Sr}_3\text{Ti}_2\text{O}_7$  (S) was present during the anneal. The points connected by the dashed lines were annealed at the same temperature and if you follow these lines, it is apparent that shorter annealing times lead to more photocathodic surfaces. It is also clear that lower annealing temperatures lead to more photocathodic terraces. The presence of  $\text{Sr}_3\text{Ti}_2\text{O}_7$  makes the surface more photocathodic and the presence of  $\text{TiO}_2$  make the surface more photoanodic.

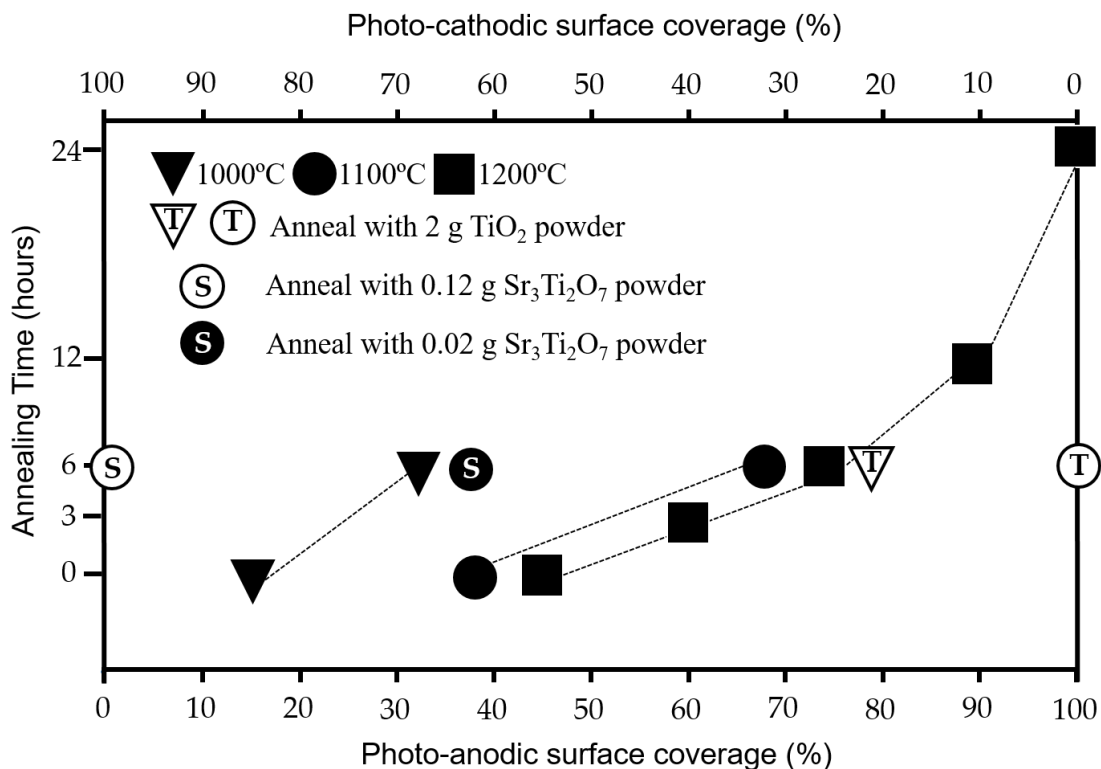


**Fig. 6.12.** The fractional coverage of photoanodic and photocathodic terraces versus the annealing time for samples shown in Figs. 2 through 11. The shape of symbols represents the annealing temperature.

## 6.4 Discussion

The experimental results show that SrTiO<sub>3</sub> (110) surfaces, when annealed at temperatures greater than or equal to 1000 °C in air have two types of terraces with distinct surface potentials. The terraces that have the higher (more positive) surface potential promote reduction and are referred to photocathodic terraces. The terraces that have the lower (more negative) surface potential promote oxidation and are referred to as photoanodic terraces. This is similar previously published observations on other surface surfaces, including polar terraces on SrTiO<sub>3</sub> (111),<sup>14</sup> polar domains on ferroelectric surfaces<sup>10</sup>, domains on ferroelastic surfaces<sup>12,34</sup>, thin films supported by ferroelectrics,<sup>13,35,36</sup> and hematite.<sup>37</sup> All of these cases have the same correlation between surface potential and photochemical reactivity; the area with a higher surface potential has reduced upward (or more downward) band bending at surface. As a result, photogenerated electrons have a smaller energy barrier to get to surface (or, in the case of downward band bending, are attracted to the surface) to participate in reduction reactions. On the other hand, areas with low surface potential have increased upward band bending. Upward band bending attracts holes to surface for oxidation reactions and repels electrons. This qualitative interpretation has been supported quantitatively by simulations of the photochemical reactivity thin TiO<sub>2</sub> supported by ferroelectric BaTiO<sub>3</sub>.<sup>38</sup>

As mentioned earlier, the SrTiO<sub>3</sub> (110) surface can be terminated by a SrTiO plane with a formal charge of 4<sup>+</sup> or by a 2O plane with a formal charge of 4<sup>-</sup> and the spacing between these two planes of opposite charge is 1.38 Å (defined as N). On the idealized bulk terminated surface illustrated in Fig. 6.1, odd-N should have different surface terminations and terraces separated by even-N should have the same surface termination. However, the SrTiO<sub>3</sub> (110) surface is known to reconstruct. For example, a series of (n x 1) reconstructions has been observed after annealing in ultra-high vacuum environment.<sup>39</sup> For samples annealed at 1 atm, (1 x 1) and (1 x 2)

reconstructions made up of  $\text{TiO}_2$  microfacet planes were found.<sup>22</sup> Other types of reconstructions have also been reported, depending on the annealing temperature, the time, and the environment.<sup>19, 20, 21, 24</sup> In each of these cases, the surface can be thought of as a network of corner- or edge-sharing  $\text{TiO}_x$  units with varying stoichiometries that depend on how much Sr was lost during the annealing process.<sup>23</sup> One aspect of these reconstructions that is important for the current work is that, independent of the reconstruction or the annealing environment, step heights measured between terraces of the same chemical composition are still even multiples of N.<sup>27, 28, 40</sup> Therefore, step height measurements can be used to determine if there is a change in the chemical composition of the terraces. In our experiment, it was determined that terraces separated by even-N have similar photochemical reactivity and surface potential while terraces separated by odd-N have different reactivity and surface potentials.

The potential difference between the two terraces originates from both surface charges and work function difference. It is assumed that the actual charges on the different terraces are reduced from the ideal +4 and -4 by reconstruction and adsorption. For example, for samples exposed to air and aqueous solutions, adsorption of hydroxyls is expected to alter the surface charge. The adsorption of water on  $(1 \times n)$  reconstructed  $\text{SrTiO}_3$  (110) surfaces has been studied and it was found that surfaces with highly oxidized Ti only weakly adsorb water.<sup>25, 26</sup> However, if there is reduced Ti on the surface, then water molecules are dissociated at oxygen vacancies and hydroxyl groups are strongly adsorbed to the surface. Calculations have also indicated that there should be work function differences between the ideal  $\text{SrTiO}$  and  $2\text{O}$  terraces, with the later having a work function that is 1 eV lower than the former.<sup>41</sup> Termination dependent work functions, charge, and adsorption probably all contribute to the difference in the measured potential and reactivity of the

two different terraces on SrTiO<sub>3</sub>, but at this point in time it is difficult to assign the relative importance of each factor.

The experiments show that higher annealing temperatures and longer annealing times cause an increase in the fraction of the surface that is photoanodic. As noted before, the vapor pressure of SrO<sub>x</sub> above SrTiO<sub>3</sub> is much larger than TiO<sub>x</sub>.<sup>42, 43, 44</sup> Therefore, longer and higher temperature annealing is likely to cause the evaporation of Sr and leave the surfaces Ti-rich. Therefore, according to the results in Fig. 6.12, the photoanodic terrace is most likely to be Ti-rich and the photocathodic terraces are likely to have more Sr. This is consistent with the observations on the clean surfaces; the photocathodic terraces are usually higher than the photoanodic terraces, as illustrated in Figs. 6.2(a), 6.5, 6.8 and 6.9(c), suggesting that these areas are left behind as layers of the surface are removed.

The experiments showed that when SrTiO<sub>3</sub> (110) single crystals were annealed with Sr-rich and Sr-poor powders, the surfaces could be tuned to more photoanodic and photocathodic extremes, respectively. The interaction of the SrTiO<sub>3</sub> (110) surface and the powder must occur through the vapor phase. Although the vapor pressure of TiO<sub>2</sub> powder at the annealing temperature is negligible ( $P_{\text{TiO}_x} \sim 10^{-10}$  torr at 2000 °C)<sup>45</sup>, the vapor pressure of SrO while heating SrTiO<sub>3</sub> is orders of magnitude higher ( $P_{\text{SrO}} > 2$  torr at 2000 °C)<sup>42, 43</sup>. Moreover, the presence of water vapor converts strontium oxide to a hydroxide that has a vapor pressure which is larger by many orders of magnitude.<sup>44</sup> Therefore, the most plausible mechanism is that the SrO evaporated from the SrTiO<sub>3</sub> surface reacts with the surrounding TiO<sub>2</sub> reservoir, encouraging further evaporation of Sr element and leaving behind a more Ti-rich photoanodic SrTiO<sub>3</sub> (110) surface. In earlier research, we studied SrTiO<sub>3</sub> (111) surfaces annealed in the same conditions used here. X-ray photoelectron spectroscopy showed that SrTiO<sub>3</sub> (111) surfaces annealed with TiO<sub>2</sub> powders contained more Ti

than the ones annealed without  $\text{TiO}_2$ , consistent with the proposed mechanism.<sup>14</sup> The same mechanism should be applicable to the  $\text{SrTiO}_3$  (110) surface.

For the case of heating in the presence of  $\text{Sr}_3\text{Ti}_2\text{O}_7$ , it is assumed that the Sr-rich phase acts as a source of SrO with a much greater surface area. Thus, there is a concentration gradient to transport SrO from the powder to the sample surface to compensate for any Sr evaporating from the crystal. In this way, the surface are tuned to be the more Sr-rich photocathodic surface. This is also consistent with a report of getting SrTiO or O single terminated  $\text{SrTiO}_3$  (110) surface (all covered in Ti-rich oxide clusters) by tuning Sr/Ti ratio at the surface using  $\text{Ar}^+$  sputtering then followed with ultra-high vacuum annealing. This treatment increased the surface Sr concentration, while it was still SrTiO terminated.<sup>24</sup> Our experiments of tuning the surface termination from nearly purely photocathodic to purely photoanodic by adding excess powders uses a similar concept, but the process can be carried out in air. Therefore, this is a straightforward and complementary method to vacuum annealing and solution chemical treatments developed for surface engineering thin film substrates.<sup>28, 46, 47, 48</sup>

Our earlier study of the  $\text{SrTiO}_3$  (111) surface showed that the Ti-rich termination that had a smaller potential was more reactive for photooxidation.<sup>14</sup> The same appears to be true for  $\text{SrTiO}_3$  (110). However, the surface coverage of photoanodic and photocathodic terraces of  $\text{SrTiO}_3$  (110) can be tuned over a much wider range than  $\text{SrTiO}_3$  (111). By varying temperature and time, or adding reservoirs of Ti-rich or Sr-rich powders, the surface can almost continuously changed from purely photoanodic to photocathodic. Therefore, it is possible to optimize the overall photochemical reactivity for the reaction of interest. For example, if the catalyst is designed to degrade organic compounds, a high percentage of photoanodic terraces might be the most efficient. For water splitting, the relative areas of the terraces should be adjust so that reduction and oxidation

half reactions occur at the same rate. On an n-type semiconductor such as SrTiO<sub>3</sub>, this is also likely to be a surface that favor the minority carrier (oxidation) reaction.

## 6.5 Conclusions

SrTiO<sub>3</sub> (110) surfaces annealed in air at temperatures between 1000 °C and 1200 °C exhibit two types of terraces with distinct surface potentials. The different types of terraces are separated by odd integer multiples of the interplanar spacing, corresponding to different chemical terminations of the bulk crystal. The terraces with the more positive (less positive) surface potential promote photoreduction (photooxidation) reactions as more electrons (holes) are attracted to surface. Therefore, the more positive terraces are photocathodic and the less positive terraces are photoanodic. The relative surface coverage of these two terraces, and the surface reactivity, can be controlled by the temperature and duration of annealing. The relative area of photoanodic (photocathodic) terraces can be controlled within the range of 100 % to 15 % (0 % to 85 %). Samples annealed at higher temperatures and for longer times have increasing photoanodic surface areas. It was also found that the surface termination could be controlled by annealing the crystals with Ti- or Sr-rich powders. Annealing with TiO<sub>2</sub> powder promotes photoanodic surfaces and annealing with Sr<sub>3</sub>Ti<sub>2</sub>O<sub>7</sub> powder promotes photocathodic surfaces. By using the Sr<sub>3</sub>Ti<sub>2</sub>O<sub>7</sub> powder, it was possible to create a surface that was 98 % photocathodic. These annealing treatments make it possible to adjust the SrTiO<sub>3</sub> surface from almost completely photocathodic to completely photoanodic.

## Reference

1. M. R. Hoffmann, S. T. Martin, W. Y. Choi, and D. W. Bahnemann, "Environmental applications of semiconductor photocatalysts," *Chem. Rev.*, 95[1] 69-96 (1995).
2. M. Kitano and M. Hara, "Heterogeneous photocatalytic cleavage of water," *J. Mater. Chem.*, 20[4] 627-41 (2010).
3. A. Kudo and Y. Miseki, "Heterogeneous photocatalyst materials for water splitting," *Chem. Soc. Rev.*, 38[1] 253-78 (2009).
4. F. E. Osterloh, "Inorganic nanostructures for photoelectrochemical and photocatalytic water splitting," *Chem. Soc. Rev.*, 42[6] 2294-320 (2013).
5. M. A. Fox and M. T. Dulay, "Heterogeneous Photocatalysis," *Chem. Rev.*, 93[1] 341-57 (1993).
6. L. Li, G. S. Rohrer, and P. A. Salvador, "Heterostructured Ceramic Powders for Photocatalytic Hydrogen Production: Nanostructured TiO<sub>2</sub> Shells Surrounding Microcrystalline (Ba,Sr)TiO<sub>3</sub> Cores," *J. Am. Ceram. Soc.*, 95[4] 1414-20 (2012).
7. X. Wang, Q. Xu, M. Li, S. Shen, X. Wang, Y. Wang, Z. Feng, J. Shi, H. Han, and C. Li, "Photocatalytic Overall Water Splitting Promoted by an alpha-beta phase Junction on Ga<sub>2</sub>O<sub>3</sub>," *Angewandte Chemie-International Edition*, 51[52] 13089-92 (2012).
8. R. Munprom, P. A. Salvador, and G. S. Rohrer, "Ferroelastic domains improve photochemical reactivity: a comparative study of monoclinic and tetragonal (Bi<sub>1-0.5x</sub>Na<sub>0.5x</sub>)(V<sub>1-x</sub>Mo<sub>x</sub>)O<sub>4</sub> ceramics," *J. Mater. Chem. A*, 4[8] 2951-59 (2016).
9. L. Li, P. A. Salvador, and G. S. Rohrer, "Photocatalysts with internal electric fields," *Nanoscale*, 6[1] 24-42 (2014).
10. J. L. Giocondi and G. S. Rohrer, "Spatial separation of photochemical oxidation and reduction reactions on the surface of ferroelectric BaTiO<sub>3</sub>," *J. Phys. Chem. B*, 105[35] 8275-77 (2001).
11. J. L. Giocondi and G. S. Rohrer, "Structure sensitivity of photochemical oxidation and reduction reactions on SrTiO<sub>3</sub> surfaces," *J. Am. Ceram. Soc.*, 86[7] 1182-89 (2003).
12. R. Munprom, P. A. Salvador, and G. S. Rohrer, "The orientation dependence of the photochemical reactivity of BiVO<sub>4</sub>," *J. Mater. Chem. A*, 3[5] 2370-77 (2015).
13. Y. L. Zhang, A. M. Schultz, P. A. Salvador, and G. S. Rohrer, "Spatially selective visible light photocatalytic activity of TiO<sub>2</sub>/BiFeO<sub>3</sub> heterostructures," *J. Mater. Chem.*, 21[12] 4168-74 (2011).
14. Y. Zhu, P. A. Salvador, and G. S. Rohrer, "Controlling the Relative Areas of PhotoCathodic and PhotoAnodic Terraces on the SrTiO<sub>3</sub> (111) Surface," *Chem. Mater.*, DOI: 10.1021/acs.chemmater.6b02205 in press (2016).
15. A. H. Kahn and L. A.J., "Electronic Energy Bands in Strontium Titanate," *Phys. Rev. A*, 135[5A] 1321-25 (1964).
16. K. van Benthem, C. Elsasser, and R. H. French, "Bulk electronic structure of SrTiO<sub>3</sub>: Experiment and theory," *J. Appl. Phys.*, 90[12] 6156-64 (2001).
17. J. M. Lehn, J. P. Sauvage, and R. Ziessel, "Photochemical water splitting continuous generation of hydrogen and oxygen by irradiation of aqueous suspensions of metal loaded strontium-titanate," *New J. Chem.*, 4[11] 623-27 (1980).
18. T. K. Townsend, N. D. Browning, and F. E. Osterloh, "Nanoscale Strontium Titanate Photocatalysts for Overall Water Splitting," *Acs Nano*, 6[8] 7420-26 (2012).
19. H. Bando, Y. Aiura, Y. Haruyama, T. Shimizu, and Y. Nishihara, "Structure and electronic states on reduced SrTiO<sub>3</sub>(110) surface observed by scanning tunneling-microscopy

- and spectroscopy," *J. Vac. Sci. Tech. B*, 13[3] 1150-54 (1995).
20. J. Brunen and J. Zegenhagen, "Investigation of the SrTiO<sub>3</sub> (110) surface by means of LEED, scanning tunneling microscopy and Auger spectroscopy," *Surf. Sci.*, 389[1-3] 349-65 (1997).
  21. N. Erdman and L. D. Marks, "SrTiO<sub>3</sub>(001) surface structures under oxidizing conditions," *Surf. Sci.*, 526[1-2] 107-14 (2003).
  22. A. Gunhold, K. Gomann, L. Beuermann, V. Kempter, G. Borchardt, and W. Maus-Friedrichs, "Changes in the surface topography and electronic structure of SrTiO<sub>3</sub>(110) single crystals heated under oxidizing and reducing conditions," *Surf. Sci.*, 566 105-10 (2004).
  23. D. M. Kienzle, "Surface Structures of the Metal-Oxide Materials Strontium Titanate and Lanthanum Aluminate." in. Northwestern University, 2013.
  24. Z. Wang, F. Yang, Z. Zhang, Y. Tang, J. Feng, K. Wu, Q. Guo, and J. Guo, "Evolution of the surface structures on SrTiO<sub>3</sub>(110) tuned by Ti or Sr concentration," *Phys. Rev. B*, 83[15] 155453 (2011).
  25. W. T. Li, S. M. Liu, S. Wang, Q. L. Guo, and J. D. Guo, "The Roles of Reduced Ti Cations and Oxygen Vacancies in Water Adsorption and Dissociation on SrTiO<sub>3</sub>(110)," *J. Phys. Chem. C*, 118[5] 2469-74 (2014).
  26. Z. M. Wang, X. F. Hao, S. Gerhold, Z. Novotny, C. Franchini, E. McDermott, K. Schulte, M. Schmid, and U. Diebold, "Water Adsorption at the Tetrahedral Titania Surface Layer of SrTiO<sub>3</sub>(110)-(4 x 1)," *J. Phys. Chem. C*, 117[49] 26060-69 (2013).
  27. Y. Mukunoki, N. Nakagawa, T. Susaki, and H. Y. Hwang, "Atomically flat (110) SrTiO<sub>3</sub> and heteroepitaxy," *Appl. Phys. Lett.*, 86[17] (2005).
  28. A. Biswas, P. B. Rossen, C. H. Yang, W. Siemons, M. H. Jung, I. K. Yang, R. Ramesh, and Y. H. Jeong, "Universal Ti-rich termination of atomically flat SrTiO<sub>3</sub> (001), (110), and (111) surfaces," *Appl. Phys. Lett.*, 98[5] 051904 (2011).
  29. J. B. Lowekamp, G. S. Rohrer, P. A. M. Hotsenpiller, J. D. Bolt, and W. E. Farneth, "Anisotropic photochemical reactivity of bulk TiO<sub>2</sub> crystals," *J. Phys. Chem. B*, 102[38] 7323-27 (1998).
  30. K. Tanaka, K. Harada, and S. Murata, "Photocatalytic deposition of metal-ions onto TiO<sub>2</sub> powder," *Sol. Energy*, 36[2] 159-61 (1986).
  31. J. Torres and S. Cerveramarch, "Kinetics of the photoassisted catalytic-oxidation of Pb(II) in TiO<sub>2</sub> suspensions," *Chem. Eng. Sci.*, 47[15-16] 3857-62 (1992).
  32. D. Necas and P. Klapetek, "Gwyddion: an open-source software for SPM data analysis," *Central European Journal of Physics*, 10[1] 181-88 (2012).
  33. H. N. McMurray and G. Williams, "Probe diameter and probe-specimen distance dependence in the lateral resolution of a scanning Kelvin probe," *Journal of Applied Physics*, 91[3] 1673-79 (2002).
  34. R. Munprom, P. A. Salvador, and G. S. Rohrer, "Polar Domains at the Surface of Centrosymmetric BiVO<sub>4</sub>," *Chem. Mater.*, 26[9] 2774-76 (2014).
  35. N. V. Burbure, P. A. Salvador, and G. S. Rohrer, "Photochemical Reactivity of Titania Films on BaTiO<sub>3</sub> Substrates: Influence of Titania Phase and Orientation," *Chem. Mater.*, 22[21] 5831-37 (2010).
  36. N. V. Burbure, P. A. Salvador, and G. S. Rohrer, "Photochemical Reactivity of Titania Films on BaTiO<sub>3</sub> Substrates: Origin of Spatial Selectivity," *Chem. Mater.*, 22[21] 5823-30 (2010).

37. Y. Zhu and A. M. R. Schultz, Gregory S. Salvador, Paul A., "The Orientation Dependence of the Photochemical Activity of  $\alpha$ -Fe<sub>2</sub>O<sub>3</sub>," *J. Am. Ceram. Soc.* (2016).
38. J. J. Glickstein, P. A. Salvador, and G. S. Rohrer, "Computational Model of Domain-Specific Reactivity on Coated Ferroelectric Photocatalysts," *Journal of Physical Chemistry C*, 120[23] 12673-84 (2016).
39. B. C. Russell and M. R. Castell, "Reconstructions on the polar SrTiO<sub>3</sub> (110) surface: Analysis using STM, LEED, and AES," *Phys. Rev. B*, 77[24] (2008).
40. R. Bachelet, F. Valle, I. C. Infante, F. Sanchez, and J. Fontcuberta, "Step formation, faceting, and bunching in atomically flat SrTiO<sub>3</sub> (110) surfaces," *Appl. Phys. Lett.*, 91[25] (2007).
41. A. Pojani, F. Finocchi, and C. Noguera, "Polarity on the SrTiO<sub>3</sub> (111) and (110) surfaces," *Surf. Sci.*, 442[2] 179-98 (1999).
42. C. Gugushev, D. Klimm, F. Langhans, Z. Galazka, D. Kok, U. Juda, and R. Uecker, "Top-seeded solution growth of SrTiO<sub>3</sub> crystals and phase diagram studies in the SrO-TiO<sub>2</sub> system," *Crystengcomm*, 16[9] 1735-40 (2014).
43. R. H. Lamoreaux, D. L. Hildenbrand, and L. Brewer, "High-temperature vaporization behavior of oxides 2. Oxides of Be, Mg, Ca, Sr, Ba, B, Al, Ga, In, Tl, Si, Ge, Sn, Pb, Zn, Cd, and Hg," *J. Phys. Chem. Ref. Data*, 16[3] 419-43 (1987).
44. T. Zhang and S. Wang, "Seals for Planar Solid Oxide Fuel Cells: The State of the Art," pp. 58. in *Nanostructured and Advanced Materials for Fuel Cells*. Edited by S. P. Jiang and P. K. Shen. CRC Press, Taylor Francis Group, Boca Raton, FL, 2008.
45. P. M. Martin, "Handbook of deposition technologies for films and coatings: science, applications and technology," pp. 196. William Andrew, (2009).
46. J. Chang, Y.-S. Park, and S.-K. Kim, "Atomically flat single-terminated SrTiO<sub>3</sub> (111) surface," *Appl. Phys. Lett.*, 92[15] 152910 (2008).
47. T. D. Doan, J. L. Giocondi, G. S. Rohrer, and P. A. Salvador, "Surface engineering along the close-packed direction of SrTiO<sub>3</sub>," *J. Cryst. Growth*, 225[2-4] 178-82 (2001).
48. W. M. Sigmund, M. Rotov, Q. D. Jiang, J. Brunen, J. Zegenhagen, and F. Aldinger, "A titanium-rich (111) surface of SrTiO<sub>3</sub> single crystals by thermal annealing," *Appl. Phys. A Mater. Sci. Process.*, 64[2] 219-20 (1997).

## Chapter 7 Buried Charge at the $\text{TiO}_2/\text{SrTiO}_3$ (111)

### Interface and its Effect on Photochemical Reactivity

*High temperature annealing in air is used to produce  $\text{SrTiO}_3$  (111) surfaces with two types of atomically flat terraces: those that promote photoanodic reactions and those that promote photocathodic reactions. Surface potential measurements show that the photocathodic terraces have a relatively more positive surface potential than the photoanodic terraces. After depositing thin titania ( $\text{TiO}_2$ ) films on the surface, from 0.9 nm to 16 nm thick, the surface of the film above the photocathodic terraces also has photocathodic properties, similar to those of the bare surface. While a more positive surface potential can be detected on the surface of the thinnest titania films (0.9 nm thick), it is undetectable for thicker films. The persistence of the localized photocathodic properties on the film surface, even in the absence of a measurable difference in local potential, indicates that the charge associated with specific terraces on the bare  $\text{SrTiO}_3$  (111) surface remains localized at the  $\text{TiO}_2/\text{SrTiO}_3$  interface and that the buried charge influences the motion of photogenerated carriers.*

## 7.1 Introduction

Studies of the polar surfaces such as ZnO (0001)<sup>1</sup> and GaN (0001)<sup>2</sup> have shown that the internal electric field that arises from the charge on the polar surface can separate photogenerated electron-hole pairs and increase the photochemical reactivity. SrTiO<sub>3</sub> is a well-known photocatalyst that can split water when illuminated by UV light<sup>3, 4, 5</sup> and several of the low index surfaces are polar. For example, the ideal unreconstructed (111) surface is polar and charged; it can be terminated by a Ti<sup>4+</sup> layer or by a SrO<sub>3</sub><sup>4-</sup> layer. While the real SrTiO<sub>3</sub> (111) surface in air is likely to be reconstructed<sup>6, 7, 8</sup> and covered by a layer of adsorbates,<sup>9, 10</sup> it has recently been shown that some (111) terraces have locally photocathodic properties and the others have photoanodic properties.<sup>11</sup> Furthermore, the photocathodic terraces have a relatively positive potential compared the photoanodic terraces, as measured by Kelvin probe force microscopy (KFM).<sup>12</sup> The interpretation of these observations was that the terraces with a more positive potential (photocathodic) have reduced upward band bending at the surface and it is easier for photogenerated electrons to reach the surface and participate in photoreduction reactions. The photoanodic terraces, with a less positive surface potential, have increased upward band bending that prevents electrons from getting to the surface while holes are driven to the surface to participate in oxidation reactions. In other words, the polar terraces on the SrTiO<sub>3</sub> (111) have distinct photocathodic or photoanodic properties and, therefore, strongly influence photochemical reactions.

While polar surfaces might provide a mechanism to increase photochemical reactivity, their stability with respect to faceting and other types of reconstruction is questionable.<sup>13, 14</sup> One strategy for stabilizing polar surfaces is to add a thin protective coating that protects the polar surface.<sup>15, 16, 17</sup> Earlier studies of ferroelectrics coated by titania have illustrated that the reactivity

of the film surface is spatially selective and mimics the reactivity of the underlying polar substrate.<sup>15, 17</sup> The proposed mechanism is essentially the same as for the bare ferroelectric surface;<sup>18</sup> the substrate surfaces with positively charged domains have reduced upward band bending and the substrate surfaces with negatively charged domains have increased upward band bending. Electrons and holes that migrate to positive and negative domains, respectively, can then pass through the relatively thin titania coating and react with species at the surface. Recent simulations of photogenerated charge carrier transport in coated ferroelectrics provided quantitative support for this mechanism.<sup>19</sup>

Considering the similarities between charged ferroelectric domains and polar surface terminations, we can hypothesize that a thin coating on a polar SrTiO<sub>3</sub> surface will have photocathodic and photoanodic regions that mimic the properties of the underlying substrate. The main point of this paper is to describe findings that support this hypothesis. For the coating, we use titania. Titania has been used to coat ferroelectrics and SrTiO<sub>3</sub> in the past,<sup>15, 20</sup> it is a stable photocatalyst,<sup>21, 22</sup> and the TiO<sub>2</sub>/SrTiO<sub>3</sub> heterostructure has been shown to be photocatalytically active.<sup>23</sup> SrTiO<sub>3</sub> (111) surfaces have been prepared by high temperature annealing and the photocathodic regions have been identified using both surface potential imaging by KFM and the photochemical reduction of silver. After growing thin titania films, the same areas were analyzed and the results show that the charge on the terraces of the bare SrTiO<sub>3</sub> surface remain at the buried interface and influence the transport of photogenerated charge carriers.

## 7.2 Experimental Procedure

Commercially available SrTiO<sub>3</sub> (111) single crystals (MTI company, (111) +/- 0.5°, roughness < 5 Å) were heated in air at 5 °C/min to 1250 °C and held for 10 h. After annealing, the topography and surface potential distribution were imaged using a scanning probe microscope (Solver-Next, NT-MDT, Russia). A silicon probe (Tap300-G, budget sensor) was used to record topographic images and a conductive PtCr coated probe (190E-G, budget sensor) was used to record surface potential (also referred to as KFM) images. The image data was processed using the Gwyddion<sup>24</sup> software package.

The photocathodic areas of the surface were identified by photochemically reducing Ag<sup>+</sup> from solution.<sup>11, 18, 25, 26</sup> The reduced silver is insoluble and forms metallic deposits on the surface that can be imaged by AFM.<sup>27</sup> A 300 W mercury lamp (Newport, Irvine, CA) was used for illumination and the reaction time was 8 s. During this procedure, skin and eyes must be protected to prevent damage by UV radiation. After illumination, the sample was rinsed with de-ionized water and dried using a stream of 99.995 % nitrogen gas. After imaging the pattern of silver on the surface, the silver was removed by wiping the surface with a cotton swab and then sonicating the sample in a bath of methanol for 10 min. After the surface was cleaned, it was imaged by AFM again to make sure there was no detectable silver residue.

Atomically flat TiO<sub>2</sub> thin films were grown on the clean SrTiO<sub>3</sub> (111) surface using pulsed laser deposition (PLD) (Neocera, MD) with a KrF ( $\lambda = 248$  nm) laser (Coherent, CA). The film was deposited at 700 °C with an oxygen pressure of 30 to 40 mTorr. These conditions were adopted, with minor adjustments, from previous work in which TiO<sub>2</sub> films were grown on BiFeO<sub>3</sub> and BaTiO<sub>3</sub> substrates.<sup>15, 17, 28</sup> Note that to make the film atomically flat, we used a reduced laser pulse frequency (3 Hz) and a reduced laser energy (estimated to be 0.6 J/cm<sup>2</sup> at the target). After

deposition, the film thickness was measured using X-ray reflectivity. Films thicker than 5 nm can be measured directly, and the thicknesses of thinner films were estimated from the number of pulses used during the deposition (calibrated from the measurements on the thicker films). The film growth rate at this condition is around 1 nm per 1400 pulses. The phase of the film was examined by X-ray diffraction. A Philip X'Pert Pro MRD system was used for the diffraction measurements. The Cu anode X-ray source was operated at 40 kV and 45 mA to generate an X-ray beam with a wavelength of 0.154 nm ( $\text{Cu-K}_{\alpha 1}/\text{K}_{\alpha 2}$ ). Electron backscatter diffraction patterns of the heterostructure were captured using a Quanta 200 SEM (FEI, Hillsboro, OR) and analyzed using commercial software (TSL, EDAX, Mahwah, NJ) to check the film's crystallinity and orientation.

The film surfaces were used to reduce silver under the same conditions as the bare substrates. Topographic atomic force microscopy (AFM) images were recorded of the same areas before and after depositing the film so that the patterns of silver reduced on the film could be compared to those on the bare substrate. KFM was also used to map the surface potential distribution in the same areas before and after film growth.

### 7.3 Results

The topography of the  $\text{SrTiO}_3$  (111) surface after annealing at 1250 °C in air is shown in Fig. 7.1(a). The surface is characterized by a set of atomically flat terraces separated by approximately parallel steps 1 to 2 nm in height. The surface potential distribution in the same area is shown in Fig. 7.1(b). The surface potential image indicates that the terraces have two distinct contrast levels and the potential difference between the two varies in the range of 7-15

mV. After the sample was illuminated by UV light in a silver nitrate solution, metallic silver selectively deposited on some of the terraces and appears as white contrast in Fig. 7.1(c). After comparing the locations of the silver to the potential distribution in the KFM image (Fig. 7.1(b)), it is clear the Ag deposits preferentially on the set of terrace that have the relatively greater (more positive) surface potential. These observation are consistent with those we have recently reported and we refer to the terraces that reduce silver as photocathodic terraces.<sup>12</sup>

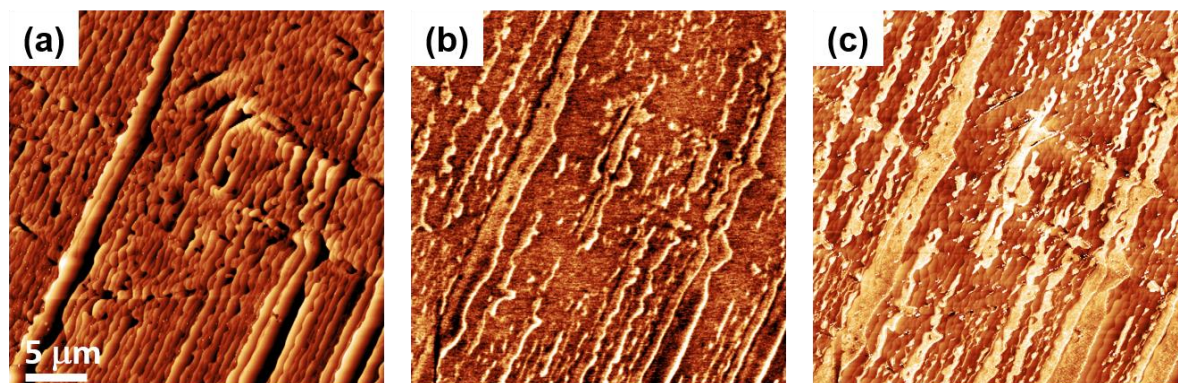


**Figure 7.1.** (a) Topographic AFM image of the clean SrTiO<sub>3</sub> (111) surface. (b) Surface potential image of the same area. (c) Topographic image of the same area after it was used to photochemically reduce Ag<sup>+</sup>. All images are 30 μm × 30 μm. The contrast range from black-to-white is: (a) 0 – 3 nm, (b) -25 – 0 mV, and (c) 0 – 10 nm.

After the experiment depicted in Fig. 7.1, the reduced silver was removed from the surface and TiO<sub>2</sub> films were deposited. A pair of typical topographic AFM images, of the same area, before and after depositing a 2.2 nm thick titania film, are shown in Fig. 7.2. Note that there are high spots (white contrast) in the images that are thought to be surface contamination from handling. These spots serve as useful fiducial markers for locating the same area; four of the spots are marked with a blue dot to identify the same location in the two images. The steps on this part of the surface are 1 to 2 nm in height and the roughness of the terraces is about 1.0 Å. After depositing the TiO<sub>2</sub> film, the roughness of the same area increased to 2.1 Å. Despite the modest

increase in roughness, the shapes of the step edges and terraces are unchanged and this makes it possible to verify that the images are recorded at the same location.

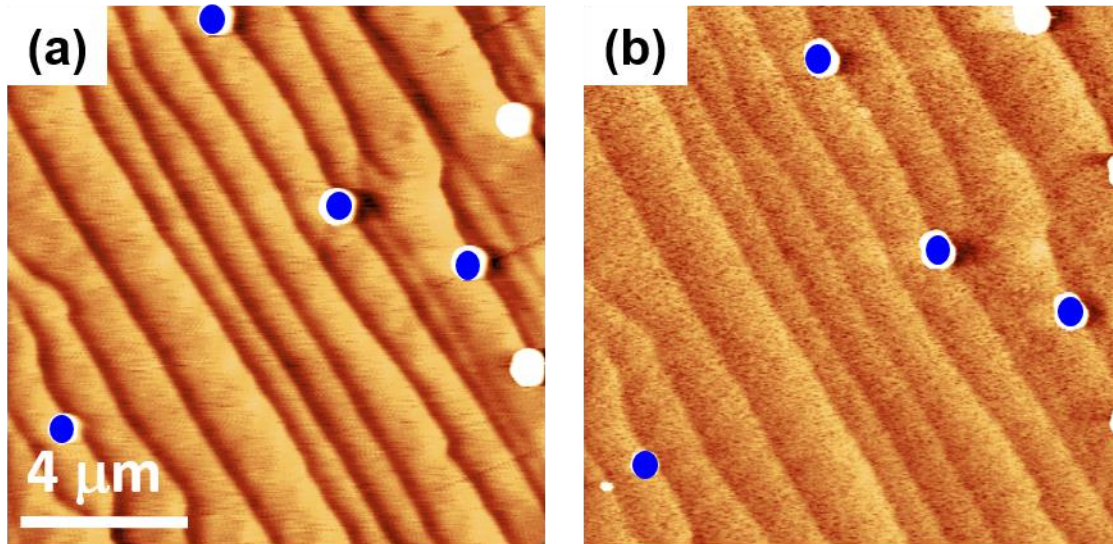


**Figure 7.2.** Topographic AFM images (semi-contact mode) of (a) the bare SrTiO<sub>3</sub> (111) surface after annealing and (b) the same area after depositing a 2.2 nm thick TiO<sub>2</sub> film. In each image, the field of view is 13 μm × 13 μm. For both images, the vertical range from black-to-white is 0 – 5 nm.

X-ray diffraction was used to characterize the bare annealed SrTiO<sub>3</sub> (111) substrate and the 50 nm TiO<sub>2</sub>/SrTiO<sub>3</sub> heterostructure. The diffraction patterns from the bare substrate and the heterostructures are shown in Fig. 7.3(a) and it is clear that a new peak has appeared after deposition of the 50 nm film. The position the SrTiO<sub>3</sub> (111) peak is 40.081°, 0.082° from the ideal peak position (39.999 °).<sup>29</sup> The new peak that appears after the film is deposited is located at 37.812°. Assuming that the measured position of the new peak is shifted by the same offset as the SrTiO<sub>3</sub> (111) peak, its true position is 37.730°. We assign this new peak to anatase (004) because it differs from the ideal position by only 0.028 °.<sup>30</sup> It has been reported that TiO<sub>2</sub> films grown on SrTiO<sub>3</sub> (111) can have mixed phases and orientations: in addition to (001) anatase, (112) anatase and (100) rutile are also observed.<sup>31</sup> However, the (112) anatase diffraction peak

(38.600 °) and the rutile (200) peak (39.195 °) coincide with the SrTiO<sub>3</sub> (111) substrate peak, so the X-ray diffraction data was not sufficient to determine if these other orientations occurred in our films.

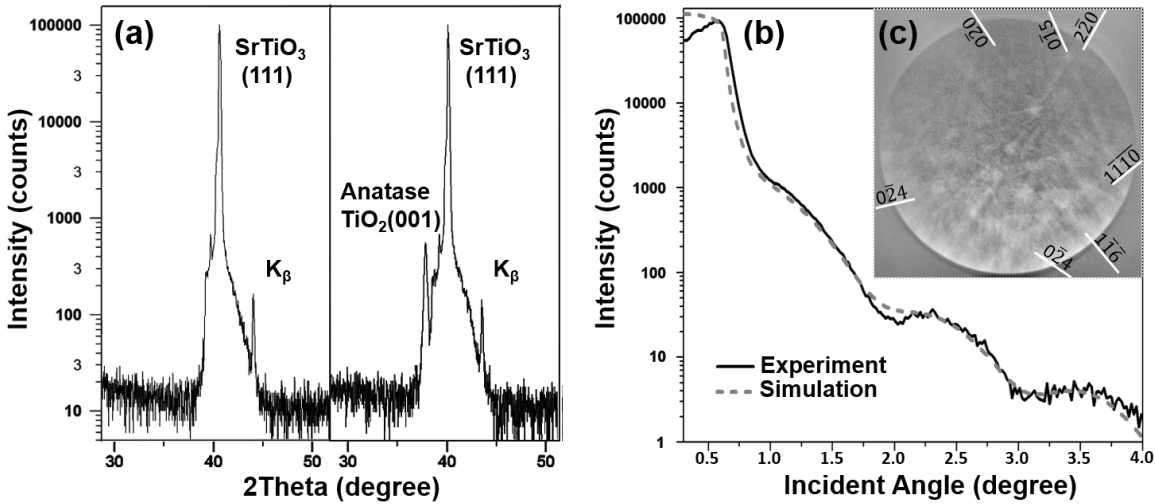


**Figure 7.3.** (a) XRD patterns of the bare SrTiO<sub>3</sub> (111) substrate (left panel) and the TiO<sub>2</sub>/SrTiO<sub>3</sub> heterostructure (right panel). The film thickness is about 50 nm. (b) Example of an X-ray reflectivity curve measured on a TiO<sub>2</sub> film/SrTiO<sub>3</sub> (111) single crystal heterostructure. The roughness of film is 3.5 Å, the roughness of the substrate is 0.5 Å and the measured film thickness is 7.2 nm. (c) Electron backscatter diffraction pattern from TiO<sub>2</sub>/SrTiO<sub>3</sub> heterostructure (thickness > 50 nm).

An electron backscatter diffraction pattern of the heterostructure is shown in Fig. 7.3(c). The diffraction pattern shows some clear bands, but is relatively weak, indicating poor crystallinity. While the pattern could not be indexed to a single phase, some bands (labeled in Fig. 7.3(c)) were consistent with the anatase (001) orientation. We did not succeed in indexing the other bands in the pattern, but it is clearly the result of a mixture of orientations or phases. Because the film is relatively thick (> 50 nm) it is unlikely that any of the band contrast arises from the substrate. We assume that the poor epitaxy of the film results from specifics of the deposition conditions, possibly from the low laser energy in combination with the temperature, pressure, and

geometry. We targeted conditions to yield smooth films and the results indicate that, in addition to films that are kinetically flat (low relative adatom mobility), they also have poor epitaxial quality. The crystalline, but not epitaxial films, are characteristic of what would be expected in a real catalyst.

An example of one of the X-ray reflectivity patterns used to measure the film thickness is shown in Fig. 7.3(b). The film thickness is directly proportional to the spacing between local maxima and this sample is estimated to be 7.2 nm thick (using simulation software X'Pert Reflectivity).<sup>32</sup> Note that the maximum incident angle range in the measurement is  $4^\circ$ ; beyond  $4^\circ$  the intensity signal is less than the noise. Therefore, the thinnest films that the X-ray reflectivity technique can characterize are around 5 nm, which will only show two maxima in the reflection intensity. The thicknesses of films thinner than 5 nm were estimated according to the film growth rate established from measurements of thicker films.

A series of films with thicknesses ranging from 0.9 nm to 16 nm was deposited. The pattern of silver particles after the photoreduction of silver was recorded on each sample, at the same area, before and after depositing the titania film. KFM images were also recorded to determine if the surface potential of the underlying SrTiO<sub>3</sub> (111) terraces influences the local potential at the surface of the TiO<sub>2</sub> film. The distribution of silver on the substrate, the surface potential distribution on the film surface, and the distribution of reduced silver on the film surface for the 0.9 and 2.2 nm thick films are compared in Fig. 7.4, where (a) to (c) show the distributions on the 0.9 nm thick film and (d) to (f) show the distributions for the 2.2 nm thick film. The images in Fig. 7.4(a) to (c) clearly show a correlation between the location of the silver on the bare substrate, the measured surface potential on the film, and the distribution of silver on the film surface. In other words, photocathodic terraces on the substrate that reduce silver also are also photocathodic

on the film surface. In addition, the surface potential of the 0.9 nm thick film surface is relatively more positive at the locations where the silver deposits. However, the measured potential difference (4 to 10 mV) is slightly less than on the substrate (7 to 15 mV). It should also be noted that silver appears to deposit almost everywhere on the film surface in (c), but significantly more deposits are observed on the terraces with a higher potential.

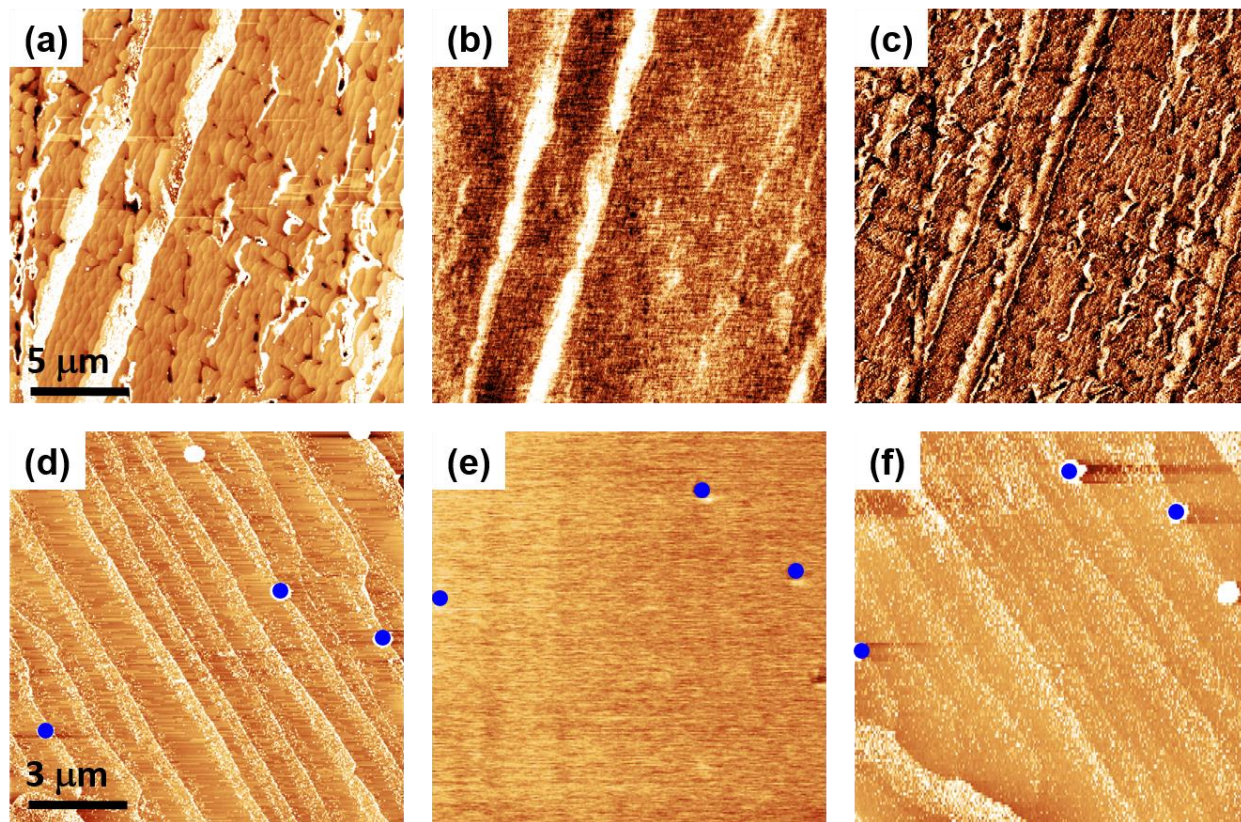


**Figure 7.4.** (a) and (d): AFM topographic images of bare SrTiO<sub>3</sub> (111) substrates after silver-reduction reactions. (b) and (e): Surface potential images measured in the same areas as (a) and (d), respectively, after deposition of a 0.9 (b) and 2.2 (e) nm titania film. (c) and (f): AFM topographic images of the two heterostructures from (b) and (e), respectively, after the silver-reduction reaction. The images (a), (b), and (c) are 20 μm × 20 μm. The images (d), (e), and (f) are 11 μm × 11 μm. In (d-f), blue dots are used to mark the same three places on the surface. Vertical scales from black-to-white are: (a), (d), and (f), 0 – 10 nm; (b) and (e) -10 – 10 mV; (c) 0 – 5 nm.

The corresponding images of the sample with the 2.2 nm titania film are shown in Fig. 7.4(d), (e), and (f). The KFM image (Fig. 7.4(d)) did not show a significant contrast difference

between the reactive and unreactive terraces; this was also true for all thicker films. This indicates that the charge associated with the terraces on the substrate has either been removed by the film growth or is screened by the film and undetectable at the surface. Even though no potential variations can be measured on the film surface, the pattern of silver reduced on the film surface (Fig. 7.4(f)) still mimics the pattern of reduced silver on the substrate (Fig. 7.4(d)). This result indicates that the charge remains on the terraces and still influences the motion of photogenerated carriers, but that it is sufficiently screened by the film so that it cannot be detected by KFM.

Experiments parallel to those described above were repeated for samples with thicker titania films and the results are shown in Fig. 7.5. The patterns of silver reduced on the bare surfaces of two SrTiO<sub>3</sub> (111) substrates are shown in Figs. 7.5(a) and (c). The same areas are shown after the deposition of 7.2 nm (Fig. 7.5(b)) and 16 nm (Fig. 7.5(d)) thick titania films and the reduction of silver. The result is similar to what was observed for the thinner films, with the pattern of silver on the film surface mimicking what was observed on the substrate surface before film deposition. A detailed comparison shows that films supported by reactive terraces are more reactive than the rest of the surface and films supported by unreactive terraces have some reduced silver, but much less than in the areas above the reactive terraces.

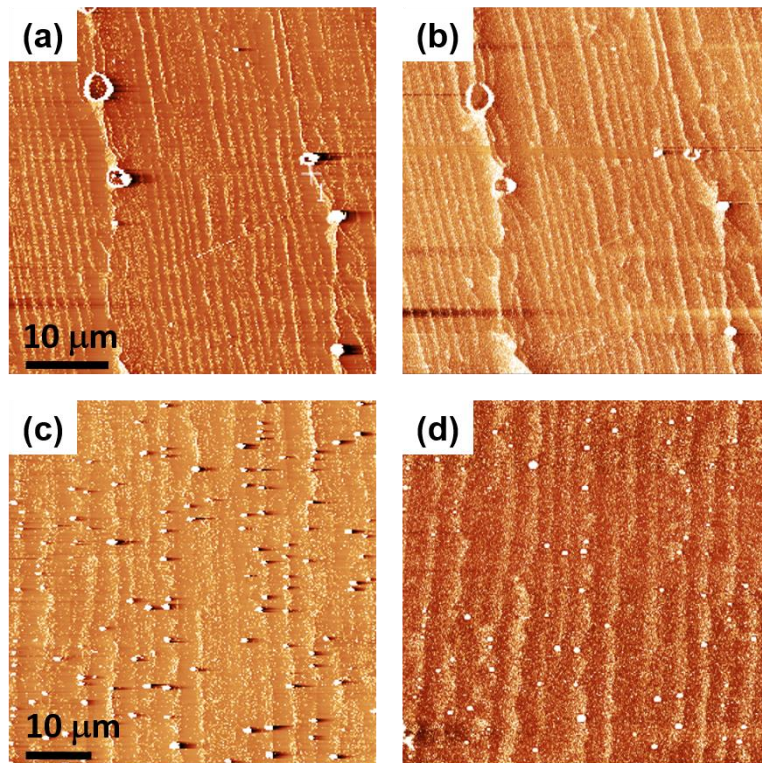


**Figure 7.5.** Topographic AFM images of the same areas of the substrate ((a) & (c)) and film surfaces ((b) & (d)), after the photoreduction of silver, for two different film thicknesses. In (b), the film is 7.2 nm thick and in (d) the film is 16 nm thick. The fields of view in (a) and (b) are  $40 \mu\text{m} \times 40 \mu\text{m}$ . The fields of view in (c) and (d) are  $50 \mu\text{m} \times 50 \mu\text{m}$ . The vertical scales from black-to-white are 0 – 20 nm.

#### 7.4 Discussion

The observations in the previous section show that titania films (up to 16 nm in thickness) supported on  $\text{SrTiO}_3$  (111) surfaces (which were annealed in air at  $1250 \text{ }^\circ\text{C}$  for 10 h prior to growth) have roughly the same spatially selective reactivity as the bare substrates. For the thinnest film, the relative potential difference between the two terraces is also similar to the potential difference on the bare substrate. These observations indicate that the charge on the terraces of the

bare substrate is trapped at the buried substrate-film interface and that the buried charge influences the transport of photogenerated electrons and holes.

To understand the mechanism of this phenomenon, we begin by considering where the photoelectrons are generated. SrTiO<sub>3</sub> and TiO<sub>2</sub> are both able to reduce Ag when stimulated by UV irradiation,<sup>11, 25</sup> but in this experiment, the titania film is too thin to adsorb enough light to produce significant concentrations of electron-hole pairs. Because the light used in this experiment has an absorption depth in SrTiO<sub>3</sub> and TiO<sub>2</sub> on the order of 10<sup>2</sup> nm,<sup>33, 34, 35</sup> the majority of light was adsorbed in the substrate; most of the electrons participating in the silver-reduction reaction must also have been generated in the SrTiO<sub>3</sub> substrate. Second, the diffusion length of electrons in TiO<sub>2</sub> is on the order of 100 nm to 10 μm.<sup>36</sup> Because the titania films were all less than 20 nm thick, the photoelectrons from the substrate can easily get to the film surface by diffusion. Third, the KFM images measured on the ultra-thin film sample show that after we deposit a TiO<sub>2</sub> film on the annealed SrTiO<sub>3</sub> (111) substrate, there is still a correlation between surface potential and reactivity, similar to the surface potential and reactivity correlation for bare SrTiO<sub>3</sub> (111) substrate. This suggests that the potential difference on the film surface originates from the potential differences of the photocathodic and photoanodic terraces on the buried SrTiO<sub>3</sub> (111) surface. Taken together, these considerations indicate that carriers photogenerated in the substrate experience a field from the buried interface charge that attracts different amounts of electrons and holes to the interface, depending on the buried local terrace charge, and some of these carriers traverse the film and react at the TiO<sub>2</sub> surface.

The surface potential value measured by KFM is proportional the contact potential difference ( $E_{CPD}$ ) between probe and sample surface.<sup>37, 38</sup> Possible energy level diagrams for the bare SrTiO<sub>3</sub> (111) substrate and SrTiO<sub>3</sub> (111)/TiO<sub>2</sub> heterostructures are depicted in Fig. 7.6. The

photoanodic terraces on the SrTiO<sub>3</sub> (111) surface that have lower measured surface potentials have a smaller value of  $E_{CPD}$  and the bands are bent upward at the surface, as shown in Fig. 7.6(a). Therefore, for the films supported on the photoanodic terraces, electrons are repelled from the interface and directed to the interior of sample, where they recombine with holes. On the other hand, for the photocathodic terraces that have higher measured surface potentials, the value of  $E_{CPD}$  is larger and the bands are not bent upwards as far as they are on the photoanodic terraces, as illustrated in Fig. 7.6(d). Therefore, photoelectrons are more easily transported to the film surface to reduce silver ions from solution. We should mention that it is also possible the bands at the photocathodic are flat, or even have a small downward band bending, but evidence from Pb<sup>2+</sup> oxidation experiments suggest a small amount of upward band bending.<sup>12</sup> For the very thin (0.9 nm) titania film, we assume that the film is not thick enough to fully screen the charge and the bands do not relax to their equilibrium positions (see Figs. 7.6(b) and 7.6(e)). This leads to values of  $E_{CPD}$  that differ on the photoanodic and photocathodic terraces, but not by as much as on the bare substrate and this is consistent with the observations. For the thicker films, depicted in Figs. 7.6(c) and 7.6(f), the buried charge is fully screened and the bands return to their equilibrium positions. In this case,  $E_{CPD}$  at the film surface is not measurably different at the two types of terraces. However, the energy barrier at the buried interface is very different for the two terraces. There is a much smaller barrier at the interface for the photocathodic terraces, making it easier for electrons to be transmitted from the substrate to the film surface. It is this difference in the energy barrier, resulting from the buried charge, that leads to the spatially selective reactivity of the film.

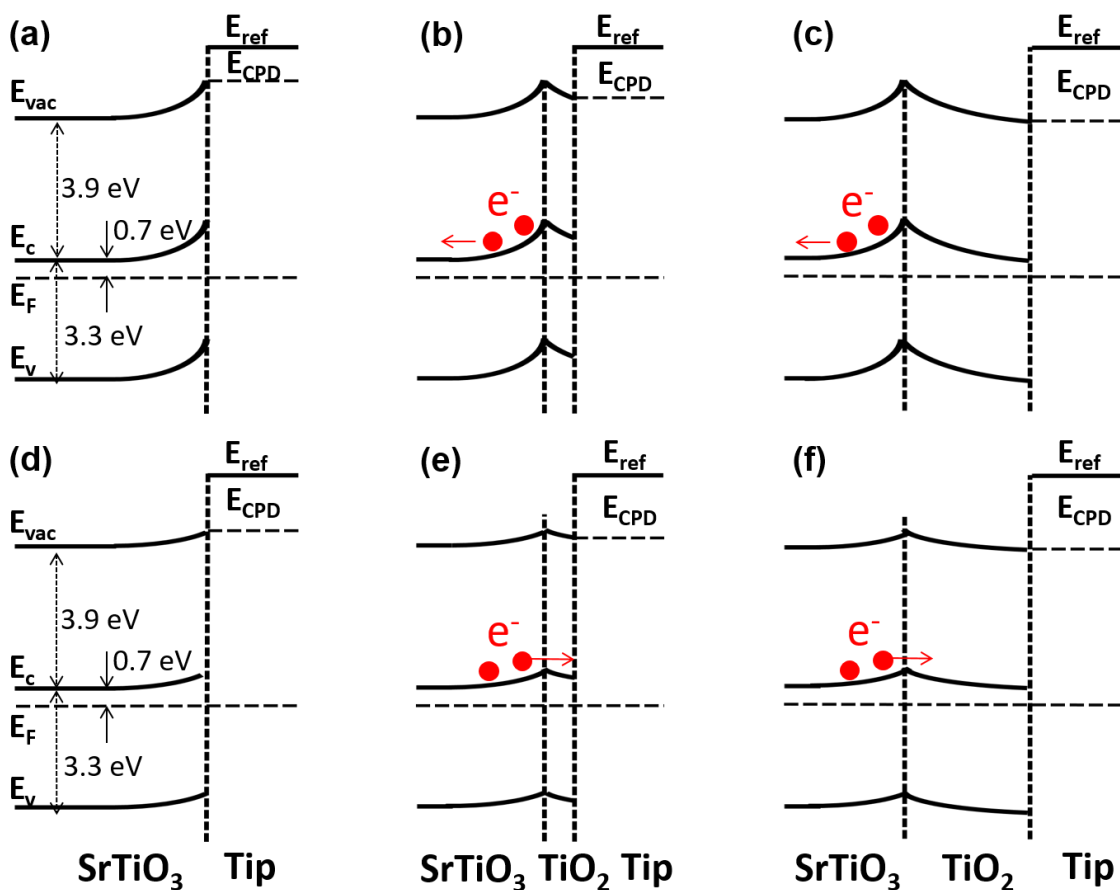


**Figure 7.6.** Schematic energy level diagrams of SrTiO<sub>3</sub> (111) and SrTiO<sub>3</sub> (111)/TiO<sub>2</sub> heterostructures and a conductive AFM tip. In each, the Fermi levels ( $E_F$ ) are aligned and the reference level ( $E_{Ref}$ ) discontinuities represent the contact potential difference ( $E_{CPD}$ ) measured by KFM. The energy levels are shown for the low surface potential terraces (a), the ultra-thin film supported on it (b), and a thicker film supported on it (c). The same cases are depicted for the high surface potential, photocathodic terraces in (d)-(f). The band bending in cases (a) through (c) prevents electrons from reaching the surface; the reduced barrier at the photocathodic terraces in (d) to (f) makes it possible for electrons to reach the interface with the solution.

The observation that the spatially selective photochemical reactivity of the substrate can be transferred to a film that normally exhibits spatially uniform reactivity is not completely new. The same phenomenon was observed in TiO<sub>2</sub>/BaTiO<sub>3</sub> and TiO<sub>2</sub>/BiFeO<sub>3</sub> heterostructures.<sup>15, 17, 39</sup> What is new about the current observations is that, while both BaTiO<sub>3</sub> and BiFeO<sub>3</sub> are ferroelectric, SrTiO<sub>3</sub> is not. For the cases of BaTiO<sub>3</sub> and BiFeO<sub>3</sub>, ferroelectric domains in the bulk with a

positive out-of-plane polarization at the surface are photocathodic, while domains with a negative surface polarization are photoanodic.<sup>18</sup> Therefore, the patterns of reduced silver on BaTiO<sub>3</sub> and BiFeO<sub>3</sub> are correlated with the domain structure. Burbure et al.<sup>15</sup> and Zhang et al.<sup>17</sup> found that thin TiO<sub>2</sub> films supported on BaTiO<sub>3</sub> or BiFeO<sub>2</sub> substrates photoreduce silver in spatially selective patterns; the patterns of the silver were correlated with the substrate domain structure. The phenomenon is similar for the TiO<sub>2</sub>/SrTiO<sub>3</sub> heterostructure, except that because SrTiO<sub>3</sub> is not ferroelectric, we assert that it is the differences in the potentials of the polar surface terminations on different buried terraces that influences the motion of photogenerated carriers.

It should be noted that earlier studies showed that TiO<sub>2</sub>/SrTiO<sub>3</sub> composites enhanced the UV light photocatalytic activity compared the separated phases.<sup>20, 23</sup> In the TiO<sub>2</sub>/SrTiO<sub>3</sub> heterostructures described here, we also observed slightly enhanced photoreactivity for the reduction of silver. Films supported on originally unreactive SrTiO<sub>3</sub> terraces (photoanodic) reduced some silver, while films supported on photocathodic SrTiO<sub>3</sub> terraces were just as reactive as the bare surface. This is understandable because TiO<sub>2</sub> is a good photocatalyst when activated by UV light. Although the film is thin, it still absorbs some light and produces photocarriers to participate in the reaction. Second, the electronic structure of the heterostructure can promote the separation of photogenerated charge carriers. Because both the conduction band and valence band of SrTiO<sub>3</sub> are at higher energies than the comparable bands in TiO<sub>2</sub>,<sup>40, 41, 42</sup> photogenerated electrons in SrTiO<sub>3</sub> can reduce their energy by moving to the conduction band of TiO<sub>2</sub> and ultimately to the surface to reduce Ag<sup>+</sup> from solution.

The findings reported here might ultimately have an important impact on the design of photocatalysts. The idea of using fixed charges on catalyst surfaces to separate photogenerated carriers, ameliorate recombination, and increase reaction efficiencies is well established.<sup>43, 44, 45, 46,</sup>

<sup>47</sup> By burying these charges at an internal interface covered by titania, the catalyst will be stable in an aqueous environment and the charges will be protected from degradation. While this has been demonstrated before for titania coated ferroelectrics,<sup>15, 17, 20</sup> SrTiO<sub>3</sub> offers a significant possible advantage compared to ferroelectrics because the ratio of photocathodic to photoanodic surface area can be controlled.<sup>12</sup> The relative areas of the polar domains on the surface of a ferroelectric are nearly equal. The best ratio for the areas of the photocathodic and photoanodic surfaces is the one that maximizes the reaction rate. This is presumably the inverse of the ratio of the rates of the cathodic and anodic half reactions and this is unlikely to be unity. While the ratios of opposite domains can be controlled in bulk ferroelectrics by poling, it is not clear how this could be accomplished with a powdered catalyst. However, we have recently shown that the ratio of photocathodic and photoanodic surface area on the SrTiO<sub>3</sub> (111) surface can be controlled by high temperature thermal treatments.<sup>12</sup> Therefore, it is possible, at least in principle, to create catalysts with controlled distributions of surfaces promoting photocathodic or photoanodic reactions and to protect these surfaces with a thin titania layer while preserving the positive benefits that result from the separation of charge carriers.

## 7.5 Conclusion

When silver is photochemically reduced on titania films supported by SrTiO<sub>3</sub> (111) substrates, the pattern of silver on the film surface mimics the pattern that is reduced on the substrate surface, before the film is deposited. Silver is preferentially reduced above terraces that have a more positive surface potential than the unreactive terraces. These observations indicate that the charges on different terraces on the SrTiO<sub>3</sub> (111) surface remain at the buried interface

after film growth. At the interface, they influence the transport of charge carriers to the surface such that silver is reduced on the film above the photocathodic terraces on the substrate.

## Reference

1. J. Yang, J. Wang, X. Li, J. Lang, F. Liu, L. Yang, H. Zhai, M. Gao, and X. Zhao, "Effect of polar and non-polar surfaces of ZnO nanostructures on photocatalytic properties," *J. Alloys Compd.*, 528 28-33 (2012).
2. H. Bae, E. Kim, J.-B. Park, S.-J. Kang, K. Fujii, S. H. Lee, H.-J. Lee, and J.-S. Ha, "Effect of Polarity on Photoelectrochemical Properties of Polar and Semipolar GaN Photoanode," *J. Electrochem. Soc.*, 163[3] H213-H17 (2016).
3. J. M. Lehn, J. P. Sauvage, and R. Ziessel, "Photochemical water splitting continuous generation of hydrogen and oxygen by irradiation of aqueous suspensions of metal loaded strontium-titanate," *New J. Chem.*, 4[11] 623-27 (1980).
4. J. H. Luo and P. A. Maggard, "Hydrothermal synthesis and photocatalytic activities of SrTiO<sub>3</sub>-coated Fe<sub>2</sub>O<sub>3</sub> and BiFeO<sub>3</sub>," *Adv. Mater.*, 18[4] 514-17 (2006).
5. T. K. Townsend, N. D. Browning, and F. E. Osterloh, "Nanoscale Strontium Titanate Photocatalysts for Overall Water Splitting," *Acs Nano*, 6[8] 7420-26 (2012).
6. A. N. Chiaramonti, C. H. Lanier, L. D. Marks, and P. C. Stair, "Time, temperature, and oxygen partial pressure-dependent surface reconstructions on SrTiO<sub>3</sub>(111): A systematic study of oxygen-rich conditions," *Surf. Sci.*, 602[18] 3018-25 (2008).
7. L. D. Marks, A. N. Chiaramonti, F. Tran, and P. Blaha, "The small unit cell reconstructions of SrTiO<sub>3</sub>(111)," *Surf. Sci.*, 603[14] 2179-87 (2009).
8. B. C. Russell and M. R. Castell, "Surface of sputtered and annealed polar SrTiO<sub>3</sub>(111): TiO<sub>x</sub>-rich ( $n \times n$ ) reconstructions," *J. Phys. Chem. C*, 112[16] 6538-45 (2008).
9. S. Ferrer and G. A. Somorjai, "UPS and XPS studies of chemisorption of O<sub>2</sub>, H<sub>2</sub>, and H<sub>2</sub>O on reduced and stoichiometric SrTiO<sub>3</sub>(111) surfaces - the effects of illumination," *Surf. Sci.*, 94[1] 41-56 (1980).
10. P. V. Nagarkar, P. C. Searson, and F. D. Gealy, "Effect of surface-treatment on SrTiO<sub>3</sub> - an X-ray photoelectron spectroscopic study," *J. Appl. Phys.*, 69[1] 459-62 (1991).
11. J. L. Giocondi and G. S. Rohrer, "Structure sensitivity of photochemical oxidation and reduction reactions on SrTiO<sub>3</sub> surfaces," *J. Am. Ceram. Soc.*, 86[7] 1182-89 (2003).
12. Y. Zhu, P. A. Salvador, and G. S. Rohrer, "Controlling the Relative Areas of PhotoCathodic and PhotoAnodic Terraces on the SrTiO<sub>3</sub> (111) Surface," *Chem. Mater.*, DOI: 10.1021/acs.chemmater.6b02205 in press (2016).
13. J. Goniakowski, F. Finocchi, and C. Noguera, "Polarity of oxide surfaces and nanostructures," *Rep. Prog. Phys.*, 71[1] (2008).
14. P. W. Tasker, "Stability of Ionic-Crystal Surfaces," *J. Phys. C*, 12[22] 4977-84 (1979).
15. N. V. Burbure, P. A. Salvador, and G. S. Rohrer, "Photochemical Reactivity of Titania Films on BaTiO<sub>3</sub> Substrates: Origin of Spatial Selectivity," *Chem. Mater.*, 22[21] 5823-30 (2010).
16. A. Heller, "Chemistry and applications of photocatalytic oxidation of thin organic films," *Accounts of Chemical Research*, 28[12] 503-08 (1995).
17. Y. L. Zhang, A. M. Schultz, P. A. Salvador, and G. S. Rohrer, "Spatially selective visible light photocatalytic activity of TiO<sub>2</sub>/BiFeO<sub>3</sub> heterostructures," *J. Mater. Chem.*, 21[12] 4168-74 (2011).
18. J. L. Giocondi and G. S. Rohrer, "Spatial separation of photochemical oxidation and reduction reactions on the surface of ferroelectric BaTiO<sub>3</sub>," *J. Phys. Chem. B*, 105[35] 8275-77 (2001).

19. J. J. Glickstein, P. A. Salvador, and G. S. Rohrer, "A Computational Model of Domain Specific Reactivity on Coated Ferroelectric Photocatalysts," *J. Phys. Chem. C*, 120[23] 12673-84 (2016).
20. L. Li, G. S. Rohrer, and P. A. Salvador, "Heterostructured Ceramic Powders for Photocatalytic Hydrogen Production: Nanostructured TiO<sub>2</sub> Shells Surrounding Microcrystalline (Ba,Sr)TiO<sub>3</sub> Cores," *J. Am. Ceram. Soc.*, 95[4] 1414-20 (2012).
21. M. Hirano, C. Nakahara, K. Ota, and M. Inagaki, "Direct formation of zirconia-doped titania with stable anatase-type structure by thermal hydrolysis," *J. Amer. Ceram. Soc.*, 85[5] 1333-35 (2002).
22. M. Inagaki, Y. Nakazawa, M. Hirano, Y. Kobayashi, and M. Toyoda, "Preparation of stable anatase-type TiO<sub>2</sub> and its photocatalytic performance," *Int. J. Inorg. Mater.*, 3[7] 809-11 (2001).
23. J. Zhang, J. H. Bang, C. Tang, and P. V. Kamat, "Tailored TiO<sub>2</sub>-SrTiO<sub>3</sub> Heterostructure Nanotube Arrays for Improved Photoelectrochemical Performance," *ACS Nano*, 4[1] 387-95 (2010).
24. Gwyddion, "Available from World Wide Web: <http://gwyddion.net/resources.php>." in., 2011.
25. J. B. Lowekamp, G. S. Rohrer, P. A. M. Hotsenpiller, J. D. Bolt, and W. E. Farneth, "Anisotropic photochemical reactivity of bulk TiO<sub>2</sub> crystals," *J. Phys. Chem. B*, 102[38] 7323-27 (1998).
26. R. Munprom, P. A. Salvador, and G. S. Rohrer, "Polar Domains at the Surface of Centrosymmetric BiVO<sub>4</sub>," *Chem. Mater.*, 26[9] 2774-76 (2014).
27. J. M. Herrmann, J. Disdier, and P. Pichat, "PHOTOCATALYTIC DEPOSITION OF SILVER ON POWDER TITANIA - CONSEQUENCES FOR THE RECOVERY OF SILVER," *Journal of Catalysis*, 113[1] 72-81 (1988).
28. N. V. Burbure, P. A. Salvador, and G. S. Rohrer, "Orientation and Phase Relationships between Titania Films and Polycrystalline BaTiO<sub>3</sub> Substrates as Determined by Electron Backscatter Diffraction Mapping," *J. Am. Ceram. Soc.*, 93[9] 2530-33 (2010).
29. R. W. G. Wyckoff, "Crystal Structures," Vol. 2. Interscience: New York, (1964).
30. D. T. Cromer and K. Herrington, "The Structures of Anatase and Rutile," *J. Amer. Chem. Soc.*, 77[18] 4708-09 (1955).
31. A. Lotnyk, S. Senz, and D. Hesse, "Epitaxial growth of TiO<sub>2</sub> thin films on SrTiO<sub>3</sub>, LaAlO<sub>3</sub> and yttria-stabilized zirconia substrates by electron beam evaporation," *Thin Solid Films*, 515[7-8] 3439-47 (2007).
32. PANalytical, "X'PERT PRO MRD XL: PW3217 X'PERT REFLECTIVITY". in., *The Netherlands* 2007.
33. A. Frye, R. H. French, and D. A. Bonnell, "Optical properties and electronic structure of oxidized and reduced single-crystal strontium titanate," *Z. Metal.*, 94[3] 226-32 (2003).
34. T. Sekiya, K. Ichimura, M. Igarashi, and S. Kurita, "Absorption spectra of anatase TiO<sub>2</sub> single crystals heat-treated under oxygen atmosphere," *J. Phys. Chem. Solids*, 61[8] 1237-42 (2000).
35. H. Tang, F. Levy, H. Berger, and P. E. Schmid, "Urbach Tail of Anatase TiO<sub>2</sub>," *Phys. Rev. B*, 52[11] 7771-74 (1995).
36. Y. Yamada and Y. Kanemitsu, "Determination of electron and hole lifetimes of rutile and anatase TiO<sub>2</sub> single crystals," *Appl. Phys. Lett.*, 101[13] (2012).

37. W. Melitz, J. Shen, A. C. Kummel, and S. Lee, "Kelvin probe force microscopy and its application," *Surf. Sci. Rep.*, 66[1] 1-27 (2011).
38. M. Nonnenmacher, M. P. Oboyle, and H. K. Wickramasinghe, "Kelvin probe force microscopy," *Appl. Phys. Lett.*, 58[25] 2921-23 (1991).
39. N. V. Burbure, P. A. Salvador, and G. S. Rohrer, "Photochemical Reactivity of Titania Films on BaTiO<sub>3</sub> Substrates: Influence of Titania Phase and Orientation," *Chem. Mater.*, 22[21] 5831-37 (2010).
40. J. Pan, G. Q. Lu, and H.-M. Cheng, "On the True Photoreactivity Order of {001}, {010}, and {101} Facets of Anatase TiO<sub>2</sub> Crystals," *Angew. Chem. Int.*, 50[9] 2133-37 (2011).
41. A. G. Thomas, W. R. Flavell, A. K. Mallick, A. R. Kumarasinghe, D. Tsoutsou, N. Khan, C. Chatwin, S. Rayner, G. C. Smith, R. L. Stockbauer, S. Warren, T. K. Johal, S. Patel, D. Holland, A. Taleb, and F. Wiame, "Comparison of the electronic structure of anatase and rutile TiO<sub>2</sub> single-crystal surfaces using resonant photoemission and x-ray absorption spectroscopy," *Phys. Rev. B*, 75[3] 035105 (2007).
42. K. van Benthem, C. Elsasser, and R. H. French, "Bulk electronic structure of SrTiO<sub>3</sub>: Experiment and theory," *J. Appl. Phys.*, 90[12] 6156-64 (2001).
43. M. Batzill, "Fundamental aspects of surface engineering of transition metal oxide photocatalysts," *Energy Environ. Sci.*, 4[9] 3275-86 (2011).
44. A. Kakekhani and S. Ismail-Beigi, "Ferroelectric-Based Catalysis: Switchable Surface Chemistry," *ACS Catal.*, 5[8] 4537-45 (2015).
45. M. A. Khan, M. A. Nadeem, and H. Idrissn, "Ferroelectric polarization effect on surface chemistry and photocatalytic activity: A review," *Surface Science Reports*, 71[1] 1-31 (2016).
46. L. Li, P. A. Salvador, and G. S. Rohrer, "Photocatalysts with internal electric fields," *Nanoscale*, 6[1] 24-42 (2014).
47. D. Tiwari and S. Dunn, "Photochemistry on a polarisable semi-conductor: what do we understand today?," *Journal of Materials Science*, 44[19] 5063-79 (2009).

## Chapter 8 Conclusions

*This chapter summarizes all of the experimental results from Chapters 4-7, both in the context of addressing the three motivating questions proposed in Chapter 1.2, and in the context of integrating related details from each individual chapter.*

### 8.1 Photochemical activity and surface potential correlation

*Q: Do measured surface potentials correlate with the spatial location of photochemical half reactions on the surfaces of  $\text{Fe}_2\text{O}_3$  and  $\text{SrTiO}_3$  catalysts?*

*A: Yes. In the studies on polycrystalline hematite ceramics and  $\text{SrTiO}_3$  (111) and (110) single crystals, the local photochemical activity was correlated with the local surface potential. In all cases, high (low) surface potential regions (averaged over grains or specific to individual atomic terraces) were found to be more reactive in photoreduction (photooxidation). These results are consistent with local surface reactivity being influenced by the local sub-surface band bending, which drives photogenerated carriers to the local surface in different amounts.*

The orientation dependence of the photochemical reactivity of hematite was measured and found to be anisotropic. Based on many observations, it was concluded that the orientations of

grains that are most reactive for the photoreduction of  $\text{Ag}^+$  are located close to the  $(1\bar{1}02)$  orientation. On the other hand, surfaces oriented near  $(0001)$  are the least reactive. Surface potential images were recorded for many grains and it was found that most of the reactive grains have high surface potentials while unreactive grains have low surface potential. Although outliers exist, the variation in the average measured surface potential as a function of crystal orientation is consistent with the orientation dependent reactivity; the average surface potentials of the most reactive orientations are the highest, and the average potentials for the least reactive orientations are lowest. This surface potential correlation was compared with other possible origins of the anisotropic reactivity, and it was found to be the most satisfactory description.

For the polycrystalline hematite ceramics, the average potential and average reactivity for a given orientation were investigated. On the other hand, the local surface potential and local reactivity for an individual orientation were investigated for  $\text{SrTiO}_3$  single crystals. For both  $(111)$  and  $(110)$  surfaces exhibiting step and terrace structures (from high temperature anneals), a similar correlation was found between the surface potential of specific terraces and the reactivity on those terraces, for both  $\text{SrTiO}_3$   $(111)$  and  $(110)$  surfaces, as was found for the polycrystalline hematite. Polar atomic terraces that reduced silver ions to silver metal in marker reactions had the highest surface potential, and terraces that oxidize lead ions had the lowest surface potential.

Interestingly, the relative amount of the different terraces (discussed below) could be varied widely through thermal treatments, such that the average reactivity of identically oriented crystals could be modified from fully photoreductive to fully photooxidative, with a concomitant change in the average surface potential. This implies that the orientation dependent reactivity of  $\text{SrTiO}_3$  ceramics may vary widely depending on the processing conditions. In the case of  $\text{Fe}_2\text{O}_3$ , we did observe cases where some samples had a different orientation dependent reactivity than most (the

( $\bar{1}\bar{2}10$ ) orientation was most reactive for  $\text{Ag}^+$  reduction). In that case, the orientation dependent surface potential also varied, always being consistent with the main conclusion correlating high surface potential surfaces favoring photoreduction. The observations on  $\text{SrTiO}_3$  agree: the relative surface reactivity for a given orientation correlates with surface charge on the orientation, rather than the specific orientation itself.

## 8.2 Control surface termination of $\text{SrTiO}_3$

*Q: Can the  $\text{SrTiO}_3$  catalyst's overall photochemical reactivity be tuned by modifications of the area percentage of high or low potential surfaces (terminations)?*

*A: Yes. By modifying thermal annealing conditions, the fractional area of terraces that promote photoreduction was tuned between 14 % and 55 % for  $\text{SrTiO}_3$  (111) surfaces and between 0 % and 98 % for  $\text{SrTiO}_3$  (110) surfaces.*

In the experiments on  $\text{SrTiO}_3$  (111) surfaces, more than 50 % of the surface area of standard samples, those annealed in covered alumina crucibles in air at 1250 °C, were active for the photoreduction of silver. To control the areal coverage ratio of the two terminations, samples were annealed in a titania rich atmosphere established by the addition of excess  $\text{TiO}_2$  powders or  $\text{TiO}_2/\text{SrTiO}_3$  powder mixtures, always at 1250 °C. All results showed a consistent trend: the fractional coverage of terraces that were active for photoreduction, and that had high surface potentials, decreased as the relative titania excess in the powder beds increased. This finding demonstrates a new route to controlling polar terminations of  $\text{SrTiO}_3$  (111), and establishes that reactivity is not exactly orientation specific: it can be modified through surface engineering.

The method discussed above was further tested and developed on SrTiO<sub>3</sub> (110) single crystal surfaces. The surface termination of SrTiO<sub>3</sub> (110) was investigated as a function of time, temperature, and composition of powder beds. Both decreasing the annealing temperature ( $T$  varied from 1200 °C to 1000 °C) and decreasing the annealing time ( $t$  varied from 6 hours to 0 hour) led to increasing area fractions of the photoreductive terraces. The area fraction of photoreductive terraces was tuned from 80 % at low- $T$  and short  $t$  to 0 % at high- $T$  and long  $t$ . This implies that the as received surface chemistry favors photoreduction and high surface potentials, and that high-temperature anneals move the surface chemistry to favor photooxidation and low-surface potentials. Surfaces annealed with adjacent TiO<sub>2</sub> powders exhibited increased fractions of photooxidative terraces, while surfaces annealed with adjacent Sr<sub>3</sub>Ti<sub>2</sub>O<sub>7</sub> powders exhibited increased fractions of photoreductive terraces. Using the three parameters judiciously allowed for the (110) surfaces to be tuned between essentially fully photoreductive with high surface potentials to essentially fully photooxidative with low surface potentials.

The simplest interpretation of how the powder beds interact is through a Sr-containing vapor phase, whose overall pressure is determined from the relative evaporation / condensation rates at the surfaces in the chamber. When excess TiO<sub>2</sub> powder is used, Sr-containing vapors can react with TiO<sub>2</sub>, increasing the driving force for evaporation at the crystal surface. Conversely, when TiO<sub>2</sub>/SrTiO<sub>3</sub> mixtures or Sr<sub>3</sub>Ti<sub>2</sub>O<sub>7</sub> are used, evaporation from the Sr-rich higher surface area powders decreases (increases) the driving force for evaporation (condensation) from the crystal surface. XPS results on the Ti concentration at the surface were in agreement with this hypothesis. Nevertheless, the main point is that the surface reactivity and potential could be engineered for individual orientations to exhibit any fractional coverages of terraces that promote photoreduction or photooxidation, with the concomitant change in surface potential.

This again implies that the relative surface reactivity of oxides, especially polar surfaces for materials having a volatile component, can be engineered to exhibit a range of relative reactivity if the surface potential can be engineered chemically through process steps. Engineering through chemistry and processing to control surface charges may be simpler than engineering charges in ferroelectrics and flexo-electrics. Indications from outliers in the  $\text{Fe}_2\text{O}_3$  experiment are that process-dependent orientations in surface charge can be used to modify orientation dependent reactivity in the binary oxides too. The longer term question is now: How can we engineer a single orientation to exhibit optimized overall reactivity with spatially separated and balance photooxidation and photoreduction rates.

### **8.3 Photochemical activity of $\text{TiO}_2/\text{SrTiO}_3$ heterostructure**

*Q: Do potential differences at buried interfaces in  $\text{TiO}_2/\text{SrTiO}_3(111)$  heterostructures affect the photochemical activity of the film's surface?*

*A: Yes. In the study of  $\text{TiO}_2/\text{SrTiO}_3(111)$  heterostructure, silver was found to be preferentially photoreduced on the  $\text{TiO}_2$  film's surface at positions directly above photoreductive terraces on the bare substrate, which also had more positive surface potentials. Even for the thickest (16 nm) films, where the spatial variation in the surface potential was no longer measurable by KFM, the film surfaces retained the spatial selectivity of the underlying substrate.*

The effect of the potential difference at the film-substrate interface in heterostructured photocatalysts, composed of 1 – 16 nm thick titania films supported on thermally annealed  $\text{SrTiO}_3(111)$  substrates, was studied. The pattern of photoreduced silver on the surfaces of all the films,

i.e., for all thicknesses studied, mimics the pattern of photoreduced silver on the bare SrTiO<sub>3</sub> substrate before depositing the film. For the thinnest films, the relative surface potential measured at the film's surface was similar to that of the bare substrate too. For the thicker films, the surface potential at the film's surface no longer matched the pattern from the substrate, but the spatial dependence of reactivity did. These observations show that the photochemical reactivities of the thin films are controlled by the potentials at the buried film-substrate interface. A possible mechanism for the photochemical reaction on this heterostructure was proposed: it involved electrons photogenerated in the SrTiO<sub>3</sub> substrate that migrate to the buried interface under the influence of the internal electric field associated with potential difference at the interface, which then can migrate across the film where they participate in the photoreduction reaction.

This mechanism is identical to that proposed for heterostructured ferroelectric photocatalysts, such as TiO<sub>2</sub>-coated BaTiO<sub>3</sub>, which was based on physical and computational investigations.<sup>1, 2, 3</sup> Combined with the demonstration that the surface charge of the catalyst, for any given orientation, can be influenced through thermal treatments in controlled atmospheres to exhibit any fractional relative reactivity, from photoanodic to photocathodic and anywhere in between, similar to how a ferroelectric can be controlled by poling or domain writing, indicates that entirely new avenues are possible in engineering optimized stable photocatalysts through chemical control of a powdered catalyst's surface chemistry through straightforward annealing steps. Because there are many more non-ferroelectric photocatalysts than there are ferroelectric ones, the chemical approach offers a much broader potential for new photocatalyst development, possibly leading to highly efficient solar photocatalysts for water splitting.

## Reference

1. N. V. Burbure, P. A. Salvador, and G. S. Rohrer, "Photochemical reactivity of titania films on BaTiO<sub>3</sub> substrates: origin of spatial selectivity," *Chemistry of Materials*, 22[21] 5823-30 (2010).
2. N. V. Burbure, P. A. Salvador, and G. S. Rohrer, "Photochemical Reactivity of Titania Films on BaTiO<sub>3</sub> Substrates: Influence of Titania Phase and Orientation," *Chemistry of Materials*, 22[21] 5831-37 (2010).
3. J. J. Glickstein, P. A. Salvador, and G. S. Rohrer, "A Computational Model of Domain Specific Reactivity on Coated Ferroelectric Photocatalysts," *The Journal of Physical Chemistry C* (2016).